CHEMICAL REVIEWS

pubs.acs.org/CR

Review

Gas-Phase Infrared Spectroscopy of Neutral Peptides: Insights from the Far-IR and THz Domain

Sjors Bakels, Marie-Pierre Gaigeot,* and Anouk M. Rijs*

Cite This: *Chem. Rev.* 2020, 120, 3233−3260

Read Online

ACCESS | Metrics & More | Article Recommendations | Supporting Information

ABSTRACT: Gas-phase, double resonance IR spectroscopy has proven to be an excellent approach to obtain structural information on peptides ranging from single amino acids to large peptides and peptide clusters. In this review, we discuss the state-of-the-art of infrared action spectroscopy of peptides in the far-IR and THz regime. An introduction to the field of far-IR spectroscopy is given, thereby highlighting the opportunities that are provided for gas-phase research on neutral peptides. Current experimental methods, including spectroscopic schemes, have been reviewed. Structural information from the experimental far-IR spectra can be obtained with the help of suitable theoretical approaches such as dynamical DFT techniques and the recently developed Graph Theory. The aim of this review is to underline how the synergy between far-IR spectroscopy and theory can provide an unprecedented picture of the structure of neutral biomolecules in the gas phase. The far-IR signatures of the discussed studies are summarized in a far-IR map, in order to gain insight into the origin of the far-IR localized and delocalized motions present in peptides and where they can be found in the electromagnetic spectrum.

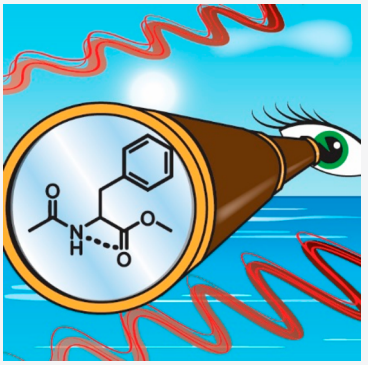

CONTENTS

1. Introduction 3234
2. Gas-Phase Spectroscopy of Neutral Molecules 3237
  2.1. IR−UV Ion Dip Spectroscopy 3237
    2.1.1. Resonance Enhanced Multiphoton Ionization 3237
    2.1.2. Far-IR Spectroscopy 3238
  2.2. Experimental Implementations: Neutral Biomolecules in the Gas Phase 3238
    2.2.1. Laser Desorption 3239
    2.2.2. Molecular Beams 3239
    2.2.3. Time-of-Flight Mass Spectrometry 3240
    2.2.4. Far-IR Laser Sources: Use of the FELIX Free Electron Lasers 3240
3. Theoretical Approaches 3240
  3.1. Overview and General Introduction of Theoretical Methods 3240
  3.2. DFT-MD for Vibrational Spectroscopy 3241
  3.3. Graph Theory and Assignment of the Far-IR Vibrational Modes 3242
4. Characterization of the Far-IR Signatures of Dipeptides 3243
  4.1. Secondary Structure of Dipeptides 3243
  4.2. Far-IR Spectroscopy of Dipeptides 3244
    4.2.1. Spectral Assignment Using Far-IR Ion Dip Spectroscopy and DFT-MD Calculations 3244
    4.2.2. Unprecedented Structural Far-IR Fingerprints 3244
    4.2.3. Far-IR Conformational Selectivity 3245
  4.3. Insights on Dipeptides from the Far-IR Region 3245
    4.3.1. Localized Modes 3245
    4.3.2. Delocalized Backbone Modes (0−400 cm^{-1}) 3246
    4.3.3. Hydrogen Bond Signatures (0−250 cm^{-1}) 3246
5. Peptide Clusters 3246
  5.1. Static-DFT versus DFT-MD for a Simple Peptide and Its Dimer 3247
    5.1.1. Z-Ala Monomer 3247
    5.1.2. Z-Ala Dimer 3247
  5.2. Use of Graph Theory on Ac-Phe-OMe and Its β-Sheet Dimer 3248
    5.2.1. NH Wagging Motion (450−650 cm^{-1}) 3248
    5.2.2. Delocalized Motions at 250−280 cm^{-1} 3249
    5.2.3. Torsional Delocalized Motions at ∼200 cm^{-1} 3250
6. Outlook to Larger Systems 3250
  6.1. Mini-proteins: How Large Can We Go in the Far-IR? 3250
7. Concluding Remarks and Outlook 3251
Associated Content 3252

Special Issue: Bond Specific Spectroscopy of Peptides and Proteins

Received: September 3, 2019
Published: February 19, 2020

https://dx.doi.org/10.1021/acs.chemrev.9b00547
Chem. Rev. 2020, 120, 3233−3260

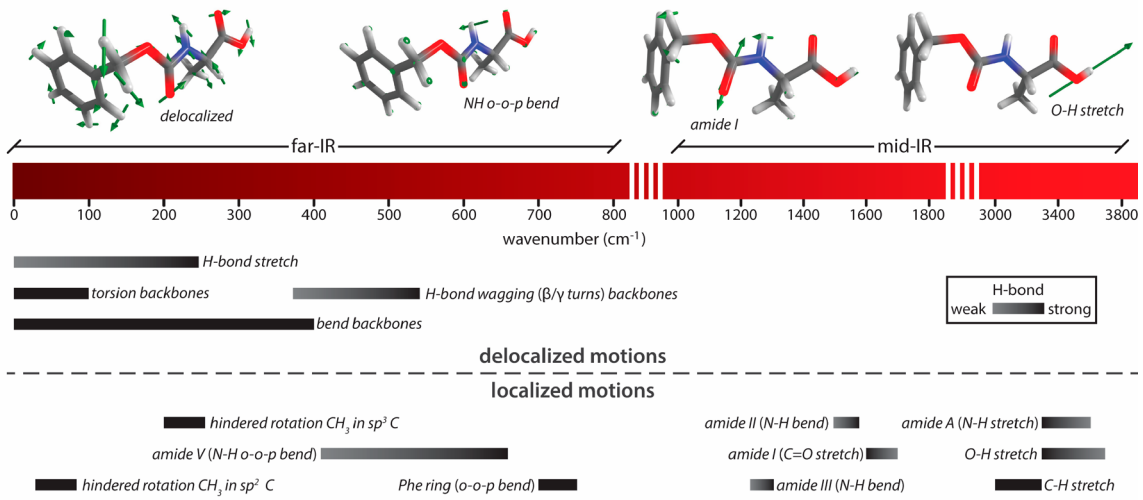

Figure 1. Signatures of common far- and mid-infrared vibrational modes, categorized by their delocalized (top) or localized character (bottom). An indication for the effect of hydrogen bonding on the frequency of modes is given by a gray scale: ranging from weak (light gray) to strong (black) hydrogen bonds.

Supporting Information 3252
Author Information 3252
Corresponding Authors 3252
Author 3252
Notes 3252
Biographies 3252
Acknowledgments 3252
Abbreviations 3253
References 3253

1. INTRODUCTION

Gas-phase infrared spectroscopy is a continuously developing method for the structural determination of biological molecules under isolated conditions. Vibrational or infrared spectroscopy brings detailed insights into the 3-dimensional structure of molecules and the intra- and intermolecular interactions via diagnostic vibrational modes.[1,2] Due to the close relationship between structure and structural changes with biomolecular function, IR action spectroscopy has been extensively applied to probe gas-phase structural details of a large variety of molecules and clusters such as peptides and proteins,[3−16] DNA bases,[17−22] glycans,[23−30] molecular motors,[31−34] metal complexes,[35−38] solvent clusters,[39−51] and astrochemical molecules.[52−57]

Traditionally, IR spectroscopy probes the fingerprint signatures focusing mainly on the amide II (NH bend), amide I (C═O stretch), and amide A (NH stretch) modes in the 1000−2000 cm^{-1} and 3300−3800 cm^{-1} region, see Figure 1. Recently, IR action spectroscopic experiments have advanced into the far-IR and THz regime. The terms far-IR and THz are often used interchangeably, although strictly speaking the definition of THz spectroscopy is limited to 10−100 cm^{-1} (0.3−3 THz). Here, no such distinction will be made and the term far-IR is used for the full 10−800 cm^{-1} (0.3−24 THz) region. In this far-IR region, large amplitude and collective motions are probed such as backbone torsional vibrations, out-of-plane modes, and hydrogen bond dynamics (Figure 1).[13] The rotational and vibrational transitions in molecules, collective vibrations in condensed-phase media, or low-energy excitations and carrier dynamics in electronic materials can be studied using this part of the electromagnetic spectrum.[58] This diversity in physical properties makes it a scientific field with great potential. For example, in solid state physics, the far-IR/THz frequencies correspond to physical phenomena of electronic materials including electron transport in semiconductors, nanomaterials, and correlated electron materials. THz radiation can be used to probe these electronic materials without the need of making contacts, which is particularly important for nanomaterials.[59,60] Other applications are more analytical in nature; here, the low-frequency vibrations in molecules are probed to identify an unknown substance. This approach can for example be applied to identify explosives and illegal drugs in a security setting, as many explosives and drugs have a unique THz fingerprint.[61,62] The most recent developments in condensed phase THz spectroscopy focus on imaging. By using spatially broad THz pulses, two-dimensional images can be recorded within seconds.[63] Since the THz/far-IR vibrational modes function as fingerprints for many molecules, the resulting two-dimensional images are molecule specific. These studies have also been extended to the imaging of brain tumors in rats and other tissues.[64,65]

In the study of biomolecular structure, far-IR action spectroscopy adopts a unique position as the frequency range which is probed in this part of the electromagnetic spectrum corresponds predominantly to delocalized modes, providing structural information beyond the local view provided by the mid-IR. This makes it a diverse tool for the study of biomolecules in different media.[66−68] In crystallized biomolecules, the structural sensitivity of far-IR spectroscopy was demonstrated by its ability to differentiate between polypeptides where either a single amino acid was exchanged or where the sequence was altered.[69] Detailed information in biomolecular function was obtained by probing for example the channel-breathing motion in a polypeptide nanotube and the clamping motion of a catalytic protein.[70] Specifically, the Markelz group showed that the effect of an inhibitor binding to the HEWL protein could be observed via a change in the direction of the clamping motion using crystal anisotropy THz microscopy (CATM).[71]− Most studies focus on the hydration shell of biomolecules, as intramolecular motions of biomole-

https://dx.doi.org/10.1021/acs.chemrev.9b00547
Chem. Rev. 2020, 120, 3233−3260

cules themselves are difficult to observe due to their strong coupling to coordinated water. For example, the effect of hydrogen bonding of the studied protein with the surrounding water molecules can be observed as a disturbance in the dynamics of these water molecules. This retardation can extend up to 25 Å (8 water molecule layers) away from the studied protein, depending on the number of hydrogen bonds between the water and the protein.[72−74] This strong interaction between protein and its hydration shell was used to probe (time-dependent) conformational changes such as folding or denaturing as was for example shown for different antifreeze proteins.[75−79] More detailed studies on the motions of biomolecules in solution are complicated by their strong coupling to water. However, a recent breakthrough using optical Kerr-effect (OKE) spectroscopy has demonstrated the presence of underdamped motions in DNA.[80,81]

Gas-phase far-IR action spectroscopy has been developed and applied predominantly to probe the 3D structures of metal clusters,[36,38,82] water and solvated ions,[83] astrophysical and astrochemical related molecules,[84] organic, hydrogen bonded molecules,[85] and biomolecules.[14,86,87] Far-IR action spectroscopy is often combined with cold methods such as molecular beam expansions and cold ion traps, using typically action spectroscopic methods such as IRPD (Infrared Photon Dissociation) of tagged ions and IR-UV ion dip spectroscopy of cooled neutral molecules.[1,88] To obtain structural information in the far-IR spectral region, intense and widely tunable radiation from far-IR Free Electron Lasers (FELs)[89−91] is essential.

Over the years a number of techniques have been developed in order to measure the far-IR or THz response of (bio)molecules in the gas phase. The most relevant ones will be reviewed here. FT-IR spectroscopy is widely adopted, especially due to the commercially available experimental setups and versatility of this method. It is mainly used for studies in solution and condensed phases. However, gas-phase experiments on volatile molecules using either gas cells, supersonic expansions, slit jets or weakly interacting matrices were also performed, yielding high resolution spectra of for example acetylene,[92,93] methane,[94] benzene,[95] methanol,[96] and CO.[97] These spectra usually cover a narrow region (e.g., a single band) of the far-IR spectrum. Additionally, broad range FT-IR spectra of small biomolecules have been obtained for molecules such as *N*-methylformamide,[98] glycine, alanine, and their dimers.[99] Another technique, which is mainly advanced by the group of Saykally, is THz vibration−rotation-tunneling spectroscopy (THz-VRT spectroscopy).[100−102] Here, tunable THz light is generated either by using the sum and difference frequencies that are obtained by mixing the output of an IR gas laser with tunable frequency-modulated microwaves[103] or by using quantum cascade lasers.[104] The light is then directed into a multipass cell to coincide with a supersonic expansion containing the sample molecules. By detecting the emitted radiation, very high resolution spectra can be obtained, as was shown for water complexes[102,105] and the propane−water dimer.[103] Broadband microwave spectroscopy, although technically accessing the adjacent spectral region (but overlapping the THz domain), is known for its ability to obtain precise structural information from the recorded rotational spectra. With the introduction of chirped pulse excitation,[106] molecules of interest include mostly volatile organic molecules such as odorants, chiral molecules, and PAHs.[84,107−109] In combination with laser ablation techniques, single amino acids and recently small peptides have become within reach.[110−113]

Another important technique addressing the far-IR region is Raman spectroscopy. The groups of Balabin and Bar combine Raman spectroscopy with a supersonic expansion.[114−117] In general, virtual states of the molecules are populated by visible light which is guided into a multipass cell. After this, the molecules will fall back to vibrational states of the electronic ground state and the molecule will emit this light which is consequently detected. Raman spectroscopy can probe states which are not allowed by IR spectroscopy, which makes the two techniques complementary. Typically, small and volatile molecules are studied with this Raman inelastic scattering processes technique, thereby elucidating structural properties of alkanes[114] and small amino acids such as glycine[115] and alanine.[116] Raman bands can also be used in a similar scheme as used in IR-UV ion dip spectroscopy, in a technique named ionization-loss stimulated Raman spectroscopy (ILSRS). Using REMPI as the excitation and ionization step, first the molecules are excited to a virtual state, and then a second laser (both visible SRS lasers require ∼30 mJ/pulse) is employed to scan the vibrational states.[117−119] With the second laser on resonance with a vibrational state, a dip in the spectrum will be observed as the virtual states will fall back quickly to the electronic and vibrational ground state to be probed by the REMPI lasers. Molecules that are probed by this technique are relatively small, such as tryptamine[118] and 2-phenylethylamine.[119]

Conformation specific far-IR spectra can also be obtained with Laser-Induced fluorescence (LIF) and/or dispersed fluorescence spectroscopy, thereby obtaining the same peak positions as in IR-UV ion dip spectroscopy.[120,121] Molecules that have been studied using this technique include tryptamine,[121] phenol (dimer),[122] phenol-acetylene aggregates,[123] and adenine.[124] In a similar fashion, the far-IR vibrations can also be probed via stimulated emission pumping (SEP), in which a UV pump−dump scheme is used to excite the molecules to a certain vibrational energy level of the electronic ground state. This technique holds that it is only applied to study small, volatile molecules.[125−128]

Ideally, to obtain and understand far-IR signatures of biomolecules, conformational selectivity, mass selectivity, and the ability to measure larger, cooled neutral peptides (i.e., using laser desorption) are combined in one single experiment. Although each of the above-mentioned techniques have their specific strengths, they are mainly limited to smaller biomolecules and/or miss the required selectivity. At this moment, far-IR ion dip spectroscopy combines these necessities and is the only method able to record the far-IR signatures of peptides of significant size and their clusters and complexes with water. Therefore, this review focuses on the results obtained with this technique.

To examine the feasibility of far-IR UV ion dip spectroscopy, phenol derivatives, such as catechol, saligenin, salicylic acid, ethylvanillin, etc., have been used as model systems.[40,85,129] These molecules were selected for their propensity to form intramolecular hydrogen bonds as well as for their ability to absorb UV light allowing us to apply IR-UV ion dip spectroscopy. However, compared to for example peptides, they are relatively small and mostly rigid, thereby reducing the number of degrees of freedom. This makes them ideal candidates to evaluate the performance of different static and dynamic DFT computational techniques used to predict far-IR

https://dx.doi.org/10.1021/acs.chemrev.9b00547
Chem. Rev. 2020, 120, 3233−3260

absorption features. Two diagnostic vibrational modes that are expected to be diagnostic for the hydrogen bond strength have been identified in the far-IR, namely the hydrogen bonded OH torsion and the hydrogen bond stretching modes; see Figure 1. Their frequency is assessed with respect to the hydrogen bond strength via the hydrogen bonded OH bond length (Figure 2).

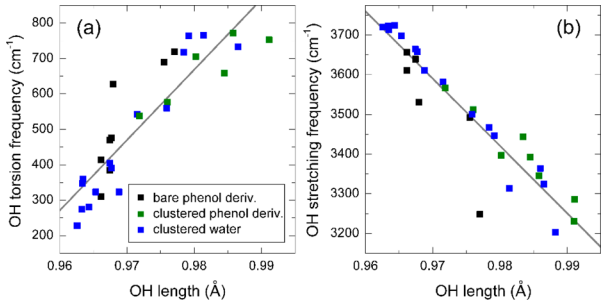

Figure 2. Relation between the OH bond length and (a) the hydrogen bonded OH torsion frequency and (b) the hydrogen bonded OH stretching frequency. In black, the vibrations of the OH groups of the bare phenol derivatives; in green, the OH moieties of the phenol derivatives hydrogen bonded to one or more water molecules; and in blue, the OH vibrations of the intermolecularly hydrogen bonded water molecules. Reprinted with permission from ref 130.

Figure 2a presents the far-IR torsion frequency, while Figure 2b shows the traditional mid-IR OH stretching vibration. Both plots show that the shifts in frequency correlate linearly to the OH length. This holds for intramolecular (in black), but also for intermolecular hydrogen bonds (in green and blue) when studying molecule−water clusters.[40] In contrast, the measured frequency of these hydrogen bond deforming modes behaves asymptotically as a function of the hydrogen bond length itself, toward the frequency expected for their free OH torsion or stretch vibration, since the hydrogen bond strength decreases for increasing bond lengths. These insights provided a natural starting point for a bottom-up study into far-IR spectroscopy of isolated biological systems.

Far-IR spectroscopy offers a wealth of complementary information with respect to the mid-IR. In the first place the vibrational region that is probed is extended, but more importantly, the nature of the vibrations in that region is different. The mid-IR region probes predominantly local bend or stretch vibrations, providing information about the local environment. In contrast, the soft far-IR vibrational modes are typically delocalized over large parts of the molecule and hence are expected to be highly sensitive to the global conformational structure of molecules, i.e. to secondary structural motifs in the case of peptides. Moreover, these far-IR modes are more structurally unique. Different conformations that have identical interactions, and thus local modes, can now in principle be distinguished based on delocalized skeletal vibrations.[86] Second, the IR spectra of larger molecules (peptides) often suffer from increasing spectral congestion in the mid-IR region as a result of an increasing number of similar oscillators. Therefore, for large and complex systems only structural families can be identified rather than the exact structure of a single conformer.[32−34,86,131,132] Besides orthogonal techniques, such as ion mobility combined with mass spectrometry for ionic molecules or the use of double or triple resonance spectroscopic schemes for neutral molecules, far-IR spectra often show a wealth of well resolved absorption bands, allowing for enhanced structural assignments, provided theoretical calculations are accurate enough in finalizing the assignment. A third advantage is that the delocalized motions can give much more fundamental insight in biomolecular function. Biomolecules are typically large systems, such as proteins and DNA, which exhibit motions across the whole molecule. These motions are not only diagnostic for their secondary structure and folding conformation,[133] but are also involved in biomolecular function and activity. This can be either the folding of proteins into their active conformation,[134,135] motions that are involved in enzymatic activity, for instance upon ligand binding,[136] or the formation of peptide aggregates.[87]

In this review, we discuss the current state-of-the-art on gas-phase far-IR and THz spectroscopy of mass- and conformer-selected neutral peptides. Early experiments on tryptophan reported on the presence of resolved bands down to 100 cm^{-1}.[137,138] However, due to poor agreement between experimental and theoretical IR spectra, this far-IR region was not used for structural assignment or mode analysis. Cirtog et al. have studied the far-IR signatures (<800 cm^{-1}) of the model peptide Ac-Phe-NH_2 (NAPA) and its hydrated clusters using IR-UV ion dip spectroscopy with the free electron laser FELIX.[7] Two conformations of Ac-Phe-NH_2···H_2O clusters were identified in which the water molecule bridges the NH and C═O moieties of the Phe residue.[139] The IR experiments revealed three strong, intermolecular IR-active modes of these hydrates, namely the wagging motion of the free OH moiety of water (∼160 cm^{-1}) and the in-plane (∼400 cm^{-1}) and out-of-plane (∼600 cm^{-1}) librations (out-of-plane wagging motions) of water; see Figure 3. The shifts in the far-IR signatures

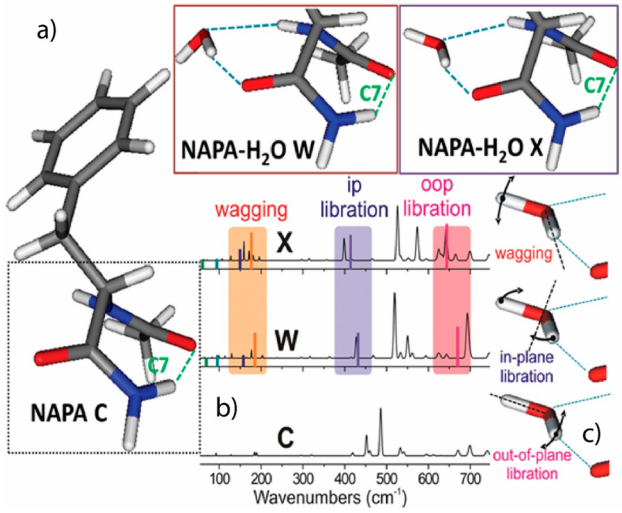

Figure 3. Infrared spectra of bare NAPA (C), and its two hydrated conformations (W, X) reveal the positions of wagging (orange), in-plane (purple), and out-of-plane (pink) libration modes of the water molecule. Adapted with permission from ref 7. Copyright 2012 The American Chemical Society.

between the different hydrates showed that these peptide−water modes strongly depend on the peptide conformation. Finally, the comparison between experimental features and theoretical frequencies revealed that this far-IR region is challenging for the theory, even for DFT with recent functionals and anharmonic corrections.[7,129] Current assignment still relies heavily on the combination of the commonly

https://dx.doi.org/10.1021/acs.chemrev.9b00547
Chem. Rev. 2020, 120, 3233−3260

used mid-IR and the newly explored far-IR regime. In this review, we will highlight the endeavors undertaken to use dynamic DFT calculations, density functional theory molecular dynamics (DFT-MD, also referred to as BOMD for Born–Oppenheimer molecular dynamics), to assign the nature of the far-IR modes and to be able to use this rich far-IR regime for structural analysis of peptides.

In section 2, the spectroscopic approaches employed to record mass- and conformer-selective far-IR spectra of peptides and typical experimental setups and strategies to perform IR-UV ion dip spectroscopy are described. Subsequently, in section 3, theoretical considerations will be lined out discussing DFT-MD simulations for vibrational spectroscopy and the newly developed graph theory for far-IR analyses. In sections 4–6, we review and discuss some of the results obtained from far-IR action spectroscopy combined with DFT-MD computations to probe specific sets of peptides ranging from dipeptides to peptide-clusters. Here, we focus first on the spectral assignment and the observed far-IR vibrational modes, followed by the theoretical developments to describe the far-IR modes. Section 6 addresses the largest peptides studied with far-IR action spectroscopy. The present review aims to shed light on experimental and theoretical strategies to decipher structural information along with scientific insights on neutral peptides from far-IR spectroscopy.

2. GAS-PHASE SPECTROSCOPY OF NEUTRAL MOLECULES

2.1. IR–UV Ion Dip Spectroscopy

The combination of experimental methods, including IR action spectroscopy, molecular beam expansion, and mass spectrometry, with quantum-chemical calculations has proven to be an excellent approach to unravel structural information on neutral, isolated biomolecules.[6,9,17,20,31,86,140−149] Biomolecules often exist in multiple, stable conformations in the gas phase. The low temperature resulting from the molecular beam environment allows the neutral molecules, brought into the gas phase by thermal evaporation or laser desorption, to be probed in a conformation selective manner by using double-resonance spectroscopic schemes. These action spectroscopic methods measure a change in properties of the studied molecules resulting from its interaction with light, rather than measuring the marginal effect of molecules on the incoming light as in conventional absorption spectroscopy. In this section, the experimental methods that are currently used to obtain mass- and conformation-selective far-IR spectra have been reviewed.

2.1.1. Resonance Enhanced Multiphoton Ionization. Essential in an IR–UV ion dip spectroscopic experiment is to record the UV excitation spectrum of the studied biomolecule. This is generally done via resonance enhanced multiphoton ionization (REMPI).[150,151] Here, the molecules are resonantly excited to typically their first electronic excited state and subsequently ionized by the absorption of a second photon (Figure 4.a). The resulting UV excitation spectrum shows features from all conformers present in the molecular beam, including their vibrational progressions. For the experiments discussed in this review predominantly one-color, (1 + 1) REMPI has been used, where the molecules are ionized by two photons of the same energy originating from a single laser via an intermediate electronically excited state (see Figure 4a, left side). However, for molecules in which the excited state energy is smaller than half of the ionization energy, two-color (1 + 1′) REMPI has to be employed (see Figure 4a, right side). This requires the use of two independent lasers, but brings experimental flexibility as the photon energy of the second laser can be chosen freely so that one can select the amount of energy deposited in the ionized molecule. The resonantly ionized molecules are subsequently detected in a time-of-flight based mass spectrometer (section 2.2.3) adding mass selectivity to the experiment.

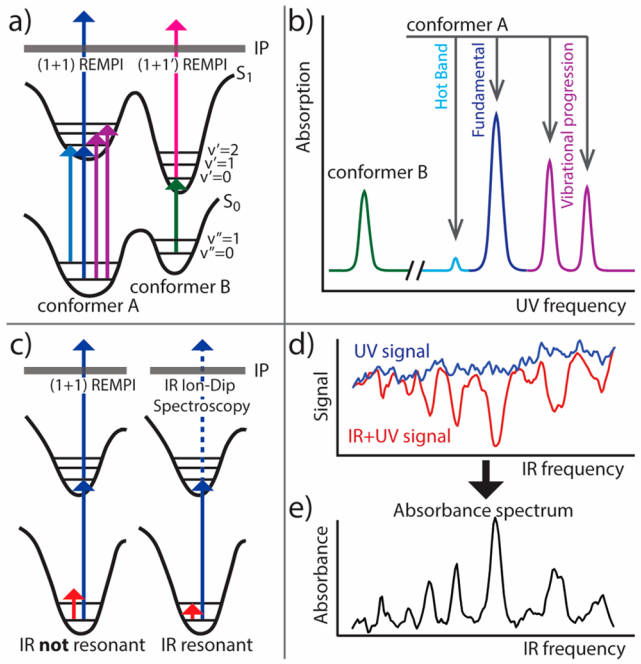

Figure 4. Schematic overview of the discussed spectroscopic methods, with (a) (1 + 1) and (1 + 1′) REMPI for two different conformers; (b) the resulting REMPI spectrum of the REMPI scheme show in (a), with corresponding colors; (c) IR ion dip spectroscopy; (d) a typical on/off IR spectrum; and (e) its corresponding absorbance spectrum.

Most of the peptides discussed in this review contain a UV absorbing moiety (chromophore) in the form of a phenyl ring either as part of the amino acid (for example phenylalanine), or added as a cap on the N- or C-terminus. Typically, resonant ionization occurs via their $\pi-\pi^*$ transition in a (1 + 1) REMPI scheme with UV photons of about 260 nm. The studied peptides are nonrigid molecules and can adapt multiple conformations with different intramolecular interactions in the gas phase. These small changes in the chemical environment of the chromophore can lead to large differences in the REMPI spectra. This results in conformer selectivity of the REMPI technique; for example, by selecting a single wavelength, a single conformer can be ionized. A typical REMPI spectrum shows a wealth of peaks besides the S_1-S_0 origin transition (Figure 4.b). Transitions from the vibronic ground state to the vibrationally excited states of the electronically excited state are observed at higher photon energies (highlighted in violet in Figure 4b), forming a vibrational progression. Another feature that can be seen in REMPI spectra is the so-called hot band, which can be used to determine the vibrational temperature of the molecule (section 2.2.1). This hot band can be found, even with supersonic cooling by the molecular beam, on the red side of the origin and originates from the transition from an excited vibrational state in the electronic ground state to the electronic excited state.

https://dx.doi.org/10.1021/acs.chemrev.9b00547
Chem. Rev. 2020, 120, 3233−3260

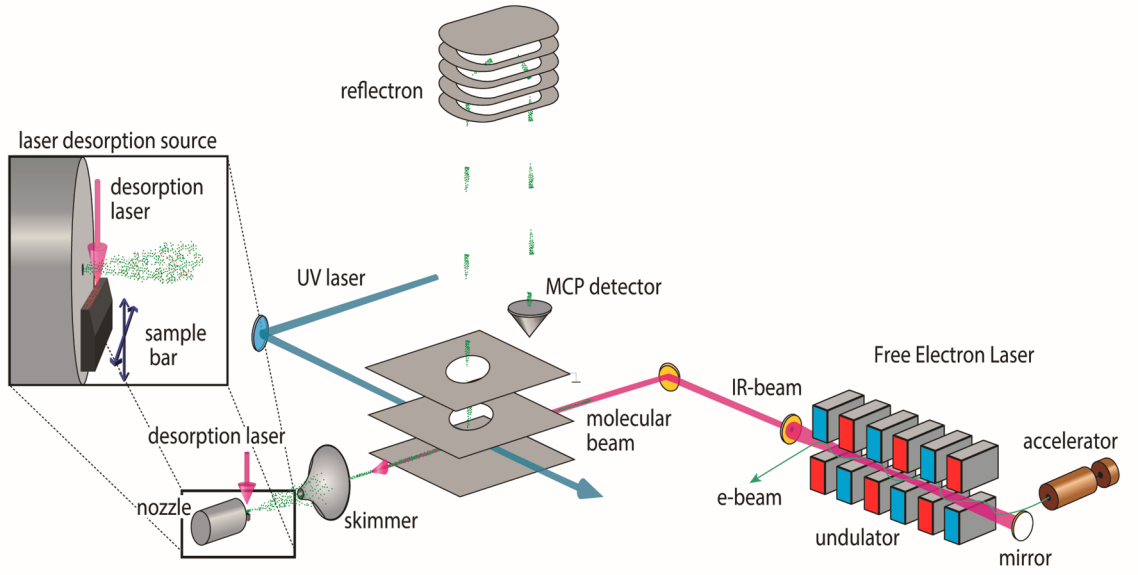

Figure 5. Schematic overview of the setup as it is used in the group of Rijs with a laser desorption source, skimmer, time-of-flight mass spectrometer, UV laser, and IR laser source FELIX. The schematic layout of the FELIX free-electron laser highlights the electron accelerator, undulator, and mirrors. Adapted with permission from ref 88. Copyright 2014 Springer Nature.

2.1.2. Far-IR Spectroscopy. By selecting a specific wavelength from the REMPI spectrum, a single conformer is excited, ionized, and detected, which results in a constant ion signal. The fixed UV pulse is preceded, typically by several tens to hundreds of nanoseconds, by a tunable IR laser pulse to obtain an infrared spectrum. When this IR frequency is resonant with a vibrational transition of the selected conformer, IR photon(s) are absorbed and population is transferred from the vibrational ground state to a vibrational excited level of the electronic ground state; see Figure 4c. This creates a dip in the ion signal created by the UV laser as the number of produced ions is reduced, which results from either (i) different spacing between the vibrational levels in the electronic ground and excited state, (ii) reduced Franck–Condon factors, (iii) possible fragmentation of the molecule after intramolecular vibrational energy redistribution (IVR), or a combination of the three.[131] This IR–UV double resonance technique, first developed by Lee et al.,[152] is often named infrared ion dip spectroscopy (IR-IDS)[88] or, alternatively, resonant ion dip infrared spectroscopy (RIDIRS).[140] The mass and conformer selective IR spectra are typically obtained in an on/off fashion, with the UV laser probing the abundance every shot and the IR laser alternating on and off to correct for fluctuations in the signal (Figure 4d).

In IR action spectroscopy, such as the applied IR–UV ion dip method, the effect of the IR radiation on the molecules is probed rather than the absorption or attenuation of light by the molecules. By carefully selecting the experimental parameters, the ion dip spectra can be converted into absorbance spectra to compare to calculated spectra (Figure 4e). Ideally, to obtain absolute absorption cross sections, all experimental variables that influence the signal intensity have to be taken into account, such as the laser beam area, pulse length, power, photon energy, and the transmission of the windows. To obtain absolute absorbance values, the following formula is used, derived from rate equations and assuming a one photon process:

$$A_{abs} = \text{Constant}\cdot\nu\cdot G(\nu)\cdot\log_{10}\left(\frac{N_{off}}{N_{on}(\nu)}\right) \quad (1)$$

with Constant a collection of constants, namely *nLhc*. Here, n is the number density of the molecules [m^{-3}], L the path length [m], h Planck's constant, and c the speed of light. ν is the wavenumber of the IR light [cm^{-1}] and is intrinsically correcting for the photon flux; N_{off} is the amount of detected ions when no IR light is present, and $N_{on}(\nu)$ is the amount of detected ions when IR light is present. The collection $G(\nu)$, given by

$$G(\nu) = \frac{S(\nu)}{T_{win}(\nu)P_0(\nu)\Delta s(\nu)} \quad (2)$$

represents a set of parameters that is dependent on the wavelength of the light, with $S(\nu)$ the surface of the light beam [m^2], $T_{win}(\nu)$ the transmission of the window(s), $P_0(\nu)$ the initial power of the light [W], and $\Delta s(\nu)$ the laser pulse length [s]. Note that since absolute absorbance intensities are difficult to determine in a molecular beam experiment (all the parameters in $G(\nu)$ have to be measured online), usually only relative intensities are calculated. For experiments performed in this review, we take for eqs 1 and (2) that C = 1 and that $T_{win}(\nu)$, $\Delta s(\nu)$, and $S(\nu)$ are constant. This results in an equation for the absorbance of

$$A = \frac{\nu}{P_0(\nu)}\log_{10}\left(\frac{N_{off}}{N_{on}(\nu)}\right) \quad (3)$$

2.2. Experimental Implementations: Neutral Biomolecules in the Gas Phase

Molecules are typically brought intact into the gas phase via heating[16,141,153] or laser desorption.[140,154−166] Subsequently, the intact molecules are cooled down to their lowest rovibrational states by seeding them into a supersonic molecular beam expansion. Finally, the studied molecules are probed spectroscopically and detected by time-of-flight mass spectrometry. A number of research groups study neutral

https://dx.doi.org/10.1021/acs.chemrev.9b00547
Chem. Rev. 2020, 120, 3233−3260

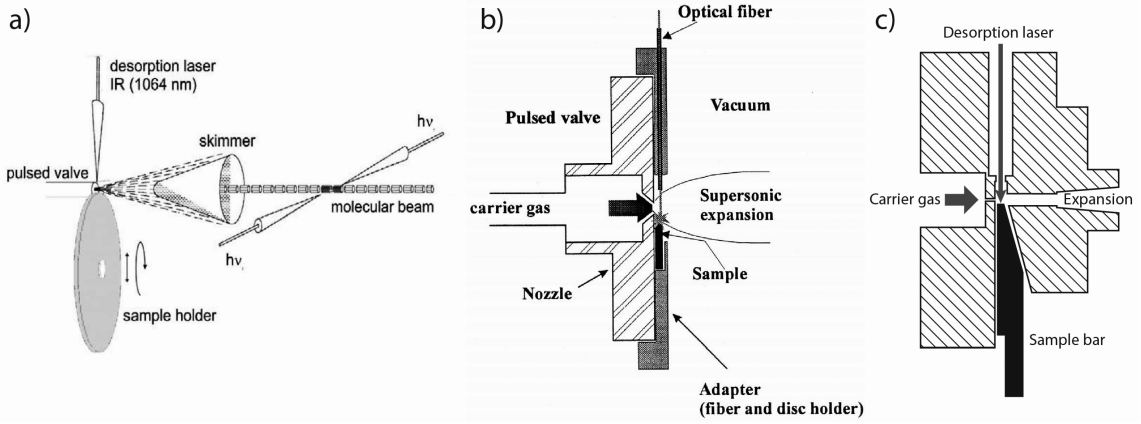

Figure 6. Three possible laser desorption sources: (a) rotating disk (reprinted with permission from ref 158. Copyright 2003 Elsevier); (b) pressed pellet (reprinted with permission from ref 160. Copyright 2000 Elsevier); (c) sample bar with (optional) additional expansion as used in the Rijs group.

biomolecules in the gas phase by means of IR laser spectroscopy, thereby mainly focusing on the 3 μm and fingerprint region. The general principle of the laser desorption–molecular beam setups used by these groups is the same as for the in Figure 5 presented far-IR experiment. Minor differences between the laser desorption sources used in various research groups will be briefly discussed in the next paragraphs.

2.2.1. Laser Desorption. Nonvolatile molecules or thermally labile molecules such as peptides and other biomolecules can be brought intact into the gas phase using laser desorption coupled to a molecular beam.[154,164,165,167] The particular implementation of the laser desorption source varies between the several research groups. Typically, the molecules are deposited on the surface of a matrix, typically a graphite sample bar, which stimulates the intact desorption. Besides the choice of sample bar material, variations can be found in (i) sample preparation, i.e. deposition, mixed, doped, premixed, and pressed; (ii) sample bar shape, i.e. rods, bars, pressed discs, etc.; and (iii) the choice of desorption laser wavelength and power.

In general, the studied molecules are being deposited on the surface of a (graphite) sample bar, which is placed just in front of the orifice of the nozzle of a pulsed valve. A low intensity, nanosecond laser, most often a Nd:YAG laser operating at the fundamental (1064 nm) or second harmonic (532 nm) wavelength is mildly focused on the surface of the sample bar. This sample bar is translated with a stepper motor to ensure that new sample is provided at each laser shot. The intact, neutral gas-phase molecules are then directly cooled by the supersonic expansion of argon. The desorption mechanism can be described by laser-induced thermal desorption, where the graphite matrix plays a passive role as energy transmitter. The nanosecond desorption laser pulse introduces a very high heating rate in the order of 10^{11} K/s, which allows the sample molecules to desorb intact from the surface instead of fragmenting.[1,168−173] It should be noted that a higher laser power and thus higher heating rate does not necessarily result in an improved signal; it might result in a larger amount of desorbed molecules, but this can easily disturb the supersonic expansion and the cooling conditions.[1]

Different laser desorption sources have been developed by the various groups active in this field. Fujii[148,156] et al. and Kleinermanns[158] et al. both use a rotating disk as shown in Figure 6a, with the sample either mixed with graphite and pressed as a disk or deposited on the lateral side of the disk. The rotation ensures a fresh sample every laser shot. While a pressed disk allows long measuring time, it is of importance to have a very stable round disk since slight fluctuations in the roundness will lead to large fluctuations in the signal. The group of Michel Mons uses a pellet, pressed from a mixture of graphite and molecule in a 4:1 ratio,[8,160,174−177] as shown in Figure 6b, which can be translated linearly to provide new sample every laser shot. A disadvantage of the use of a pressed pellet or disc is the large amount of material that has to be used. A third possible sample matrix is a cylindrical graphite rod, comparable to the one used in the Smalley sources, as is used by the groups of Müller and Fernández.[147,166] Lastly a graphite sample bar, in a similar fashion linearly translatable as the pellet from Mons, is used by groups of de Vries,[154,155] Rijs,[1,6,13,34,40] Küpper,[159,178] Zehnacker,[179,180] and Zwier.[141,181] Here, the sample is deposited on the surface of a graphite sample bar; therefore, only a submilligram quantity of the sample is required. Typically, the sample is premixed with graphite or carbon black in a 1:1 ratio. Moreover, with the addition of an air-lock to the setup, a linear sample bar alignment allows for quick change of sample. An example of a source using a sample bar as used in the group of Rijs is presented in the inset of Figure 5. Figure 6c shows a novel modification of this source, where an extra section is placed behind the desorption region to advance cooling and cluster formation. Küpper and co-workers designed a fully translational laser desorption source in the x, y, and z directions to combine with their deflection setup which allows for spatial separation of conformers using electrostatic deflection.[159,178] Additional differences between the various laser desorption setups can be found in the type of molecular beam valves that are used. Predominantly, a General Valve (Parker) with either a 0.5 or 0.8 mm diameter nozzle is employed, with the exception of for example the group of Fujii (Even–Lavie valve),[182] the groups of Küpper and de Vries (cantilever piezo valve),[183] and the groups of de Vries and Rijs (Jordan valve).

2.2.2. Molecular Beams. In order to record high-resolution far-IR spectra, thermally evaporated or laser desorbed molecules are cooled into their rotational and vibrational ground state using a molecular beam. A supersonic expansion of inert carrier gas, such as helium and argon, is

https://dx.doi.org/10.1021/acs.chemrev.9b00547
Chem. Rev. 2020, 120, 3233−3260

created by expanding the gas from a high-pressure reservoir into a region of (high) vacuum. Supersonic jets have been present since the 20s of the previous century.[184,185] Molecular beam sources are nowadays considered a very reliable and efficient technique to cool down molecules for spectroscopic investigations.[186]

In the experiments discussed here, molecules are laser-desorbed into the collision zone of a pulsed supersonic expansion. The molecules are seeded in the carrier gas pulse, and in this expansion, the sample molecules are accelerated in the same direction as the seed gas atoms. This translational cooling takes place directly at the nozzle−desorption interface. Subsequently, low energy collisions occur, decreasing the internal energy of the large molecules. This process cools the internal degrees of freedom of the seeded molecules, so that the ensemble of molecules becomes both rotationally (1−10 K) and vibrationally (15−50 K) cold, strongly depending on the mass and complexity of the molecule.[154,163,173,187−189] The cooling that occurs in the supersonic expansion is strongest immediately after the pulsed valve and decreases further downstream, so that the temperature asymptotically approaches its final value at about a distance of about 25−30 nozzle diameters downstream from the valve. The choice of the carrier gas is also of importance: Generally, more efficient cooling is obtained for larger molecules using heavier carrier gas.[155] Apart from that, it should always be taken into account that some atoms tend to form complexes with the molecules being studied, which can lead to additional observed conformers.[190]

The peptides discussed in this review often can adopt multiple conformations. It is assumed that these different conformations are populated according to a Boltzmann distribution at a temperature of about 500 K before they are cooled by the molecular beam expansion.[191−194] This cooling effectively freezes the peptides in local energy minima conformers as adopted due to the Boltzmann distribution. However, they are able to convert to lower energy structures when the interconversion barrier is low enough to cross. A rule of thumb that can be used for this interconversion barrier is 800 cm^{-1}. This means that in the end a mix of conformers can exist that comprises the thermodynamically most stable conformers but also kinetically trapped conformers.

2.2.3. Time-of-Flight Mass Spectrometry. After the neutral molecules are desorbed and cooled by the combined laser desorption and molecular beam approach, they are typically excited and ionized in a (1 + 1) REMPI process; see section 2.1.1. The mass-to-charge ratio of the formed ions can then easily be detected in a time-of-flight mass spectrometer (TOF-MS), as introduced by Wiley and McLaren.[195] This also allows identification of the mass of interest and to discriminate over formed fragments, clusters, and other ion signals resulting from contaminations. The ions of interest are accelerated using charged plates into a field free flight tube. The potential energy of the ions is converted to kinetic energy. A relation can then be made between the time (t_{TOF}) that the ions fly from the moment of entering the flight tube and its mass over charge via

$$t_{TOF} = \frac{L}{v} = \frac{L}{\sqrt{2U}}\sqrt{\frac{m}{z}} = k\sqrt{\frac{m}{z}} \quad (4)$$

with t_{TOF} the flight time in seconds, L the length of the field free region of the time-of-flight tube, and v the velocity of the ion. The kinetic energy is converted to the charge (z) times the electric potential difference U. Under the assumption that the electric field is homogeneous and that the molecules are ionized halfway between the repeller and extractor plate (see Figure 5), U is equal to $\frac{1}{2}(V_R + V_E)$, with V_R and V_E the voltage on the repeller and extractor plate, respectively. This can be summarized in the proportionality constant k, which depends on the TOF and its settings, and the mass over charge ratio (m/z), allowing easy calibration with molecules with known m/z values. Ions are detected using multichannel plate detectors, which create electron cascades after ion impact. An important improvement to the time-of-flight mass spectrometer came in the 70s when the reflectron was introduced.[196] This configuration is positioned at the end of the TOF tube, shown in Figure 5, and consists of a series of cylindrically shaped electrodes with a gradually increased DC bias voltage which reflects the ions, thereby both increasing the length L of the TOF tube as well as correcting for ions with different initial velocities. This enhances the mass resolution considerably.[197] It should be noted that the above equations follow a simple approximation for a single potential difference and the multiple charged plates in the detector make for a more complex potential landscape within the flight tube. However, the travel time of an ion still follows $t \propto \sqrt{\frac{m}{q}}$ and since all other parameters are constant within a single measurement, accurate mass separation is possible.

2.2.4. Far-IR Laser Sources: Use of the FELIX Free Electron Lasers. Free electron lasers offer the possibility to explore the low frequency vibrational motions of (bio)-molecules. Since the absorption cross section of the long wavelength vibrations for biomolecules is typically very low compared to the vibrations in the fingerprint region, these high intensity IR sources with a wide tunability are needed. For far-IR spectroscopic purposes, the most utilized free electron lasers are the FELs in Berlin (Fritz Haber Institute),[91,198] Nijmegen (FELIX),[90,199] and Orsay (CLIO),[89,200] from which the latter two are open user facilities. These free electron lasers all have a typical micro- and macro-pulse structure. For the experiments discussed in this review, the Free Electron Laser for Infrared eXperiments (FELIX) has been used. FELIX has typical macropulse energies of 50−200 mJ and covers the region between 2.7 and 150 μm, or 67 cm^{-1} to 3700 cm^{-1}, with approximately a spectral bandwidth of 0.5% of the energy in wavenumbers.

3. THEORETICAL APPROACHES

3.1. Overview and General Introduction of Theoretical Methods

The two main aspects in the theoretical calculations for gas-phase infrared spectroscopy are (1) to find the relevant 3D conformations and rank them by increasing order of energy (potential energy or free energy, including entropic effects) and (2) to calculate infrared spectra for a selection of these conformers in order to assign the experimentally observed spectroscopic fingerprints to 3D structures. Usually, the conformers with lower energies are selected at this stage. We are briefly reviewing both of these issues and will especially emphasize on DFT-MD dynamical IR spectroscopy and its advantages for the far-IR and THz spectral domain where vibrational anharmonicities and mode couplings have to be carefully assessed in order to achieve a 1-to-1 theory−experiment comparison. All theoretical strategies reviewed hereby rely on classical nuclei; that is, the nuclei are not treated

https://dx.doi.org/10.1021/acs.chemrev.9b00547
Chem. Rev. 2020, 120, 3233−3260

at the quantum mechanical level but rather are treated as classical particles. Whenever the term "classical" is employed in our text, it strictly refers to "classical nuclei".

Finding minima on the potential energy surface (PES) of gas-phase molecules and clusters nowadays relies on the following general strategies. In a first stage, a dynamical exploration of the potential energy surface is performed, typically using a classical level of representation of the interactions through force field molecular dynamics simulations (FF-MD). Sufficiently high temperatures (or internal energies) are employed in order to ensure an exhaustive conformational sampling of the PES, which is especially essential for floppy gas-phase biomolecules. This step is followed by clustering of the explored conformations into families of 3D-structures, ranked by increasing order of energy (at this level of representation), thus providing a first conformational screening of the PES. A certain number of these structural families are subsequently subjected to geometry optimizations using a more precise quantum level of representation of the interactions, typically at the DFT level for a rather good compromise between accuracy and computational cost. Of course, higher levels of quantum representations can be applied at this second stage, their use being limited only by computational costs. An intermediate step consisting of a semiempirical electronic representation could also be applied, before the more computationally costly DFT level, in order to improve the first conformational screening. Semiempirical MD can also be used for the first conformational screening. These steps ensure that a large number of minima on the PES can be found, using appropriate minimization algorithms. As a final stage, clustering of the optimized 3D-structures leads to a final energy ranking of the conformations at the highest level of electronic representation one can computationally afford.

Harmonic frequencies have to be calculated in order to check that the conformations hence generated are minima on the potential energy surface. Such strategies can be found in e.g. refs 1, 2, 8, and 201−216 for various gas-phase molecular systems. Exploring and localizing minima on the PES are nowadays a routine performed by all well-known classical MD and quantum chemistry packages (e.g., GROMACS, LAMMPS, Schrodinger suite, Gaussian, TURBOMOLE, ADF, Gamess, NWChem, ORCA, and for most other popular packages used in the gas-phase community). In the literature the theoretical methods and algorithms used for conformational searches on potential energy surfaces are discussed.[207,217] Note that MD simulations can also be coupled to more elaborate techniques such as parallel tempering, thereby enhancing the phase space sampling. In order to assign the 3D structure that is responsible for the experimental IR features, the IR frequencies will be calculated for a selection of the (lower energy) conformations found on the PES. The long-standing paradigm in the gas-phase community, which view has been challenged within the past few years, is that the lowest energy conformation should be the one providing the (best) match to the experimental spectrum. Experimentally, the formation of the lowest energy conformation is driven by a balance between kinetic, enthalpic, and entropic effects. A good example here is cis/trans isomerization of amide bonds.[218,219] Enthalpy will favor the formation of the lowest (enthalpy) energy structure in which typically a maximum of hydrogen bonds can be formed, while these conformers might not be entropically favored. Higher (enthalpy) energy conformers can be entropically favored instead. Added to that, kinetic effects specific to the experimental conditions (and presumably also system dependent) can be entering into the final balance, driving away from the formation of the lowest energy conformer. Kinetic trapping of high energy conformers has indeed been found increasingly more relevant.[43,179,220−227]

Conformational mixing can be included by a Boltzmann weighting of the individual static (harmonic or anharmonic) IR spectra or can be directly accounted for through molecular dynamics simulations (for sufficiently low energy barriers separating the conformers). In the following section, we will only review the calculation and assignment of vibrational anharmonic spectra through finite temperature molecular dynamics simulations, especially within the DFT (density functional theory) electronic representation. DFT-MD anharmonic vibrational spectroscopy is the main methodology applied up-to-now in interpreting far-IR/THz gas-phase vibrational spectra of flexible peptides, as reviewed in the application sections of this paper. We refer the reader to a recent review[207] where one can find details and discussions on the merits and some limitations on the calculation of static harmonic IR spectra and on discussions over static anharmonic spectra calculations, especially on using VSCF/VCI methodologies. The more recent papers by Bowman et al.,[228−230] Gerber et al.,[231] Barone et al.,[232] and Sibert et al.[233] provide up-to-date perspectives on method developments on static anharmonic spectra calculations.

3.2. DFT-MD for Vibrational Spectroscopy

Within the well-known time-correlation function formalism in linear response theory,[234,235] a dynamical IR absorption spectrum is obtained via

$$I(\omega) = \frac{2\pi\omega(1 - e^{(-\beta\hbar\omega)})}{3\hbar cV} D(\omega) \int_{-\infty}^{+\infty} dt e^{i\omega t} \langle \delta\mu(t) \cdot \delta\mu(0) \rangle \tag{5}$$

where $\beta = 1/kT$, ω is the frequency of the absorbed light, c is the speed of light in vacuum, V is the volume of the system, $\hbar$ is Planck's constant, $\mu(t)$ is the instantaneous dipole moment vector of the system at time t, $\delta\mu(t) = \mu(t) - \langle\mu\rangle$ is the fluctuation with respect to the mean value and $\langle ... \rangle$ refers to the equilibrium time correlation function (i.e., equilibrium trajectories). In this equation $D(\omega)$ is a quantum correction factor, multiplying the classical line shape to correct for the violation of the detailed balance conditions by the classical treatment of nuclei and to account for zero-point motion effects related to the presence of hydrogen atoms. It is an empirical correction, which we have shown to be chosen equal to $\frac{\beta\hbar\omega}{1 - e^{-\beta\hbar\omega}}$.[236] This correction is one of the most reliable empirical corrections from the literature.[236−238] Only IR intensities are affected by this term. With such correction, one ends up with the following equation, written either in terms of time correlation function of the dipole moment fluctuations or in terms of the time correlation function of the dipole moment derivatives fluctuations:

$$\begin{aligned} I(\omega) &= \frac{2\pi\beta\omega^2}{3cV} \int_{-\infty}^{+\infty} dt e^{i\omega t} \langle \delta\mu(t) \cdot \delta\mu(0) \rangle \\ &= \frac{2\pi\beta}{3cV} \int_{-\infty}^{+\infty} dt e^{i\omega t} \left\langle \delta\left(\frac{d\mu(t)}{dt}\right) \cdot \delta\left(\frac{d\mu(0)}{dt}\right) \right\rangle \end{aligned} \tag{6}$$

https://dx.doi.org/10.1021/acs.chemrev.9b00547
Chem. Rev. 2020, 120, 3233−3260

We refer elsewhere[207,229,239,240] for details on the advantages and limitations of dynamical anharmonic spectra calculations over static harmonic/anharmonic spectra calculations.

No harmonic approximations have been made in eq 6, neither on the potential energy surface nor on the dipole moment. The only ingredients are the time evolution and fluctuations of the dipole moment of the molecular system, which are naturally obtained from MD simulations. There is therefore no need for any harmonic expansion of the transition dipole moment, nor for normal modes, in contrast to static (an)-harmonic calculations. Importantly, the vibrational modes and their frequencies are therefore not directly related to the curvature of the potential energy surface at the minima, but rather to the time evolution of the electric dipole moment of the molecular system. This is governed by the conformational dynamics at the finite temperature of the simulation. Put in other words, dynamical−anharmonic IR calculations through eq 6 only rely on the time evolution of the dipole moment of the molecule, while static−harmonic IR calculations rely both on the geometry of the molecule on a minimum stationary point on the potential energy surface (PES) and on the diagonalization of a Hessian matrix to extract the frequency modes. These latter hence require an accurate calculation of the (PES) at the minimum energy geometry, as the frequencies of the vibrational modes directly reflect the curvature of the PES at this minimum stationary point. That is not the case for the dynamical−anharmonic IR calculations; there, the PES is not directly included in any of the terms in eq 6. Instead, what has to be described accurately is the dipole moment surface and, more than that, the fluctuations in time of this dipole moment. As a consequence, dynamical anharmonic spectra and static harmonic spectra rely on strictly different properties, and dynamical/static spectra presumably require different levels of accuracy for the evaluation of the underlying properties.

Hence, the use for very accurate PES at a high quantum level of representation[241,242] might not be needed for dynamical spectra, instead accurate dipolar surfaces[86,243,244] or accurate "on the fly" calculations of dipole moments[207,245] are required. Note also that the fluctuations of the molecular dipole moment are the ingredients in eq 6 rather than the absolute dipole moment values. The peak positions, intensities, and shapes directly follow from eq 6. In particular the shape and broadening of the peaks result from the underlying dynamics, e.g. conformational/isomeric dynamics, H-bond dynamics, etc., and the mode-couplings sampled at a given temperature (internal energy).

Regarding the DFT-accuracy used for the electronic level of representation in all trajectories presented throughout this work; it is shown that the BLYP-D2/D3[246−248] level of representation provides a robust electronic representation for dynamical spectroscopy, transferable from gas-phase molecules and clusters,[13,207,239,249,250] to liquid water and aqueous peptides[236,251] to inhomogeneous solid−water and air−water interfaces.[252−254] Using BLYP-D3, far-IR/THz spectroscopy of gas-phase peptides typically shows sharp IR peaks and on average 7−10 cm^{-1} deviations of the dynamical IR band-positions from the IR-UV ion dip experimental peaks, while deviations of the order of 20−40 cm^{-1} can be obtained in the mid-IR region.[13,86,87] Higher levels of DFT, especially hybrid functionals (typically B3LYP, PBE0, or HSE06) increase the computational costs of the DFT-MD trajectories significantly, while their merits for dynamical vibrational spectroscopy of gas-phase molecules have not been proved.[255] All trajectories discussed here are obtained with classical nuclei; however, the IR line shapes are corrected for quantum nuclei effects through the prefactor in eq 6, which allows us to have confidence in the rather small deviations in the peak positions between DFT-MD IR spectra and experiments.

The initial conditions for the molecular dynamics, i.e. the positions and velocities of the atoms, are respectively taken from geometry optimizations and a Boltzmann distribution centered at a given temperature T. A more elaborate distribution of the kinetic energy within the vibrational modes can be achieved at the initial time of the trajectory, thereby mimicking zero point energy (ZPE) quantum effects.[228,256−258] Leakage of the ZPE between the modes is however observed in such (classical nuclei) trajectories,[258−260] thus not conserving the ZPE per vibrational mode.

3.3. Graph Theory and Assignment of the Far-IR Vibrational Modes

Assigning vibrational modes from MD simulations is not an easy task, and several methods have been developed with variable success.[261−267] None of these methods are routinely used by the MD spectroscopic theory community. Recently, an alternative theoretical method has been developed that combines atomic polar tensors (APT)−weighted dynamical IR spectral calculations and graph theory.[87] Such methodology overcomes well-known issues on the equipartition of energy within the vibrational modes that impedes a reliable extraction of "effective normal modes" from the MD trajectories while it directly reveals all couplings between the molecular motions (these couplings being, by construction, absent from the "effective normal modes" analyses in the literature). In a nutshell, and as shown in ref 268, eq 6 can be rewritten into

$$I(\omega) = \frac{2\pi\beta}{3cV}\sum_m \frac{\partial\mu}{\partial R_m}\frac{\partial\mu}{\partial R_m}\int_{-\infty}^{+\infty} dt e^{i\omega t}\langle \dot{R}_m(t)\cdot\dot{R}_m(0)\rangle + \frac{2\pi\beta}{3cV}\sum_m\sum_{l\neq m}\frac{\partial\mu}{\partial R_m}\frac{\partial\mu}{\partial R_l}\int_{-\infty}^{+\infty} dt e^{i\omega t}\langle \dot{R}_m(t)\cdot\dot{R}_l(0)\rangle \quad (7)$$

where $\langle \dot{R}_m(t)\cdot\dot{R}_m(0)\rangle$ and $\langle \dot{R}_m(t)\cdot\dot{R}_l(0)\rangle$ are respectively the self- and cross-correlation functions of the derivatives of the internal coordinates ($3N - 6$ nonredundant internal coordinates (IC)) and $\frac{\partial\mu}{\partial R_l}$ are the derivatives of the dipole moment with respect to the internal coordinates. Within a transformation these latter are the equivalent of APTs obtained in Cartesian coordinates (and readily extracted from e.g. the Gaussian quantum chemistry package). The IC velocities $\dot{R}_l(t)$ ($\forall l$ and $\forall t$) are calculated by numerical derivation with a five points central difference algorithm.

Equation 7 shows that the IR spectrum of any molecular system can be decomposed into components arising either from each IC (self-part in eq 7) or from its correlation with any other ICs (cross-part in eq 7). The most important advantage of eq 7 is that all self- and cross-terms take into account the IR activity of each of these components into the final decomposition, thanks to the APT components in the prefactors (i.e., $\frac{\partial\mu}{\partial R_m}$). As a consequence, each IR band located at frequency ω_x within the $I(\omega)$ total spectrum can be decomposed into well identified self- and cross-correlation contributions as follows:

https://dx.doi.org/10.1021/acs.chemrev.9b00547
Chem. Rev. 2020, 120, 3233−3260

$$IR(\omega_x) = \sum_{m,l} I_{IC_{ml}}(\omega_x) = \sum_{m} I_{IC_m}(\omega_x) + \sum_{m,l\neq m} I_{IC_{ml}}(\omega_x) \quad (8)$$

Cross-correlations and their Fourier transforms, $\langle \dot{R}_m(t)\cdot \dot{R}_l(0)\rangle$ in $I_{IC_{ml}}(\omega)$, can be positive or negative depending on the relative phase of the motions of the two ICs, therefore $I_{IC_{ml}}(\omega)$ can likewise be positive or negative. The contribution of each spectral component $I_{IC_{ml}}$ into the active $IR(\omega_x)$ band is furthermore given by the normalized weight $w_{ml} = \frac{I_{IC_{ml}}(\omega_x)}{IR(\omega_x)}$. In practice, the surface area of each of the peaks in the $IR(\omega)$ spectrum is reconstructed from the sum of the $I_{IC_{ml}}$ surface areas responsible for that particular peak. This is only possible because the $I_{IC_{ml}}$ possesses the proper IR activity. With this, we know which internal coordinates contribute to each IR band and the percentage of participation of each $I_{IC_{ml}}$ into the final IR band through the w_{ml} weights. This provides the individual contributions of the internal coordinates into the intensity of that particular band. Such reconstruction includes both the self-part contribution of the internal coordinates as well as all cross-parts, which is the main issue in reconstructing the full IR activity of one given band. Cut-off values for including contributions are applied.[87]

By applying graph theory to the decomposition of the IR intensity bands described above, $I_{IC_{ml}}(\omega_x)$ self- $(m = l)$ and cross- $(m \neq l)$ contributions to any given $IR(\omega_x)$ IR band are presented by a colored indirect graph, in which the vertices are composed of the self-terms and the edges are given by the cross-terms. In these graphs the weight of each of these self- and cross-terms is assigned to the corresponding vertex/edge of the graph, directly providing the composition of the anharmonic mode at a given ω_x frequency. There is one graph per IR band, see Figures 12 and 13 in section 5.2 and Figure S5 for examples.

Various aspects of the graph theory are highly advantageous when using this theory for mode assignments. As soon as the graph is plotted, one can immediately see the self- and cross-term contributions of the internal coordinates into the given vibrational mode. Moreover, the graphs also directly visualize whether a vibrational mode is constructed of coupled or uncoupled internal motions; that is, a graph is made of connected elements and/or disconnected elements. By the number of connected elements in the graph, the localized or delocalized character of a mode can be determined. The weights displayed on the graph provide the information on the "electronic" vs "mechanic" couplings at play in the motions in a very efficient way. ICs can be mechanically correlated without participating in the final IR. In that case, the weight of the edge on the graph would have a high value but low or even zero value on one of the connected vertices. The ultimate advantage of the graphs is the natural capability for comparing graphs and hence extract similarities, ideal for comparing vibrational modes within one molecular system or between molecular systems, as is illustrated in section 5.2.

4. CHARACTERIZATION OF THE FAR-IR SIGNATURES OF DIPEPTIDES

4.1. Secondary Structure of Dipeptides

The first far-IR ion dip experiments on neutral, isolated dipeptides aimed to unravel whether structural information could be extracted from their far-IR signatures.[86] Until then, the far-IR region was not commonly employed to study the secondary structure of peptides in the gas phase, owing to the absence of strong tunable far-IR light sources, the low intensity of the vibrational transitions, and the difficulty in assigning the observed modes by quantum chemical calculations. To advance far-IR ion dip spectroscopy and to learn about the nature of the soft delocalized vibrations in biomolecules, a series of capped Ac-Phe-AA-NH_2 dipeptides was studied. These dipeptides all contain a phenylalanine (Phe) residue, which was used as UV chromophore for resonance enhanced excitation and ionization, and a second, variable amino acid residue (AA); glycine (Gly), alanine (Ala), proline (Pro), cysteine (Cys), serine (Ser), or valine (Val). These dipeptides have been studied in detail by IR-UV ion dip spectroscopy in the mid-IR amide A, amide I, and II regions, revealing their structural preferences and conformations present.[142,175,269,270] This series is therefore a good test for (i) the feasibility of far-IR ion dip spectroscopy providing an indication of what signal strengths can still be measured and (ii) the current static and dynamical DFT-based theoretical methods and their performance in the far-infrared spectral domain. Once the theoretical method is validated, the origin of the far-IR vibrational modes can be revealed.

The capped Ac-Phe-AA-NH_2 dipeptides typically fold in either a γ-turn (C7) or a β-turn (C10) geometry; see Figure 7,

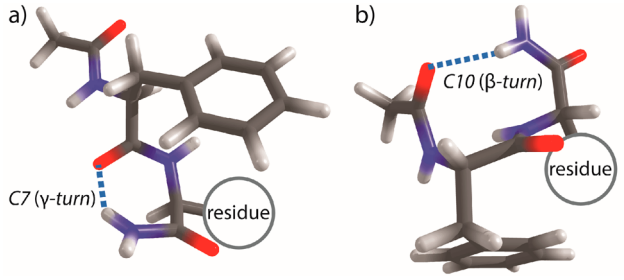

Figure 7. Typical conformational structures of Ac-Phe-AA-NH_2 dipeptides showing (a) a γ-turn, enclosing a ring of 7 atoms and (b) a β-turn, enclosing a ring of 10 atoms. Colors: Red, oxygen; blue, nitrogen; dark gray, carbon; and light gray, hydrogen.

where the NH_2 terminal cap is actively participating in this intramolecular hydrogen bond interaction. The C7 γ-turn is formed by hydrogen bonding between the C═O group of residue i and the NH group of residue $i + 2$ or, for the dipeptides here, between C═O(i) and the NH group of the NH_2 end-cap. These short-range C7 hydrogen bond interactions are relatively strong, compared for example to the weak nonlinear C5 interactions. In the short dipeptides studied here, a C10 (β-turn) results from hydrogen bonding between the C═O group from the C-terminus cap and the NH moiety from the NH_2 cap (see Figure 7b). Previous studies, using mid-IR ion dip spectroscopy combined with static DFT calculations, have shown that, under typical molecular beam conditions, the γ-turn conformer is observed for the Ac-Phe-Gly-NH_2, Ac-Phe-Ala-NH_2 and Ac-Phe-Ser-NH_2, and Ac-Phe-Val-NH_2 dipeptides. For the latter (Val), two conformers were identified, both with a γ-turn structure differing by the orientation of the $-CH(CH_3)_2$ residue with respect to the backbone. For both Ac-Phe-Cys-NH_2 and Ac-Phe-Pro-NH_2 two main conformations have been identified: one conformer with an intramolecular hydrogen bond leading

https://dx.doi.org/10.1021/acs.chemrev.9b00547
Chem. Rev. 2020, 120, 3233−3260

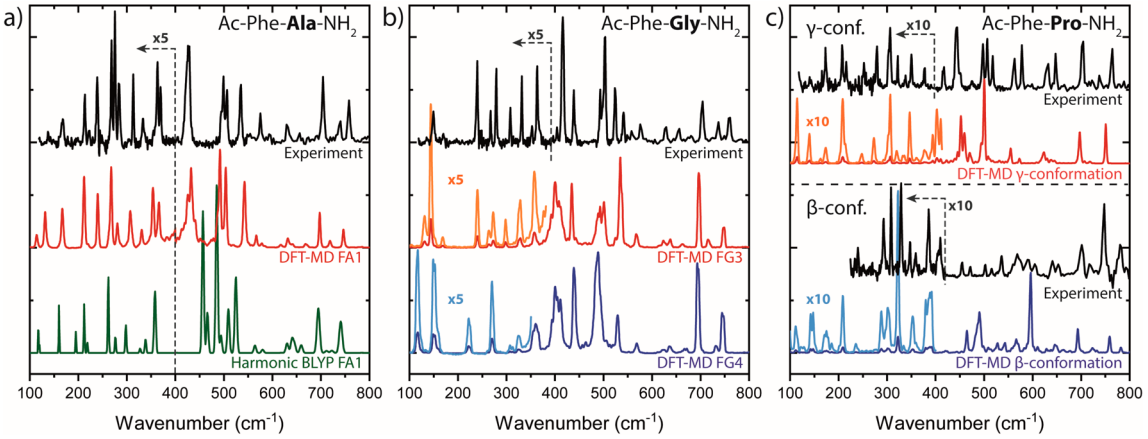

Figure 8. (a) Experimental spectrum (black) of Ac-Phe-Ala-NH_2 and DFT-MD (red) and harmonic calculated spectra (green) of its assigned structure; (b) Experimental spectrum (black) of Ac-Phe-Gly-NH_2 and DFT-MD calculated spectra of two different conformers FG3 (red) and FG4 (blue). Both (a) and (b) adapted with permission from ref 86. Copyright 2014 John Wiley and Sons. (c) Experimental spectra (black) of two conformers of Ac-Phe-Pro-NH_2 (γ-conformer upper panel, β-conformer lower panel), and their assigned DFT-MD spectra in color. Adapted with permission from refs 14 and 86. Copyright 2015 The Royal Society of Chemistry.

to the formation of a ten membered ring (β-turn) and one to a seven membered ring (γ-turn).[142,175,269,270]

4.2. Far-IR Spectroscopy of Dipeptides

4.2.1. Spectral Assignment Using Far-IR Ion Dip Spectroscopy and DFT-MD Calculations. The far-IR part of the absorption spectrum of gas-phase peptides was in many aspects still an uncharted territory. The first reported far-IR spectra, on the single amino acid tryptophan, did not provide explicit information on the modes present.[137,138] Successively, a study on capped phenylalanine−water clusters did report on the conformer selective intermolecular modes of the hydrates; however, they noted that the current level of theory was not sufficient for a detailed structural analysis.[139] In the past years, the far-IR has been explored, focusing on the above-mentioned series of capped Phe-AA dipeptides. All spectra are obtained as described in section 2.1.2 using the free electron laser FELIX as the IR source. As can be seen from the black trace of Figure 8a the far-IR spectrum of Ac-Phe-Ala-NH_2 shows a wealth of well-resolved, narrow, and rather intense peaks throughout the complete far-IR region recorded down to 100 cm^{-1} with typical line widths of about 3 cm^{-1} (fwhm),[86] limited by the bandwidth of the free electron laser. Synergy between experimental observation and theoretical calculated spectra is essential to obtain structural information from these low frequency motions. To go beyond the insufficient static DFT calculations, dynamical DFT-MD (section 3.2) was employed to structurally assign the obtained far-IR spectra. Ac-Phe-Ala-NH_2 was assigned by Mons et al. to a γ-turn structure based on the amide A (3 μm) region.[142] The excellent agreement between the observed far-IR experimental spectrum (black trace) with the dynamical DFT-MD spectrum calculated for the assigned FA1 γ-turn structure (red trace) confirms this assignment; see Figure 8a. The far-IR vibrations are extremely well reproduced by the dynamical DFT-MD spectrum, especially in the region below 500 cm^{-1} with deviations between experiment and theory of maximum 10 cm^{-1} (which lies almost within the spectral resolution). At the 500−800 cm^{-1} region the agreement is still very good, although slightly increased deviations were observed from the experiment.

In contrast, the static, harmonic DFT calculated spectrum (green trace) was not able to accurately reproduce the far-IR signatures. Significant deviations from the experiment were observed, for both the B3LYP as well as the BLYP functional, especially for the 400−600 cm^{-1} region. Below 400 cm^{-1} several peaks were not predicted or band positions are significantly misplaced by the static DFT calculations. The B97-D functional performed reasonably well in the far-IR regime for this Ac-Phe-Ala-NH_2 dipeptide, while in earlier work it was found that also the B97-D functional had significant problems in predicting the delocalized far-IR vibrations in amino acids and peptide−water clusters.[7]

Recently, additional calculations using BLYP with the D3 empirical dispersion factor were performed for the Phe-AA dipeptides discussed in this review; see Figure S2. In general, as expected, the addition of the D3 term shows an improvement over the static calculations without the D3 term. These initial results show that the static DFT spectra with dispersion correction can be used to understand the far-IR signatures of peptides with limited or weak interactions. This is consistent with the findings for Z-Ala-OH discussed in section 5.1. However, the static-DFT spectra do not provide a consistent picture; for example, they do not provide a good agreement with the far-IR spectra of NAPA−water[7] or have an unreliable prediction for the N−H bending vibrations in the Phe-AA dipeptides.

4.2.2. Unprecedented Structural Far-IR Fingerprints. Figure 8b presents the experimental far-IR spectrum of Ac-Phe-Gly-NH_2 (FG) (in black) together with the dynamical DFT-MD spectra of two iso-energetic conformers.[86] The experimental spectra reveal well-resolved, narrow peaks down to 100 cm^{-1}. The dynamical spectra of the two FG conformers show that only the FG3 (red trace) calculated peaks coincide with the experiment. The unique peak pattern between 100 and 350 cm^{-1} is well-reproduced by the dynamical DFT-MD spectrum of FG3 and not at all by FG4 (blue trace). Although these two iso-energetic γ-turn conformations, a C7-equatorial (FG3) and C7-axial (FG4) conformer, give indistinguishable mid-IR spectra, their far-IR signatures are unique. This particular experiment showed that the far-IR brings unprecedented structural details on the present conformations and the dynamical DFT-MD spectra can be used for conclusive structural assignment.

https://dx.doi.org/10.1021/acs.chemrev.9b00547
Chem. Rev. 2020, 120, 3233−3260

4.2.3. Far-IR Conformational Selectivity. The third example assesses the conformational selectivity of far-IR UV ion dip spectroscopy.[14] These studies focused on the far-IR signatures of the dipeptide Ac-Phe-Pro-NH_2. Experiments performed in the 3 μm region, probing the NH stretch vibrations, have shown that the backbone of this peptide can be folded in two conformations, namely a γ-turn (C7) or a β-turn (C10) geometry.[175] These two conformations coexist after laser desorption in the molecular beam. The mass- and conformer-selective experimental far-IR spectra of the C7 (top trace) and C10 conformer (bottom trace) are presented in Figure 8c together with their DFT-MD spectra (red and blue trace, respectively). Both experimental spectra show many well-resolved peaks in the far-IR region with typical peak widths of 3 cm^{-1}, limited by the free electron laser, as was observed for Ac-Phe-Ala-NH_2 and Ac-Phe-Gly-NH_2 as well. Similar to previous experiments on this dipeptide family, theory and experiments show a remarkable agreement. Most theoretical band shapes, positions, and intensities match with the experiment; however, it was observed that some bands either lack intensity or carry too much intensity. This latter issue is well-known in gas-phase MD simulations because of the difficulty of achieving equipartition in the rather short time-scales of the DFT-MD, hence possibly affecting the intensities of IR bands of certain modes. One of the main goals of this combined experiment/DFT-MD study was to provide conformer selective signatures for the γ-turn versus β-turn conformers in the far-IR region. As is shown in Figure 8c, the 400−550 cm^{-1} domain provided this distinction between the two conformations, where a 30−40 cm^{-1} red shift is observed for the hydrogen bond signatures of the weaker C7 γ-turn.[13] This region predominately shows NH out-of-plane/wagging motions, thereby indirectly probing the NH···O hydrogen bond motions (see section 4.3).

4.3. Insights on Dipeptides from the Far-IR Region

Besides calculating the IR spectra in order to obtain insight in the 3D conformation present in the experiment, it is key to understand the origin of the modes that contribute to observed IR absorption peaks. This can be visualized by a similar approach as was used to calculate the IR spectrum. Instead of using the total dipole moment of the system (see eq 4), the intramolecular coordinate−time correlation function (named ICDOS) is determined:[86]

$$I_{ICDOS}(\omega) = \int_{-\infty}^{\infty} \sum_i \sum_j \langle IC_i(t) IC_j(0) \rangle e^{i\omega t} dt \quad (9)$$

where $IC_i(t)$ is the time evolution of the selected internal coordinate i. This intramolecular coordinate can for instance be a bond length, e.g. the C═O bond length to study the C═O vibration, a dihedral angle, as used for wagging motions or even large-scale motions, where the distance between two atoms far apart is selected to look at backbone "breathing" vibrations. Only autocorrelation functions ($i = j$) were included for the calculation of these spectra; cross-correlations and couplings between internal coordinates can be calculated but they were ignored in the presented work. Note that they were taken into account in the dynamics. Equation 9 gives the position in frequency of the selected internal coordinate, but the quantification of how much this particular internal coordinate contributes to the observed peak is not determined. Furthermore, when taking the time correlation of the intramolecular coordinate, the change in dipole moment is not included in this equation; for example, selection rules for vibrational spectroscopy are not taken into account. Equations 7 and 8 in section 3.3 do include the change in the dipole moment derivatives and would include the correct intensity of each band. However, this has not been included in the analyses presented with eq 9 in this work, as here the focus lied only on assigning the motions of the modes.

The first studies focused on finding discriminating modes as highlighted above for Ac-Phe-Pro-NH_2. To generate a universal understanding of the type of motions in the far-IR domain, similarly as is present for the mid-IR fingerprint region, a general map of the motions that are responsible for the spectroscopic signatures recorded in the far-IR domain has been developed; see Figure 1. Several possible structural selective modes from the Ac-Phe-AA-NH_2 dipeptides series have been evaluated. Two types of modes are found in the far-IR/THz domain, i.e. local modes, where only one major coordinate is involved in the motion, and delocalized modes, which are a result of a large number of internal coordinates. The far-IR spectra of all the studied Ac-Phe-AA-NH_2 dipeptides together with their DFT-MD of the assigned conformers are summarized in Figure S1.

4.3.1. Localized Modes. The local modes found in the far-IR spectral range are predominantly out-of-plane wagging motions of the hydrogen atoms, i.e. ω(NH), ω(CH), ω(SH), and ω(OH), and hindered rotational motions of CH_3 groups. The ICDOS spectra of the dihedral angles have proven to be well suited to visualize these motions since one atom has a major contribution to the wagging motion.[13]

4.3.1.1. ω(CH) of the Phenylalanine Ring (700−750 cm^{-1}):[13] Two types of ω(CH) out-of-plane vibrations of the phenyl ring from in the phenylalanine residue are observed, i.e. in-phase modes, where the variation in dipole moment of the individual CH moieties add up resulting in intense far-IR peaks, and out-of-phase modes, where the dipole moment variations cancel each other out. The latter were only observed when coupled to other internal coordinates. For all the capped Ac-Phe-AA-NH_2 dipeptides, three absorption bands were identified by the ICDOS analysis at 710, 730, and 750 cm^{-1}.[13] Although different interactions are present in the various dipeptides, such as $(NH)_{AA}$−π interaction for the γ-turns with AA = Gly, Ala, Cys, Ser, and Val and for the β-turn of Ac-Phe-Cys-NH_2 or the proline ring−π interaction for both the γ- and β-turn for Ac-Phe-Pro-NH_2, the ω(CH) out-of-plane bending motions constantly appear at the same frequencies. This indicates that the ω(CH) modes are unique for these phenyl ring out-of-plane bending modes, but they are not conformer selective as they do not depend on the local peptide environment. These findings were later confirmed with the studies on the Ac-Phe-OMe monomer and dimer.[87]

4.3.1.2. ω(NH) Out-of-Plane Wagging Modes:[13] The ICDOS analysis showed an amide V wagging signature for each of the two backbone NH amide groups. The $\omega(NH)_{Phe}$ mode is located between 470 and 510 cm^{-1} (highlighted in blue) and the $\omega(NH)_{AA}$ wagging between 530 and 640 cm^{-1} (gray); see Figure 9. The $\omega(NH)_{Phe}$ is observed within a window of 40 cm^{-1}, which is not surprising as for all Ac-Phe-AA-NH_2 dipeptides this NH_{Phe} group is involved in a weak C5 interaction with the $C{=}O_{Phe}$ moiety of the same Phe residue. For the β-turn (C10) conformer of Ac-Phe-Cys-NH_2, where the NH_{Phe} is free, the ω(NH) was found around 410−490 cm^{-1}. The $\omega(NH)_{AA}$ amide V vibrations appeared in a larger frequency window, and its position depends on the chemical

https://dx.doi.org/10.1021/acs.chemrev.9b00547
Chem. Rev. 2020, 120, 3233−3260

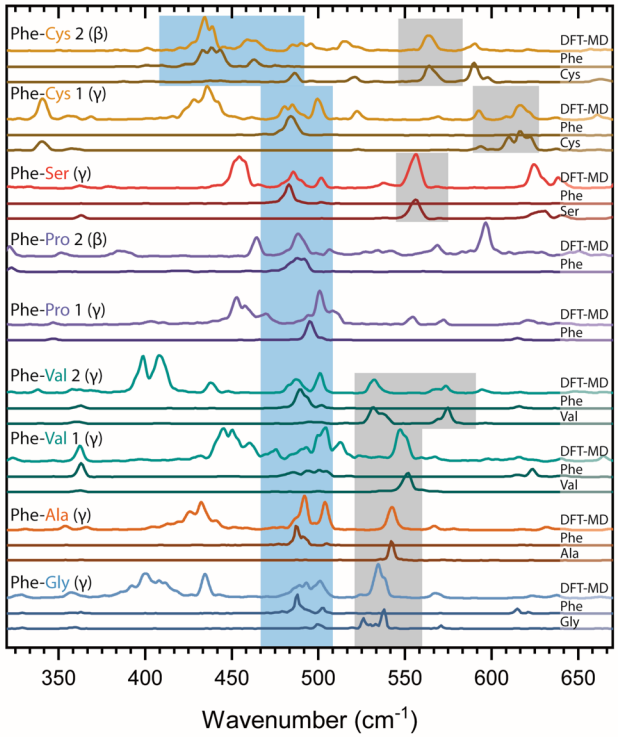

Figure 9. DFT-MD calculations of all dipeptides, together with the ICDOS of the NH out-of-plane wagging motions $\omega(NH)_{Phe/AA}$, as indicated on the right side of the graph. The positions of $\omega(NH)_{Phe}$ highlighted in blue and $\omega(NH)_{AA}$ in gray. Adapted with permission from ref 13. Copyright 2017 The Royal Society of Chemistry.

composition of the residue and interactions of this backbone NH with the rest of the peptide. For the γ-turns with AA= Gly, Ala, and Val (2×), there is a π-interaction between the NH_{AA} group and the phenyl ring. The corresponding $\omega(NH)_{AA}$ was identified at 530−550 cm^{-1}, showing a blue shift of about 30−50 cm^{-1} with respect to $\omega(NH)_{Phe}$. The same interaction is present for the γ-turns with AA = Cys and Ser. However, as a result of the different chemical nature of the side chain containing SH and OH groups, a supplementary blue shift is observed. For the β-turn conformation of Ac-Phe-Cys-NH_2, where NH_{Cys} has only a weak interaction with the phenyl ring, the $\omega(NH)_{Cys}$ mode is observed at 565 cm^{-1}. The out-of-plane wagging mode was shown to be a diagnostic vibration for the local structural environment around the NH backbone moiety and can be included as a valuable signature for the structural assignment of peptides. These findings were confirmed by a later study on the Ac-Phe-OMe β-sheet dimer.[87]

4.3.1.3. Other Local Modes:[13] The NH_2 moiety gives rise to symmetric and antisymmetric out-of-plane wagging motions. For the antisymmetric motion (580−720 cm^{-1}), the ICDOS showed a strong correlation between its frequency and the NH_2···O=C hydrogen bond length: The stronger the hydrogen bond, the more blue-shifted the antisymmetric out-of-plane wagging signature. This relation was not observed for the symmetric NH wagging motion (400−500 cm^{-1}). The ICDOS analysis was also used to identify other out-of-plane vibrations such as ω(SH) and ω(OH). The ω(OH) vibration of the Ac-Phe-Ser-NH_2 γ-turn was found at 557 cm^{-1}, while ω(SH) of the Ac-Phe-Cys-NH_2 γ-turn appeared at 340 and 369 cm^{-1}. For the β-turn conformation the ω(SH) showed activity at 288 and 310 cm^{-1}. These latter values confirm the blue-shift of the wagging motion with an increase in the strength of the hydrogen bond.

Two types of spectral signatures were identified for the hindered CH_3 rotational motions resulting from either the backbone methyl groups or the side chain methyl moieties present for AA = Val, Ala. Signatures of the terminal CH_3 group are found below 100 cm^{-1}, and the ICDOS shows that they are systematically coupled collective, delocalized modes. The side chain methyl moieties appear at higher frequencies and are typically observed in the 220 to 260 cm^{-1} window.

4.3.2. Delocalized Backbone Modes (0−400 cm^{-1}). Collective vibrational modes delocalized over the peptide backbone are present at the full far-IR range; however, their intensity dominates the range 0−400 cm^{-1}. The most prominent motions are the bending (100−400 cm^{-1}) and torsional (0−100 cm^{-1}) large amplitude and collective motions, which are coupled and delocalized over the peptide backbone. For the dipeptides, these motions were followed by the ICDOS analysis of backbone dihedral angles. Multiple signatures of each internal coordinate were observed in the spectra, and several dihedral angles provided the same spectral signature; that is, they were observed at the same frequency. This indeed indicates that the modes are collective and delocalized over the peptide backbone. Although it is not possible to determine the percentage of participation of each internal motion to the final mode from the ICDOS, the ICDOS do reveal how many angles and dihedral angles are involved in a peak. Furthermore, principle component analysis (PCA) was used to indicate which internal coordinates are connected and which do contribute to specific observed peaks in the experimental IR spectrum.[13]

4.3.3. Hydrogen Bond Signatures (0−250 cm^{-1}). Studies on substituted benzenes revealed two diagnostic vibrational modes related to hydrogen bond strengths in the far-IR, namely the hydrogen bonded OH torsion (ω(OH)) and the hydrogen bond stretching (ν(H-bond)) modes.[85] For the dipeptides, the hydrogen bond signatures have not yet fully been explored. Initial studies show that the hydrogen bond motion can be addressed via three internal coordinates, namely (i) the ν(H-bond) corresponding to the ICDOS of the hydrogen bond length, (ii) the angle NH···O δ(H-bond), and (iii) the dihedral angle NH···O=C ω(H-bond). These modes are however strongly coupled to other motions, complicating direct analysis.[255]

All the discussed far-IR motions for peptides are summarized in Figure 1 together with well-known mid-IR vibrational modes.

5. PEPTIDE CLUSTERS

Peptide clusters are of interest in a wide range of research fields, ranging from biomedicine to bioengineering.[271−274] A well-known example is the aggregation of partly unfolded peptides into long, organized fibrillary structures, as is observed to coincide with a number of neurodegenerative diseases.[275−277] Elucidation of the structures of small peptide clusters in the gas phase can shed light on the mechanisms that are fundamental to the aggregate formation processes. It is not trivial to prepare neutral peptide clusters in the gas phase, and since the pioneering work of Gerhards et al. on the dimer of Ac-Phe-OMe,[143] only a few papers have been published on dimers.[132,278−280] Recently Rijs et al. demonstrated the formation of higher order peptide clusters up to the tetradecamer formed in a molecular beam via laser desorption.[6]

https://dx.doi.org/10.1021/acs.chemrev.9b00547
Chem. Rev. 2020, 120, 3233−3260

The presented studies mainly focused on the mid-IR using the amide A, I, II, and III modes for structural assignment. The position of the peaks depends on the hydrogen bond interactions and is well characterized both experimentally and theoretically.[142]

As the size and complexity increases, and hence the number of intra- and intermolecular interactions, structural elucidation becomes more challenging. The combination of mid-IR spectroscopy and static quantum chemical calculations results in the identification of structural families such as for example conformers with parallel beta-sheets, rather than providing an assignment to one specific structure with known exact orientations of side groups and side chains,[132] a direct result from the increasing spectral congestion. The experiments in this section show that it is insightful to include the far-IR region, especially for peptide clusters as intermolecular hydrogen bonds are probed in this far-IR regime. These bands possibly contain a wealth of extra information on the hydrogen bonded complexes. In order to relate the observed peaks to specific modes, quantum chemical calculations are essential. Results on phenol-like molecules[129] showed that static DFT works well for molecules with no or only weak interactions. This relation is examined for peptides as well, using a small peptide and its dimer; see sections 5.1 and 5.2. In general, static DFT works well to predict the far-IR spectrum of the observed monomer conformation for the simplest peptides only. For Ac-Phe-OMe, the far-IR is necessary to determine the orientation of the phenyl side-chain (see section 5.2). For the peptide dimers the static calculations start to fail to predict certain peaks, when strong intermolecular interactions begin to play a role, and for these more anharmonic modes DFT-MD becomes more important. Moreover, recently Galimberti et al. explored the experimental and theoretical signatures in the far-IR of the monomer and dimer formation of Ac-Phe-OMe, initially studied in the mid-IR by Gerhards et al.[143,280,281] The newly developed graph theory (see section 5.2) was shown to be a novel method to reveal the character of the observed far-IR modes.[87]

5.1. Static-DFT versus DFT-MD for a Simple Peptide and Its Dimer

5.1.1. Z-Ala Monomer. Z-L-alanine−OH, abbreviated as Z-Ala (m/z 223.2), is a simple capped peptide, with the N-terminus containing a Z-cap to introduce the required UV chromophore for the IR-IDS experiments. Z-Ala is a molecule that is easy to desorb and ionize via (1 + 1) REMPI at 37589 cm^{-1}. The REMPI spectrum, see Figure S3, shows one dominant peak, which was used to obtain the far-IR spectrum (black trace of Figure 10a). Using both the mid- and far-IR regions, this IR spectrum is assigned to a linear β_L structure (lowest in energy). It has the Z-capped group pointing in the same direction as the alanine side-group. Both static DFT (B3LYP-D3/6-311++G**) and dynamic DFT-MD calculations (details are provided in section 3.2) have been performed on the assigned structure, and their calculated IR spectra are shown in Figure 10a in green and red, respectively. A scaling factor of 0.976 was used to correct for anharmonicity in the static DFT spectrum. This is the same scaling factor as was used in the mid-IR region and provides the best possible overlap in both regions. The peaks above 500 cm^{-1} are generally better described by the scaled static DFT calculations; below 500 cm^{-1} DFT-MD has a slightly better agreement regarding the peak positions. For the monomer of

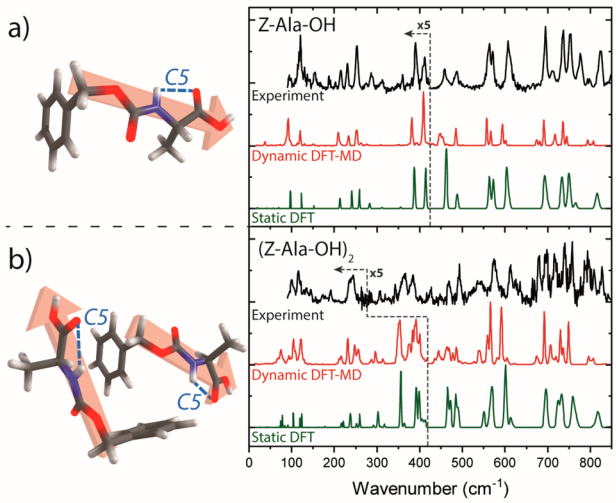

Figure 10. Experimental far-IR spectra (black) of the (a) monomer and (b) dimer of Z-alanine−OH, together with DFT-MD (red) and static DFT (green) spectra of their assigned structures. A scaling factor for the static spectra of 0.976 is used. On the left side the assigned structures of the monomer and dimer are shown, with arrows indicating the direction of their backbones.

Z-Ala both calculation methods perform well, even for the NH out-of-plane bending region around 450 cm^{-1}. The absence of strong intramolecular hydrogen bonding can explain this lack of anharmonicity and thus the good overlap of the static DFT spectrum with experiment.

5.1.2. Z-Ala Dimer. The dimer of Z-Ala shows a broadened REMPI spectrum with respect to the monomer (see Figure S3), with its main transition at 37420 cm^{-1}. Compared to the monomer, where only weak intramolecular hydrogen bonds are involved in the β_L structure, the dimer can contain stronger intermolecular hydrogen bonds. An extensive conformational search was performed to map the conformational landscape. However, none of the calculated mid- and far-IR spectra of the low energetic structures showed a reasonable overlap with experiment, while only a few of the considerably higher energetic structures (over 42 kJ/mol higher) show good agreement. The common denominator of these latter structures is that all the monomeric units within these dimers have the same orientation of the backbone as the assigned monomer (β_L) and are part of the same structural family. This is in line with previous findings, where it was demonstrated that the structures of the monomers are largely retained in the dimeric structures, favoring the stronger intermolecular hydrogen bonds over the weaker intramolecular hydrogen bonds.[132] However, the monomeric peptides forming the dimer are not engaged in intermolecular hydrogen bonding; that is, they are only connected through weak ring interactions.

The experimental, static, and dynamic DFT spectra are presented in Figure 10b. Both calculated spectra have a good agreement with the experimental IR spectrum, especially when compared to other structural families; see Figure S4. The dynamic DFT-MD spectrum agrees better below 400 cm^{-1}, with especially the peaks around 100 cm^{-1} being predicted well. The static DFT spectrum on the other hand is slightly better above 400 cm^{-1}, most notably the two peaks around 470 cm^{-1}. The frequencies of the set of peaks between 650 and 800 cm^{-1} are better predicted by the dynamical spectrum, but intensities by the static DFT. The differences between the two

https://dx.doi.org/10.1021/acs.chemrev.9b00547
Chem. Rev. 2020, 120, 3233−3260

spectra are minimal; only minor alternations between the two computational approaches are observed.

Far-IR action spectroscopy on dipeptides, as discussed in section 4, can be a powerful tool in combination with dynamic DFT-MD calculations. Static DFT is not able to predict the far-IR vibrations for these relatively strong intramolecularly hydrogen bonded dipeptides. The Z-Ala monomer is different in this respect as it is only weakly hydrogen bonded (C5 interaction), leading to a better agreement with static DFT. The dimer of Z-Ala is an interesting case since it does not adopt the lowest energy structure but appears to be a weakly bonded complex of two β_L monomers via π-interactions rather than hydrogen bonds. This explains the observed similar static DFT and the dynamic DFT-MD spectra in Figure 10b, where no large differences are observed, also not in the 400−550 cm^{-1} region. As observed before,[132] the conformational search for dimers and higher order clusters is challenging, since the heating step in simulated annealing often results in breaking of the intermolecular hydrogen bonds. However, extensive conformational searches have to be performed in order to find the exact conformation. For this particular example, where the two monomers are frozen into their β_L structures and are not changing their structures in order to form stronger intermolecular hydrogen bonds, static DFT would be sufficient. For other systems, such as the strong hydrogen bonded parallel beta-sheet dimer Ac-Ala-Ala-OBn,[6] DFT-MD would be required in the far-IR to explain all the band positions.

5.2. Use of Graph Theory on Ac-Phe-OMe and Its β-Sheet Dimer

The peptide Ac-Phe-OMe is a known model for β-sheets in the gas phase.[87,143,280,281] The REMPI spectrum of the Ac-Phe-OMe monomer shows a wealth of highly resolved peaks resulting from a single conformer.[87,143] As was previously observed for all the dipeptides presented in section 4, the experimental far-IR spectrum showed many narrow far-IR peaks with their widths depending on the bandwidth of the free electron laser (black trace in Figure 11a). The DFT-MD (details in section 3.2) calculated spectrum of the assigned $\beta_L(g^+)$ conformer (red) and the $\beta_L(g^-)$ conformer (blue) is included in Figure 11a. The theoretical spectrum of $\beta_L(g^+)$ provides a remarkable agreement with the experiment, especially in the more conformer selective region 90−400 cm^{-1}.[13,14,86] Here, all peaks in this region result in delocalized bending motions along the backbone and the side chain.

The experimental far-IR spectrum of the dimer of Ac-Phe-OMe is obtained with the UV laser at 37538.5 cm^{-1} and is assigned to a $\beta_L(g^+)$-$\beta_L(g^-)$ configuration.[87] It is plotted in Figure 11b together with its DFT-MD calculated spectrum, again showing an excellent agreement. In the next section, we will discuss a number of selected IR bands below 800 cm^{-1} as an example of how graph theory can be used for the assignments of the modes. The graph theory method is described in section 3.3 of this review. By analyzing the graphs, insights can be obtained in which modes originate from the monomer peptides and which result from the interaction between both monomers forming the dimer.

5.2.1. NH Wagging Motion (450−650 cm^{-1}). The $\omega(NH)$ out-of-plane NH wagging motion is defined by the out-of-phase torsion of φ (labeled $-C8-N-$ in the graphs) and ω (labeled $-N-C9-$ in the graphs) using the current definitions of nonredundant internal coordinates (Figure 12a).

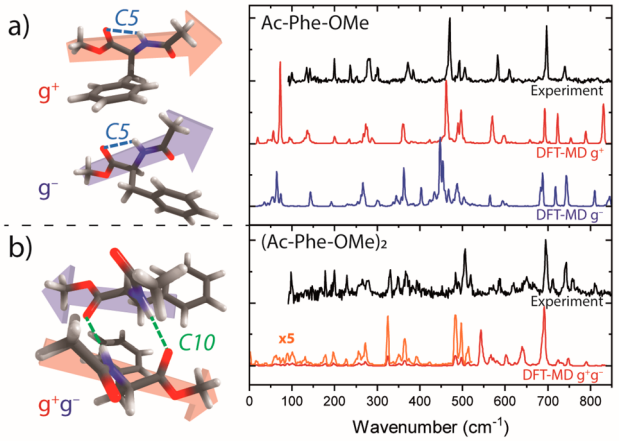

Figure 11. (a) Experimental spectrum (black) and DFT-MD calculated spectra (red for the g^+ conformer and blue for the g^- conformer) of the Ac-Phe-OMe monomer and (b) experimental spectrum (black) and assigned DFT-MD calculated spectrum (red) of the Ac-Phe-OMe dimer, together with their assigned structures. The arrows in the 3D structures indicate the direction of the backbone starting from the N-terminus. Adapted with permission from ref 87. Copyright 2019 The Royal Society of Chemistry.

The monomer graphs show that the IR peaks located at 463 cm^{-1} for the g^+ conformer and 453 cm^{-1} for g^- are dominated by the $\omega(NH)$ out-of-plane NH wagging (Figure 12b). The large values (i.e., 134 and 39 for g^+, 123 and 46 for g^-) of these two motions on the vertices of the two graphs indicate that these two modes are highly localized. Only small mechanical couplings with the backbone (values on the edges, −3 and 6) are found. The out-of-phase motion between the φ and ω torsions, which appears with large negative values at the edges, defines the out-of-plane wagging motion of the NH group.

There are two main bands in the assigned dimer conformer g^+-g^- that originate from the ω(NH) wagging motions, and are found at 542 and 640 cm^{-1} (Figure 12c). The dimer ω(NH) wagging motions are ∼100−200 cm^{-1} blue-shifted with respect to the monomer bands. This blue-shift is the result of the $NH\cdots O=C$ hydrogen bonds forming the β-sheet structure in the dimer. Blue-shifts in the ω(NH) out of plane wagging motions in the far-IR/THz domain were also observed for the dipeptides discussed in section 4 and are highlighted in Figure 1.

The graphs for the g^+-g^- dimer are more branched than the graphs for each monomer, illustrating the higher complexity arising from the intermolecular hydrogen bonded motions. The notation in the graphs with green circles carrying the ± sign indicates which monomer peptide in the dimer carries the motion, with ± for the g^+/g^- peptide in the dimer, respectively. The left part of Figure 12c shows the graph for the 542 cm^{-1} mode that is composed of a single graph of connected lines, with several colored connected vertices. The main contributors to this mode are both NH wagging motions ($-N-C9-$ and $-C8-N-$ for both g^+ and g^-), which are mechanically coupled (see the values on the edges in the graph). The values on the vertices also show that the NH on the g^- peptide strand dominates the motion, despite both NH wagging motions contributing to the final IR mode. The intermolecular hydrogen bond, indicated with the yellow vertex (NH···O1), is also coupled to the NH wagging motions and is a large contributor to the final activity of the mode. The right part of

https://dx.doi.org/10.1021/acs.chemrev.9b00547
Chem. Rev. 2020, 120, 3233−3260

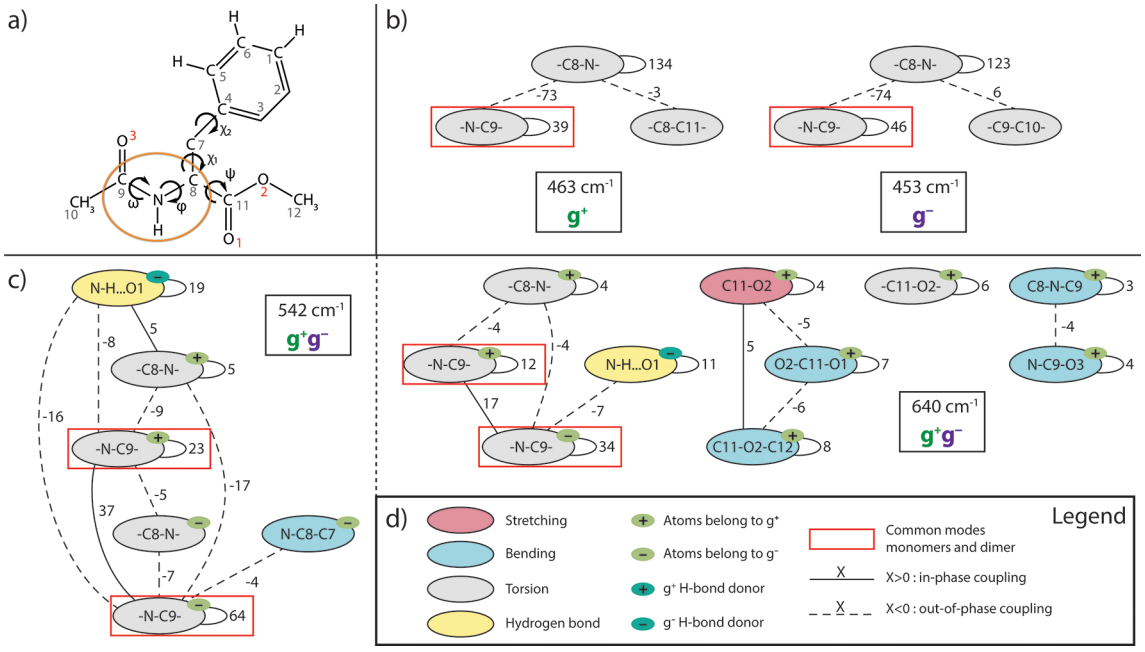

Figure 12. Graphs for the local ω(NH) wagging modes. (a) The orange circle highlights the dihedral angle involved in this motion. (b) The ω(NH) wagging mode for the g^+ and g^- monomers positioned at 463 and 453 cm^{-1}, respectively, and (c) ω(NH) wagging mode for the g^+g^- dimer at 542 and 640 cm^{-1}. (d) Legend and nomenclature. Adapted with permission from ref 87. Copyright 2019 The Royal Society of Chemistry.

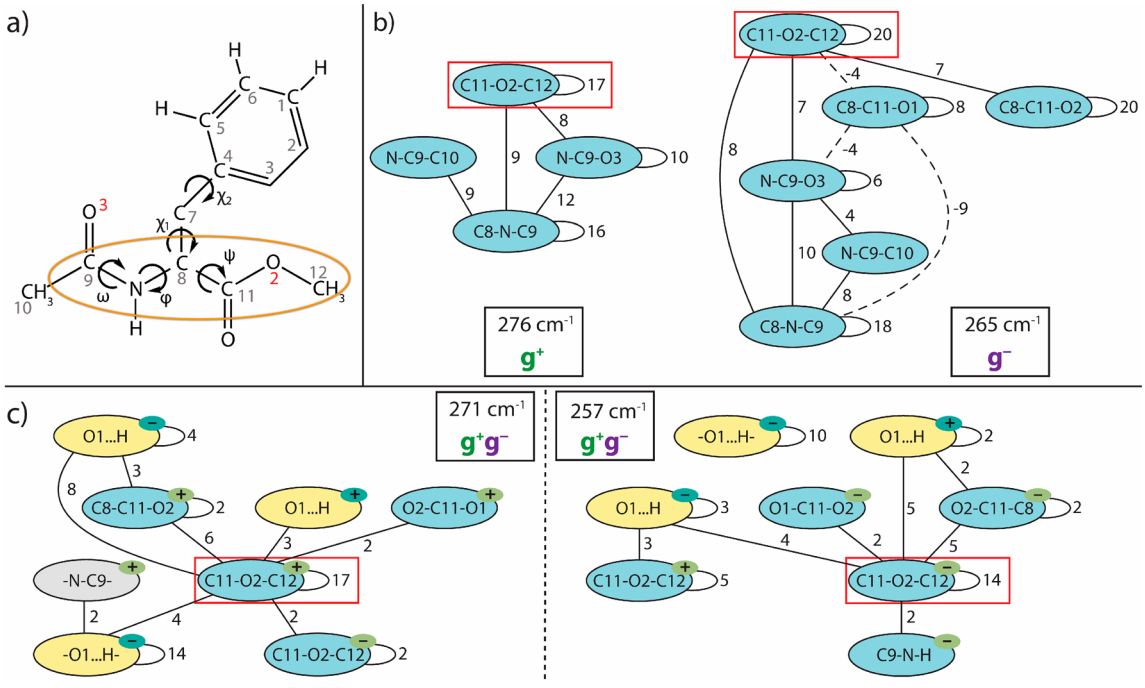

Figure 13. Graphs for delocalized backbone bending modes as shown in (a) for the (b) 276/265 cm^{-1} modes, respectively, for monomers g^+ and g^-, and (c) the 271/257 cm^{-1} modes for the g^+g^- dimer. See Figure 12d for the nomenclature. Adapted with permission from ref 87. Copyright 2019 The Royal Society of Chemistry.

Figure 12c shows the second mode at 640 cm^{-1}, assigned to the ω(NH) wagging motions, and consists of four disconnected subgraphs. The red rectangles in both graphs of Figure 12c show the similarities of the left subgraph of the 640 cm^{-1} mode to the 542 cm^{-1} mode, with the same coupling to the intermolecular hydrogen bond. Other minor contributing motions, which can be seen from the values next to the vertices, to the 640 cm^{-1} mode include C═O stretching and backbone bending modes, indicated by the red and blue vertices, respectively.

5.2.2. Delocalized Motions at 250−280 cm^{-1}. The graphs of the g^+ and g^- monomers corresponding to the peaks at 276 and 265 cm^{-1}, respectively, show highly delocalized modes distributed over several coupled bending motions of the backbones (Figure 13). The graphs of both peaks exhibit the same dominant contributions for the COC C-terminal bending (red rectangles) and for the CNC "central" bending of the

https://dx.doi.org/10.1021/acs.chemrev.9b00547
Chem. Rev. 2020, 120, 3233−3260

backbone, but also for the N-terminal N−C═O and N−C−C bending motions. The values on the edges of the graph of the 276 cm^{-1} mode of the g^+ conformer are positive, originating from in-phase coupled motions, while they can be positive or negative for the 265 cm^{-1} mode of g^- as a result of in-phase and out-of-phase couplings.

In the g^+-g^- hydrogen bonded dimer, the discussed delocalized modes of the two peptide monomers are shifted to 271 and 257 cm^{-1}, but they consist of similar contributions as was observed for the two individual monomers. Both modes are dominated by the COC C-terminal bending as indicated by the larger values on the *C11−O2−C12* vertices in both graphs. This contribution is highlighted with the red rectangles, one for g^+ (271 cm^{-1}) and one for g^- (257 cm^{-1}). Both COC C-terminal bending motions are systematically coupled to the intermolecular hydrogen bond motions, either through the intermolecular O···H stretching or the intermolecular − *O···H*− torsion. The COC C-terminal bending also couples to other backbone C-terminal bending motions, such as the OC═O and CCO bending motions. These can either be located on the same strand or on the other strand. The positive values on the edges of the graphs indicate the in-phase coupled motions. The "central" backbone CNC bending, which had a dominant contribution to the modes of both individual monomer conformations, does not participate in the dimer modes. This motion is inhibited by the intermolecular hydrogen bond in the peptide dimer. The contributions to the discussed delocalized modes are both of electronic and mechanical nature, as indicated by the nonzero values of the weights on the vertices and edges.

5.2.3. Torsional Delocalized Motions at ∼200 cm^{-1}. A final example in the low far-IR domain is a highly delocalized torsional mode for the g^+ monomer at 200 cm^{-1}, where the coupling between the backbone motions and the side chain bending is nicely visualized (Figure S5). Each of these two motions is mechanically coupled to several other torsion and bending motions; however, these couplings do not contribute to the final IR activity (as indicated by the lack of values on the associated vertices). Similarly, the dimer mode at 197 cm^{-1} also shows multiple, decoupled bending and torsional and hydrogen bonded motions.

The use of graph theory is a powerful tool in the assignment of far-IR modes. The graphs show how many motions (stretch, bending, torsion, or hydrogen bond) are involved in each vibrational mode by means of the number of vertices. It demonstrates whether the mode is constructed of localized or delocalized motions by the edges between the vertices. It specifies the number of coupled motions that participate in this mode, along with the weight each of the motions brings to the final IR mode. Graph theory makes it easy to compare between two graphs, which makes this method ideal to characterize the far-IR modes of peptide clusters. The evaluation of the monomer and dimer graphs provides information on (dis)-similarities between the far-IR modes.

6. OUTLOOK TO LARGER SYSTEMS

The application of far-IR spectroscopy with DFT-MD has proven to be successful for the structural analysis for medium-sized peptides and their aggregates as discussed in sections 4 and 5. The important next challenge would be to evaluate its use for larger peptides. In a preliminary study, the far-IR signatures of a series of capped polyalanine peptides, namely Z-Ala_3-NHMe, Z-Ala_4-NH_2, and Z-Ala_6-NH_2, are explored to unravel present intramolecular hydrogen bond stretching vibrations.[282] For all three peptides it holds that the far-IR spectra all show well-resolved peaks; even for the largest Z-Ala_6-NH_2 sharp peaks are observed in the region below 200 cm^{-1}, where the hydrogen bond stretching vibrations are expected (see Figure S6). Furthermore, for this review we have studied the far-IR response of gramicidin A and C, two 15 amino acid residue peptides, which were previously studied in the mid-IR in a collaboration with de Vries et al.[155,283]

6.1. Mini-proteins: How Large Can We Go in the Far-IR?

Gramicidin is found in the bacteria *Basillus Brevis* and is often used as an exemplar channel protein.[284−286] It is a linear polypeptide built up of 15 (hydrophobic) amino acids, with a formyl cap on the N-terminal side and an ethanolamine cap on the C-terminal side. Bacterial gramicidin is a mixture of three types of gramicidin which differ by the amino acid residue on the 11th position, resulting in gramicidin A (gA, with tryptophan on position 11), gramicidin B (gB, phenylalanine), and gramicidin C (gC, tyrosine). Additionally, each type also exhibits a minor second alteration (5−20%), where the valine residue on the first place is replaced by isoleucine. As can be seen from the mass spectrum in Figure 14, gA has the most

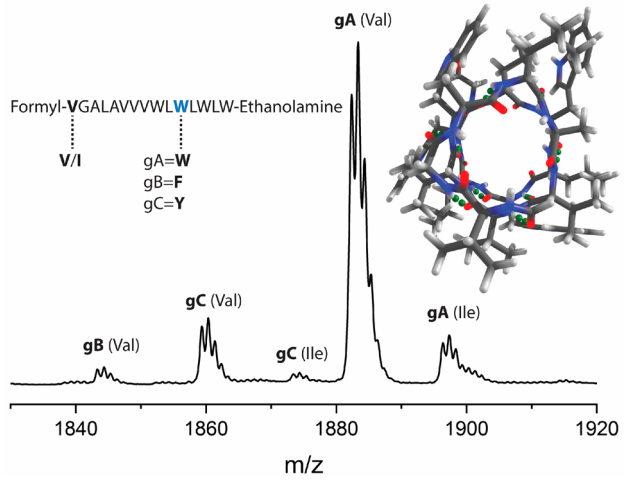

Figure 14. Mass spectrum of the gramicidin mixture, showing the distribution of gramicidin A, B, and C (gA, gB, and gC, respectively). The peptide sequence is shown on the left, and the assigned structure on the right, looking from the top through the channel.

dominant contribution (about 80%), followed by gC (15%) and only 5% of gramicidin is made up of gB. In contradiction to most natural occurring proteins, gramicidin contains not only L-forms but also D-isomers, in an alternating fashion.[287] In the condensed phase it is found that gramicidin forms a β-helix,[288] which is preserved in the gas phase as shown by the IR-UV ion dip experiments in the 3 μm region[283] and the 1000−1800 cm^{-1} fingerprint region.[155]

In this review, we present results on a recent far-IR study of gramicidin A and C. Gramicidin B was not included as the contribution of gB in the natural gramicidin sample is too low to record the far-IR with a decent signal-to-noise ratio. The far-IR spectra of gA and gC, recorded from 90 to 850 cm^{-1} are presented in Figure 15. In coincidence with the mid-IR results, the two far-IR spectra of gA and gC show strong resemblance, although the spectrum of gC appears somewhat noisier resulting from the lower contribution in the sample which

https://dx.doi.org/10.1021/acs.chemrev.9b00547
Chem. Rev. 2020, 120, 3233−3260

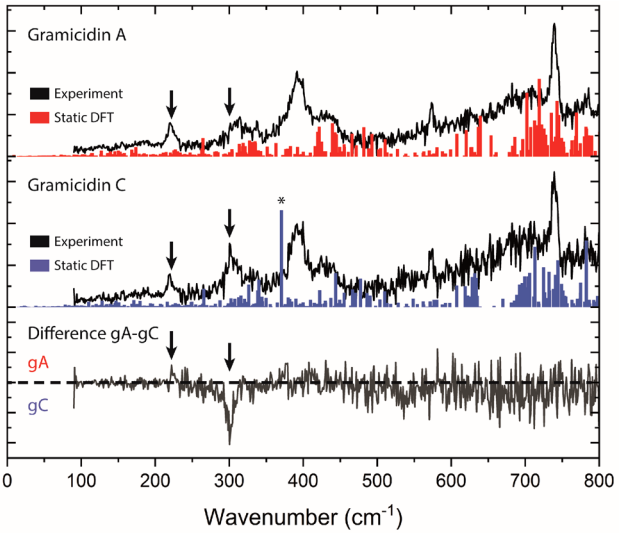

Figure 15. Experimental (black) spectra of gramicidin A (top) and C (middle panel), together with their static DFT calculations. The asterisk in the gramicidin C spectrum indicates the position of the OH torsional mode. The lower panel shows the difference spectrum between the two (gA−gC), meaning intensity below the zero line (black dots) is more intense for gramicidin C and vice versa. The two main deviations are indicated with the black arrows.

corresponds to a weaker UV signal. In the far-IR region a number of peaks can be distinguished from a broad continuous IR activity. A clear and intense peak at 739 cm^{-1} is observed and a second, smaller peak at 573 cm^{-1}. At lower frequencies a number of distinct bands can be observed: Two broader peaks at 429 cm^{-1} and a large one at 393 cm^{-1}, a feature around 305 cm^{-1} and a smaller peak around 220 cm^{-1}. In agreement with the experimental far-IR spectra, the static DFT calculations (at the DFT/SV(P) level of theory employing a TPSS functional)[155] show a similar large density of modes in this region with a few intense bands at specific frequencies. However, the exact positions of the calculated frequencies should be handled with care. Dynamic-DFT calculations are currently on their way.

Although at first sight the two far-IR spectra of gA and gC appear to be very similar, when their difference spectrum is plotted (gA minus gC), clear deviations between their two far-IR signatures appear; see the bottom panel of Figure 15. We highlight two main differences between the two spectra: a distinct higher intensity feature at 221 cm^{-1}, which is more pronounced for gA, and the most prominent difference with a gain for gC at 300 cm^{-1}. The increased band for gA at 221 cm^{-1} originates most likely from butterfly motions of the four tryptophan residues present in gA, whereas gC has only 3. A characteristic peak at 300 cm^{-1} is observed in gC with respect to gA (and also to gB, not shown here). Since these three varieties of gramicidin only differ in their sequences at the 11th position, this peak most likely results from the OH out-of-plane torsion of the tyrosine of gC.

The out-of-plane torsion vibration of the OH moiety in relation to its hydrogen bond strength has been extensively studied via far-IR experiments focusing on a number of phenol-like molecules, such as catechol and saliginin.[85,129] In phenol, in essence the same as the side group of tyrosine, the OH out-of-plane torsional mode was observed at 309 cm^{-1}, which was confirmed by both static (an)-harmonic and dynamic DFT calculations. As a result of this high similarity of the tyrosine residue with the unperturbed phenol, the similarities between the far-IR spectra of gA and gC, except for this peak, and the theoretical calculations point to a large contribution of this mode; see the star in the blue trace in Figure 15. We assign this peak to the out-of-plane torsional mode of a free OH group. This confirms that the tyrosine OH is not involved in hydrogen bonding.

These far-IR studies on large peptides and mini-proteins show that well-resolved signatures are still present when going to larger and more complex systems. Currently, DFT-MD calculations for gramicidin are under way. Gaigeot et al. have shown recently that DFT-MD can be routinely applied to molecular systems composed of >1000 atoms and on systems in the condensed phase, both of comparable or larger size than the molecules shown here.[253]

7. CONCLUDING REMARKS AND OUTLOOK

This review discusses the recent developments in far-IR action spectroscopy of neutral peptides. The use of far-IR light opened up a novel and complementary direction to provide insights into the structure of biomolecules. Additional vibrational modes, both local and delocalized, are available in the far-IR regime, often providing unprecedented structural characterization and insights in collective backbone motions of the studied peptides. We have provided a detailed overview of the various techniques that have to be employed to obtain the mass- and conformation-selective far-IR spectra (section 2) of cold, gas-phase peptides. The application of IR spectroscopy to larger molecules has relied on the significant experimental progress in the last few years. With advances in laser desorption, it is now possible not only to vaporize low vapor pressure small and medium-sized peptides intact into the gas phase but also to employ this method to large peptide aggregates and mini-proteins. The understanding of the observed far-IR signatures depends heavily on the interplay between experiment and theory. Coinciding with the experimental progress also the theoretical methods have been advanced for the far-IR analysis of large biomolecules (section 3). We have shown that finite temperature DFT-based molecular dynamics (DFT-MD) simulations is a suitable theoretical strategy for extracting local and delocalized modes, especially those that have an anharmonic character such as the out-of-plane wagging motions. The (an)-harmonic static DFT calculations work well in combination with the near- and mid-IR spectroscopy to assign the structure of biomolecules and to find a reasonable match between experiment and theory; however, they are inconsistent in predicting peak positions and intensities in the far-IR region. The work presented here shows that DFT-based molecular dynamics simulations are successful in elucidating the 3D structures of peptides (section 4), peptide clusters (section 5), and their interactions in the far-IR/THz spectral domain. We also review the use of graph theory for vibrational modes assignments, revealing the intra- and intermolecular motions responsible for these vibrational modes. It should be noted that the experimental and theoretical methods discussed in this review are not restricted to peptides only. Far-IR action spectroscopy has recently been applied to nucleobases, polyaromatic hydrocarbons (PAHs),[84] and (hydrated) benzene-derivatives[40,85] and has proven to be equally powerful for those systems as well.

The next important challenge is to evaluate the application of far-IR spectroscopy with DFT-MD for the structural analysis

https://dx.doi.org/10.1021/acs.chemrev.9b00547
Chem. Rev. 2020, 120, 3233−3260

of larger and more complex biomolecular systems. Where the mid-IR region of for example a hexapeptide is already congested with overlapping absorption bands, the far-IR regime still shows a striking collection of resolved absorption bands with a full width at half-maximum of 3 cm^{-1} down to 100 cm^{-1}. When moving toward the 15 amino-acid peptide gramicidin, spectral congestion also starts to play a role in the far-IR region. However, unique features are still present in the far-IR spectra (section 6). The use of DFT-MD does not only allow us to reveal the modes present in the far-IR; possible conformational dynamics present in the studied molecule are included in the simulation, provided that the energy barrier separating the conformations is low enough to surpass at a given temperature. Resulting signatures of conformational changes, which involve collective large amplitude motions, will be found in the far-IR regime. Currently, far-IR spectroscopy is only applied to study cold, neutral molecules. In recent experiments, we have shown that far-IR spectroscopy can be exploited in combination with room temperature mass spectrometry to study the far-IR signatures of deprotonated nucleotides; far-IR ion spectra down to 300−400 cm^{-1} using infrared multiple photon dissociation (IRMPD) were recorded.[209] As the field of gas-phase far-IR spectroscopy to probe biomolecular structure and structural changes is still relatively new, novel developments and research directions are expected to emerge from future endeavors.

ASSOCIATED CONTENT

Supporting Information

The Supporting Information is available free of charge at https://pubs.acs.org/doi/10.1021/acs.chemrev.9b00547.

Experimental far-IR spectra of dipeptides, their assigned DFT-MD spectra and additional static BLYP-D3 calculations; REMPI spectra, experimental and calculated IR spectra of the Z-alanine dimer; graph theory on delocalized torsional modes of the monomers and dimer of Ac-Phe-OMe; experimental far-IR spectra of larger alanine containing peptides (PDF)

AUTHOR INFORMATION

Corresponding Authors

Marie-Pierre Gaigeot − *LAMBE CNRS UMR8587, Université d'Evry val d'Essonne, 91025 Evry, France;* orcid.org/0000-0002-3409-5824; Email: mgaigeot@univ-evry.fr

Anouk M. Rijs − *Radboud University, Institute for Molecules and Materials, FELIX Laboratory, 6525 ED Nijmegen, The Netherlands;* orcid.org/0000-0002-7446-9907; Email: a.rijs@science.ru.nl

Author

Sjors Bakels − *Radboud University, Institute for Molecules and Materials, FELIX Laboratory, 6525 ED Nijmegen, The Netherlands*

Complete contact information is available at: https://pubs.acs.org/10.1021/acs.chemrev.9b00547

Notes

The authors declare no competing financial interest.

Biographies

Sjors Bakels received his B.Sc. in Natural Science and his M.Sc. in Science at the Radboud University in Nijmegen, The Netherlands, in 2013 and 2016, respectively. Currently he is a Ph.D. student in the group of Anouk M. Rijs at the FELIX Laboratory, located at the Radboud University in Nijmegen, where he studies different aggregation processes of peptides in the gas phase, by using infrared action spectroscopy to unravel their structures and structural changes upon aggregating.

Marie-Pierre Gaigeot is Professor at the University of Evry val d'Essonne—University Paris-Saclay in Paris, France. She is an expert in DFT-based molecular dynamics simulations applied to vibrational spectroscopies. She has been characterizing the vibrational spectroscopies of gas-phase molecules and clusters (IR-MPD, IR-PD, IR-UV ion dip), including the pioneering work reviewed here on THz vibrations of peptides and their aggregates, of the IR and Raman features of liquid water and immersed solutes, and of the challenging air/water and mineral/water SFG (sum frequency generation) spectroscopies at aqueous interfaces. The credo of the Gaigeot group is to systematically link theoretical spectroscopy with spectroscopic measurements, allowing a 1-to-1 comprehension of spectroscopic features and providing a comprehensive assignment of the features in terms of conformations. M. P. Gaigeot has also been for several years Subject Editor in Chemistry for the Royal Society Proceedings A, a member of the Editorial Boards of the Royal Society Proceedings A & Philosophical Transactions A, Spectrochimica Acta A, has been appointed recently at the Advisory board of Physical Chemistry Chemical Physics (PCCP), and is FRSC Fellow of the Royal Society of Chemistry.

Anouk Rijs is an associate professor in physical chemistry within the FELIX Laboratory of the Radboud University (Nijmegen, The Netherlands). She obtained her Ph.D. in femtosecond imaging and photoelectron spectroscopy from the Vrije Universiteit Amsterdam in 2003. During her postdoc period at University of Amsterdam and University of California Santa Barbara, she started to advance molecular spectroscopy to characterize complex molecules. She is an expert in infrared and terahertz action spectroscopy, interfaced with mass spectrometry and molecular beam technologies for large biomolecules. By focusing on the characterization of structure, molecular interactions, and probing structural changes, her group aims to obtain a fundamental understanding of protein folding interactions and the mechanism of peptide aggregation. Within the Radboud Consortium for Glycoscience, she has recently expanded these methods to carbohydrates and their glycosylation reactions. In addition to her work at Radboud University, she is the deputy-chair of the editorial board of Physical Chemistry Chemical Physics (PCCP) of the Royal Society of Chemistry and Fellow of the Royal Society of Chemistry.

ACKNOWLEDGMENTS

We gratefully acknowledge the Nederlandse Organisatie voor Wetenschappelijk Onderzoek (NWO) for the support of the FELIX Laboratory. We thank the FELIX team for their experimental support and helpful discussions. Calculations were performed at the SurfSARA Cartesius cluster under NWO Rekentijd contract 17603 or at HPC resources from GENCI-France under Grant N° 072484 (CINES/IDRIS/TGCC). No such works could have been achieved without the involvements of numerous Ph.D. and Post-Doctorate collaborators. We want to stress that most of our collaborators have been involved both in the experiments and in the simulations.

This is an important aspect of the experiment-theory investigations performed by our two groups. We are grateful to the former and current bachelor, master, and Ph.D. students of our two groups, who all contributed to the results described in this review. Among the Rijs experimental group, Sander Jaeqx, Bin Yan, Daniël Bakker, Vasyl Yatsyna, Sander Lemmens, and Kas Houthuijs, and among the Gaigeot theory group, Jérome Mahé, Daria Ruth Galimberti, and Sana Bougueroua are specifically acknowledged for their outstanding participations in the works reviewed here.

ABBREVIATIONS

AA	amino acid
Ala	alanine
APT	atomic polar tensor
BOMD	Born−Oppenheimer molecular dynamics
Cys	cysteine
DFT	density functional theory
DFT-MD	density functional theory−molecular dynamics
DNA	deoxyribonucleic acid
FEL	free-electron laser
FELIX	free-electron lasers for infrared experiments
FF-MD	force-field molecular dynamics
fwhm	full-width at half maximum
Gly	glycine
IC	internal coordinate
ICDOS	internal coordinate density of states
IR	infrared
IR-IDS	infrared ion dip spectroscopy
IRPD	infrared photon dissociation
IVR	intramolecular vibrational energy redistribution
MD	molecular dynamics
MS	mass spectrometry
NAPA	*N*-acetyl-phenylalanine-amide
Nd:YAG	neodymium-doped yttrium aluminum garnet
PCA	principle component analysis
PES	potential energy surface
Phe	phenylalanine
Pro	proline
REMPI	resonance enhanced multiphoton ionization
RIDIRS	resonant ion dip infrared spectroscopy
Ser	serine
THz	terahertz
TOF	time-of-flight
UV	ultraviolet
Val	valine
Z-cap	benzyl formate cap
ZPE	zero-point energy

REFERENCES

(1) Rijs, A. M., Oomens, J., Eds. *Gas-Phase IR Spectroscopy and Structure of Biological Molecules*; Springer, 2015.
(2) Schermann, J. P. *Spectroscopy and Modeling of Biomolecular Building Blocks*; Elsevier, 2007.
(3) Hoffmann, W.; Folmert, K.; Moschner, J.; Huang, X.; von Berlepsch, H.; Koksch, B.; Bowers, M. T.; von Helden, G.; Pagel, K. NFGAIL Amyloid Oligomers: The Onset of Beta-Sheet Formation and the Mechanism for Fibril Formation. *J. Am. Chem. Soc.* **2018**, *140*, 244−249.
(4) Scutelnic, V.; Perez, M. A. S.; Marianski, M.; Warnke, S.; Gregor, A.; Rothlisberger, U.; Bowers, M. T.; Baldauf, C.; von Helden, G.; Rizzo, T. R.; et al. The Structure of the Protonated Serine Octamer. *J. Am. Chem. Soc.* **2018**, *140*, 7554−7560.
(5) Seo, J.; Warnke, S.; Pagel, K.; Bowers, M. T.; von Helden, G. Infrared Spectrum and Structure of the Homochiral Serine Octamer-Dichloride Complex. *Nat. Chem.* **2017**, *9*, 1263−1268.
(6) Bakels, S.; Porskamp, S. B. A.; Rijs, A. M. Formation of Neutral Peptide Aggregates as Studied by Mass-Selective IR Action Spectroscopy. *Angew. Chem., Int. Ed.* **2019**, *58*, 10537−10541.
(7) Cirtog, M.; Rijs, A. M.; Loquais, Y.; Brenner, V.; Tardivel, B.; Gloaguen, E.; Mons, M. Far/Mid-Infrared Signatures of Solvent Solute Interactions in a Microhydrated Model Peptide Chain. *J. Phys. Chem. Lett.* **2012**, *3*, 3307−3311.
(8) Gloaguen, E.; Mons, M. Isolated Neutral Peptides. *Top. Curr. Chem.* **2014**, *364*, 225−270.
(9) Habka, S.; Sohn, W. Y.; Vaquero-Vara, V.; Geleoc, M.; Tardivel, B.; Brenner, V.; Gloaguen, E.; Mons, M. On the Turn-Inducing Properties of Asparagine: the Structuring Role of the Amide Side Chain, from Isolated Model Peptides to Crystallized Proteins. *Phys. Chem. Chem. Phys.* **2018**, *20*, 3411−3423.
(10) Habka, S.; Very, T.; Donon, J.; Vaquero-Vara, V.; Tardivel, B.; Charnay-Pouget, F.; Mons, M.; Aitken, D. J.; Brenner, V.; Gloaguen, E. Identification of Ion Pairs in Solution by IR Spectroscopy: Crucial Contributions of Gas Phase Data and Simulations. *Phys. Chem. Chem. Phys.* **2019**, *21*, 12798−12805.
(11) Jaeqx, S.; Du, W. N.; Meijer, E. J.; Oomens, J.; Rijs, A. M. Conformational Study of Z-Glu-OH and Z-Arg-OH: Dispersion Interactions versus Conventional Hydrogen Bonding. *J. Phys. Chem. A* **2013**, *117*, 1216−1227.
(12) Jaeqx, S.; Oomens, J.; Rijs, A. M. Gas-Phase Salt Bridge Interactions Between Glutamic Acid and Arginine. *Phys. Chem. Chem. Phys.* **2013**, *15*, 16341−16352.
(13) Mahe, J.; Bakker, D. J.; Jaeqx, S.; Rijs, A. M.; Gaigeot, M. P. Mapping Gas Phase Dipeptide Motions in the Far-Infrared and Terahertz Domain. *Phys. Chem. Chem. Phys.* **2017**, *19*, 13778−13787.
(14) Mahe, J.; Jaeqx, S.; Rijs, A. M.; Gaigeot, M. P. Can Far-IR Action Spectroscopy Combined with BOMD Simulations be Conformation Selective? *Phys. Chem. Chem. Phys.* **2015**, *17*, 25905−25914.
(15) Rijs, A. M.; Ohanessian, G.; Oomens, J.; Meijer, G.; von Helden, G.; Compagnon, I. Internal Proton Transfer Leading to Stable Zwitterionic Structures in a Neutral Isolated Peptide. *Angew. Chem., Int. Ed.* **2010**, *49*, 2332−2335.
(16) Stamm, A.; Maue, D.; Schaly, A.; Schlicher, S.; Bartl, J.; Kubik, S.; Gerhards, M. Structural Analyses of Isolated Cyclic Tetrapeptides with Varying Amino Acid Residues. *Phys. Chem. Chem. Phys.* **2017**, *19*, 10718−10726.
(17) Boldissar, S.; de Vries, M. S. How Nature Covers its Bases. *Phys. Chem. Chem. Phys.* **2018**, *20*, 9701−9716.
(18) de Vries, M. S.; Hobza, P. Gas-Phase Spectroscopy of Biomolecular Building Blocks. *Annu. Rev. Phys. Chem.* **2007**, *58*, 585−612.
(19) Nir, E.; Janzen, C.; Imhof, P.; Kleinermanns, K.; de Vries, M. S. Guanine Tautomerism Revealed by UV-UV and IR-UV Hole Burning Spectroscopy. *J. Chem. Phys.* **2001**, *115*, 4604−4611.
(20) Nir, E.; Kleinermanns, K.; de Vries, M. S. Pairing of Isolated Nucleic-Acid Bases in the Absence of the DNA Backbone. *Nature* **2000**, *408*, 949−951.
(21) Plutzer, C.; Kleinermanns, K. Tautomers and Electronic States of Jet-Cooled Adenine Investigated by Double Resonance Spectroscopy. *Phys. Chem. Chem. Phys.* **2002**, *4*, 4877−4882.
(22) van Zundert, G. C. P.; Jaeqx, S.; Berden, G.; Bakker, J. M.; Kleinermanns, K.; Oomens, J.; Rijs, A. M. IR Spectroscopy of Isolated Neutral and Protonated Adenine and 9-Methyladenine. *ChemPhysChem* **2011**, *12*, 1921−1927.
(23) Barnes, L.; Schindler, B.; Allouche, A. R.; Simon, D.; Chambert, S.; Oomens, J.; Compagnon, I. Anharmonic Simulations of the Vibrational Spectrum of Sulfated Compounds: Application to the Glycosaminoglycan Fragment Glucosamine 6-Sulfate. *Phys. Chem. Chem. Phys.* **2015**, *17*, 25705−25713.
(24) Ben Faleh, A.; Warnke, S.; Rizzo, T. R. Combining Ultrahigh-Resolution Ion-Mobility Spectrometry with Cryogenic Infrared

https://dx.doi.org/10.1021/acs.chemrev.9b00547
Chem. Rev. 2020, 120, 3233−3260

Spectroscopy for the Analysis of Glycan Mixtures. *Anal. Chem.* **2019**, *91*, 4876−4882.
(25) Elferink, H.; Mensink, R. A.; Castelijns, W. W. A.; Jansen, O.; Bruekers, J. P. J.; Martens, J.; Oomens, J.; Rijs, A. M.; Boltje, T. J. The Glycosylation Mechanisms of 6,3-Uronic Acid Lactones. *Angew. Chem., Int. Ed.* **2019**, *58*, 8746−8751.
(26) Elferink, H.; Severijnen, M. E.; Martens, J.; Mensink, R. A.; Berden, G.; Oomens, J.; Rutjes, F.; Rijs, A. M.; Boltje, T. J. Direct Experimental Characterization of Glycosyl Cations by Infrared Ion Spectroscopy. *J. Am. Chem. Soc.* **2018**, *140*, 6034−6038.
(27) Manz, C.; Pagel, K. Glycan Analysis by Ion Mobility-Mass Spectrometry and Gas-Phase Spectroscopy. *Curr. Opin. Chem. Biol.* **2018**, *42*, 16−24.
(28) Masellis, C.; Khanal, N.; Kamrath, M. Z.; Clemmer, D. E.; Rizzo, T. R. Cryogenic Vibrational Spectroscopy Provides Unique Fingerprints for Glycan Identification. *J. Am. Soc. Mass Spectrom.* **2017**, *28*, 2217−2222.
(29) Mucha, E.; Lettow, M.; Marianski, M.; Thomas, D. A.; Struwe, W. B.; Harvey, D. J.; Meijer, G.; Seeberger, P. H.; von Helden, G.; Pagel, K. Fucose Migration in Intact Protonated Glycan Ions: A Universal Phenomenon in Mass Spectrometry. *Angew. Chem., Int. Ed.* **2018**, *57*, 7440−7443.
(30) Mucha, E.; Stuckmann, A.; Marianski, M.; Struwe, W. B.; Meijer, G.; Pagel, K. In-Depth Structural Analysis of Glycans in the Gas Phase. *Chem. Sci.* **2019**, *10*, 1272−1284.
(31) Rijs, A. M.; Sandig, N.; Blom, M. N.; Oomens, J.; Hannam, J. S.; Leigh, D. A.; Zerbetto, F.; Buma, W. J. Controlled Hydrogen-Bond Breaking in a Rotaxane by Discrete Solvation. *Angew. Chem., Int. Ed.* **2010**, *49*, 3896−3900.
(32) Rijs, A. M.; Crews, B. O.; de Vries, M. S.; Hannam, J. S.; Leigh, D. A.; Fanti, M.; Zerbetto, F.; Buma, W. J. Shaping of a Conformationally Flexible Molecular Structure for Spectroscopy. *Angew. Chem., Int. Ed.* **2008**, *47*, 3174−3179.
(33) Rijs, A. M.; Compagnon, I.; Oomens, J.; Hannam, J. S.; Leigh, D. A.; Buma, W. J. Stiff, and Sticky in the Right Places: Binding Interactions in Isolated Mechanically Interlocked Molecules Probed by Mid-Infrared Spectroscopy. *J. Am. Chem. Soc.* **2009**, *131*, 2428−2429.
(34) Rijs, A. M.; Kay, E. R.; Leigh, D. A.; Buma, W. J. IR Spectroscopy on Jet-Cooled Isolated Two-Station Rotaxanes. *J. Phys. Chem. A* **2011**, *115*, 9669−9675.
(35) Fielicke, A.; Kirilyuk, A.; Ratsch, C.; Behler, J.; Scheffler, M.; von Helden, G.; Meijer, G. Structure Determination of Isolated Metal Clusters via Far-Infrared Spectroscopy. *Phys. Rev. Lett.* **2004**, *93*, 4.
(36) Gruene, P.; Rayner, D. M.; Redlich, B.; van der Meer, A. F. G.; Lyon, J. T.; Meijer, G.; Fielicke, A. Structures of Neutral Au_7, Au_{19}, and Au_{20} Clusters in the Gas Phase. *Science* **2008**, *321*, 674−676.
(37) Lang, S. M.; Bernhardt, T. M.; Kiawi, D. M.; Bakker, J. M.; Barnett, R. N.; Landman, U. The Interaction of Water with Free $Mn_4O_4^+$ Clusters: Deprotonation and Adsorption-Induced Structural Transformations. *Angew. Chem., Int. Ed.* **2015**, *54*, 15113−15117.
(38) Lushchikova, O. V.; Huitema, D. M. M.; Lopez-Tarifa, P.; Visscher, L.; Jamshidi, Z.; Bakker, J. M. Structures of Cu_n^+ (n = 3−10) Clusters Obtained by Infrared Action Spectroscopy. *J. Phys. Chem. Lett.* **2019**, *10*, 2151−2155.
(39) Asmis, K. R.; Pivonka, N. L.; Santambrogio, G.; Brummer, M.; Kaposta, C.; Neumark, D. M.; Woste, L. Gas-Phase Infrared Spectrum of the Protonated Water Dimer. *Science* **2003**, *299*, 1375−1377.
(40) Bakker, D. J.; Dey, A.; Tabor, D. P.; Ong, Q.; Mahe, J.; Gaigeot, M. P.; Sibert, E. L.; Rijs, A. M. Fingerprints of Inter- and Intramolecular Hydrogen Bonding in Saligenin-Water Clusters Revealed by Mid- and Far-Infrared Spectroscopy. *Phys. Chem. Chem. Phys.* **2017**, *19*, 20343−20356.
(41) Bernhard, D.; Dietrich, F.; Fatima, M.; Perez, C.; Poblotzki, A.; Jansen, G.; Suhm, M. A.; Schnell, M.; Gerhards, M. Multi-Spectroscopic and Theoretical Analyses on the Diphenyl Ether-tert-butyl Alcohol Complex in the Electronic Ground and Electronically Excited State. *Phys. Chem. Chem. Phys.* **2017**, *19*, 18076−18088.
(42) Bernhard, D.; Holzer, C.; Dietrich, F.; Stamm, A.; Klopper, W.; Gerhards, M. The Structure of Diphenyl Ether-Methanol in the Electronically Excited and Ionic Ground States: A Combined IR/UV Spectroscopic and Theoretical Study. *ChemPhysChem* **2017**, *18*, 3634−3641.
(43) Esser, T. K.; Knorke, H.; Siro-Brigiano, F.; Galimberti, D. R.; Asmis, K. R.; Gaigeot, M. P.; Lisy, J. M. Influence of Argon and D_2 Tagging on the Hydrogen Bond Network in $Cs^+(H2O)_3$; Kinetic Trapping Below 40 K. *Phys. Chem. Chem. Phys.* **2018**, *20*, 28476−28486.
(44) Fagiani, M. R.; Song, X.; Debnath, S.; Gewinner, S.; Schollkopf, W.; Asmis, K. R.; Bischoff, F. A.; Muller, F.; Sauer, J. Dissociative Water Adsorption by $Al_3O_4^+$ in the Gas Phase. *J. Phys. Chem. Lett.* **2017**, *8*, 1272−1277.
(45) Goebbert, D. J.; Garand, E.; Wende, T.; Bergmann, R.; Meijer, G.; Asmis, K. R.; Neumark, D. M. Infrared Spectroscopy of the Microhydrated Nitrate Ions $NO_3^-(H_2O)_{1-6}$. *J. Phys. Chem. A* **2009**, *113*, 7584−7592.
(46) Garand, E. Spectroscopy of Reactive Complexes and Solvated Clusters: A Bottom-Up Approach Using Cryogenic Ion Traps. *J. Phys. Chem. A* **2018**, *122*, 6479−6490.
(47) Voss, J. M.; Fischer, K. C.; Garand, E. Accessing the Vibrational Signatures of Amino Acid Ions Embedded in Water Clusters. *J. Phys. Chem. Lett.* **2018**, *9*, 2246−2250.
(48) Headrick, J. M.; Diken, E. G.; Walters, R. S.; Hammer, N. I.; Christie, R. A.; Cui, J.; Myshakin, E. M.; Duncan, M. A.; Johnson, M. A.; Jordan, K. D. Spectral Signatures of Hydrated Proton Vibrations in Water Clusters. *Science* **2005**, *308*, 1765−1769.
(49) Shin, J. W.; Hammer, N. I.; Diken, E. G.; Johnson, M. A.; Walters, R. S.; Jaeger, T. D.; Duncan, M. A.; Christie, R. A.; Jordan, K. D. Infrared Signature of Structures Associated with the $H^+(H_2O)_n$ (n = 6 to 27) Clusters. *Science* **2004**, *304*, 1137−1140.
(50) Yang, N.; Duong, C. H.; Kelleher, P. J.; Johnson, M. A. Unmasking Rare, Large-Amplitude Motions in D_2-Tagged $I^-(H_2O)_2$ Isotopomers with Two-Color, Infrared-Infrared Vibrational Predissociation Spectroscopy. *J. Phys. Chem. Lett.* **2018**, *9*, 3744−3750.
(51) Yang, N.; Duong, C. H.; Kelleher, P. J.; McCoy, A. B.; Johnson, M. A. Deconstructing Water's Diffuse OH Stretching Vibrational Spectrum with Cold Clusters. *Science* **2019**, *364*, 275−278.
(52) Mackie, C. J.; Candian, A.; Huang, X. C.; Maltseva, E.; Petrignani, A.; Oomens, J.; Buma, W. J.; Lee, T. J.; Tielens, A. The Anharmonic Quartic Force Field Infrared Spectra of Hydrogenated and Methylated PAHs. *Phys. Chem. Chem. Phys.* **2018**, *20*, 1189−1197.
(53) Maltseva, E.; Mackie, C. J.; Candian, A.; Petrignani, A.; Huang, X. C.; Lee, T. J.; Tielens, A.; Oomens, J.; Buma, W. J. High-resolution IR Absorption Spectroscopy of Polycyclic Aromatic Hydrocarbons in the 3 μm Region: Role of Hydrogenation and Alkylation. *Astron. Astrophys.* **2018**, *610*, A65.
(54) de Haas, A. J.; Oomens, J.; Bouwman, J. Facile Pentagon Formation in the Dissociation of Polyaromatics. *Phys. Chem. Chem. Phys.* **2017**, *19*, 2974−2980.
(55) Gao, J. H.; Berden, G.; Oomens, J. Laboratory Infrared Spectroscopy of Gaseous Negatively Charged Polyaromatic Hydrocarbons. *Astrophys. J.* **2014**, *787*, 170
(56) Maltseva, E.; Petrignani, A.; Candian, A.; Mackie, C. J.; Huang, X. C.; Lee, T. J.; Tielens, A.; Oomens, J.; Buma, W. J. High-Resolution IR Absorption Spectroscopy of Polycyclic Aromatic Hydrocarbons: The Realm of Anharmonicity. *Astrophys. J.* **2015**, *814*, 23
(57) Oomens, J.; Tielens, A.; Sartakov, B. G.; von Helden, G.; Meijer, G. Laboratory Infrared Spectroscopy of Cationic Polycyclic Aromatic Hydrocarbon Molecules. *Astrophys. J.* **2003**, *591*, 968−985.
(58) Baxter, J. B.; Guglietta, G. W. Terahertz Spectroscopy. *Anal. Chem.* **2011**, *83*, 4342−4368.
(59) Hangyo, M.; Tani, M.; Nagashima, T. Terahertz Time-Domain Spectroscopy of Solids: a Review. *Int. J. Infrared Millimeter Waves* **2005**, *26*, 1661−1690.

https://dx.doi.org/10.1021/acs.chemrev.9b00547
Chem. Rev. 2020, 120, 3233−3260

(60) Lloyd-Hughes, J.; Jeon, T.-I. A Review of the Terahertz Conductivity of Bulk and Nano-materials. *J. Infrared, Millimeter, Terahertz Waves* **2012**, *33*, 871−925.
(61) Davies, A. G.; Burnett, A. D.; Fan, W.; Linfield, E. H.; Cunningham, J. E. Terahertz Spectroscopy of Explosives and Drugs. *Mater. Today* **2008**, *11*, 18−26.
(62) Leahy-Hoppa, M. R.; Fitch, M. J.; Osiander, R. Terahertz Spectroscopy Techniques for Explosives Detection. *Anal. Bioanal. Chem.* **2009**, *395*, 247−257.
(63) Kanda, N.; Konishi, K.; Nemoto, N.; Midorikawa, K.; Kuwata-Gonokami, M. Real-time Broadband Terahertz Spectroscopic Imaging by Using a High-sensitivity Terahertz Camera. *Sci. Rep.* **2017**, *7*, 42540.
(64) Yamaguchi, S.; Fukushi, Y.; Kubota, O.; Itsuji, T.; Ouchi, T.; Yamamoto, S. Brain Tumor Imaging of Rat Fresh Tissue using Terahertz Spectroscopy. *Sci. Rep.* **2016**, *6*, 30124.
(65) Yang, X.; Zhao, X.; Yang, K.; Liu, Y.; Liu, Y.; Fu, W.; Luo, Y. Biomedical Applications of Terahertz Spectroscopy and Imaging. *Trends Biotechnol.* **2016**, *34*, 810−824.
(66) Grischkowsky, D.; Keiding, S.; Vanexter, M.; Fattinger, C. Far-Infrared Time-Domain Spectroscopy with Terahertz Beams of Dielectrics and Semiconductors. *J. Opt. Soc. Am. B* **1990**, *7*, 2006−2015.
(67) Nemes, C. T.; Koenigsmann, C.; Schmuttenmaer, C. A. Functioning Photoelectrochemical Devices Studied with Time-Resolved Terahertz Spectroscopy. *J. Phys. Chem. Lett.* **2015**, *6*, 3257−3262.
(68) Xu, Y.; Havenith, M. Perspective: Watching Low-frequency Vibrations of Water in Biomolecular Recognition by THz Spectroscopy. *J. Chem. Phys.* **2015**, *143*, 170901.
(69) Whitmire, S. E.; Wolpert, D.; Markelz, A. G.; Hillebrecht, J. R.; Galan, J.; Birge, R. R. Protein Flexibility and Conformational State: A Comparison of Collective Vibrational Modes of Wild-type and D96N Bacteriorhodopsin. *Biophys. J.* **2003**, *85*, 1269−1277.
(70) Zhang, H.; Siegrist, K.; Plusquellic, D. F.; Gregurick, S. K. Terahertz Spectra and Normal Mode Analysis of the Crystalline VA Class Dipeptide Nanotubes. *J. Am. Chem. Soc.* **2008**, *130*, 17846−17857.
(71) Acbas, G.; Niessen, K. A.; Snell, E. H.; Markelz, A. G. Optical Measurements of Long-range Protein Vibrations. *Nat. Commun.* **2014**, *5*, 3076.
(72) Esser, A.; Belsare, S.; Marx, D.; Head-Gordon, T. Mode Specific THz Spectra of Solvated Amino Acids using the AMOEBA Polarizable Force Field. *Phys. Chem. Chem. Phys.* **2017**, *19*, 5579−5590.
(73) Gupta, P. K.; Esser, A.; Forbert, H.; Marx, D. Toward Theoretical Terahertz Spectroscopy of Glassy Aqueous Solutions: Partially Frozen Solute-Solvent Couplings of Glycine in Water. *Phys. Chem. Chem. Phys.* **2019**, *21*, 4975−4987.
(74) Zhang, C.; Durbin, S. M. Hydration-induced Far-infrared Absorption Increase in Myoglobin. *J. Phys. Chem. B* **2006**, *110*, 23607−23613.
(75) Chen, J.-Y.; Knab, J. R.; Ye, S.; He, Y.; Markelz, A. G. Terahertz Dielectric Assay of Solution Phase Protein Binding. *Appl. Phys. Lett.* **2007**, *90*, 243901.
(76) Ebbinghaus, S.; Meister, K.; Born, B.; DeVries, A. L.; Gruebele, M.; Havenith, M. Antifreeze Glycoprotein Activity Correlates with Long-Range Protein- Water Dynamics. *J. Am. Chem. Soc.* **2010**, *132*, 12210−12211.
(77) Heyden, M.; Havenith, M. Combining THz Spectroscopy and MD Simulations to Study Protein-hydration Coupling. *Methods* **2010**, *52*, 74−83.
(78) Hielscher, R.; Friedrich, T.; Hellwig, P. Far-and Mid-Infrared Spectroscopic Analysis of the Substrate-Induced Structural Dynamics of Respiratory Complex I. *ChemPhysChem* **2011**, *12*, 217−224.
(79) Kim, S. J.; Born, B.; Havenith, M.; Gruebele, M. Real-time Detection of Protein-water Dynamics upon Protein Folding by Terahertz Absorption Spectroscopy. *Angew. Chem., Int. Ed.* **2008**, *47*, 6486−6489.
(80) Alexandrov, B. S.; Gelev, V.; Bishop, A. R.; Usheva, A.; Rasmussen, K. O. DNA Breathing Dynamics in the Presence of a Terahertz Field. *Phys. Lett. A* **2010**, *374*, 1214−1217.
(81) Swanson, E. S. Modeling DNA Response to Terahertz Radiation. *Phys. Rev. E* **2011**, *83*, No. 040901.
(82) van der Tol, J.; Jia, D. W.; Li, Y. J.; Chernyy, V.; Bakker, J. M.; Nguyen, M. T.; Lievens, P.; Janssens, E. Structural Assignment of Small Cationic Silver Clusters by Far-infrared Spectroscopy and DFT Calculations. *Phys. Chem. Chem. Phys.* **2017**, *19*, 19360−19368.
(83) Esser, T. K.; Knorke, H.; Asmis, K. R.; Schollkopf, W.; Yu, Q.; Qu, C.; Bowman, J. M.; Kaledin, M. Deconstructing Prominent Bands in the Terahertz Spectra of $H_7O_3^+$ and $H_9O_4^+$: Intermolecular Modes in Eigen Clusters. *J. Phys. Chem. Lett.* **2018**, *9*, 798−803.
(84) Lemmens, A. K.; Gruet, S.; Steber, A. L.; Antony, J.; Grimme, S.; Schnell, M.; Rijs, A. M. Far-IR and UV Spectral Signatures of Controlled Complexation and Microhydration of the Polycyclic Aromatic Hydrocarbon Acenaphthene. *Phys. Chem. Chem. Phys.* **2019**, *21*, 3414−3422.
(85) Bakker, D. J.; Peters, A.; Yatsyna, V.; Zhaunerchyk, V.; Rijs, A. M. Far-Infrared Signatures of Hydrogen Bonding in Phenol Derivatives. *J. Phys. Chem. Lett.* **2016**, *7*, 1238−1243.
(86) Jaeqx, S.; Oomens, J.; Cimas, A.; Gaigeot, M. P.; Rijs, A. M. Gas-Phase Peptide Structures Unraveled by Far-IR Spectroscopy: Combining IR-UV Ion-Dip Experiments with Born-Oppenheimer Molecular Dynamics Simulations. *Angew. Chem., Int. Ed.* **2014**, *53*, 3663−3666.
(87) Galimberti, D. R.; Bougueroua, S.; Mahe, J.; Tommasini, M.; Rijs, A. M.; Gaigeot, M. P. Conformational Assignment of Gas Phase Peptides and their H-bonded Complexes using far-IR/THz: IR-UV Ion Dip Experiment, DFT-MD Spectroscopy, and Graph Theory for Mode Assignment. *Faraday Discuss.* **2019**, *217*, 67−97.
(88) Rijs, A. M.; Oomens, J. IR Spectroscopic Techniques to Study Isolated Biomolecules. *Top. Curr. Chem.* **2014**, *364*, 1−42.
(89) Prazeres, R.; Glotin, F.; Insa, C.; Jaroszynski, D. A.; Ortega, J. M. Two-colour Operation of a Free-Electron Laser and Applications in the Mid-infrared. *Eur. Phys. J. D* **1998**, *3*, 87−93.
(90) Oepts, D.; Vandermeer, A. F. G.; Vanamersfoort, P. W. The Free-Electron-Laser User Facility Felix. *Infrared Phys. Technol.* **1995**, *36*, 297−308.
(91) Schöllkopf, W.; Gewinner, S.; Junkes, H.; Paarmann, A.; Helden, G. v.; Bluem, H. P.; Todd, A. M. M. *The new IR and THz FEL facility at the Fritz Haber Institute in Berlin*; SPIE, 2015.
(92) Didriche, K.; Lauzin, C.; Foldes, T.; Vaernewijck, X. D. D.; Herman, M. The FANTASIO + Set-Up to Investigate Jet-Cooled Molecules: Focus on Overtone Bands of the Acetylene Dimer. *Mol. Phys.* **2010**, *108*, 2155−2163.
(93) Amyay, B.; Herman, M.; Fayt, A.; Fusina, L.; Predoi-Cross, A. High Resolution FTIR Investigation of $^{12}(C_2H_2)$ in the FIR Spectral Range using Synchrotron Radiation. *Chem. Phys. Lett.* **2010**, *491*, 17−19.
(94) Herman, M.; Didriche, K.; Hurtmans, D.; Kizil, B.; Macko, P.; Rizopoulos, A.; Van Poucke, P. FANTASIO: A Versatile Experimental Set-up To Investigate Jet-Cooled Molecules. *Mol. Phys.* **2007**, *105*, 815−823.
(95) Georges, R.; Bonnamy, A.; Benidar, A.; Decroi, M.; Boissoles, J. FTIR Free-Jet Set-up for the High Resolution Spectroscopic Investigation of Condensable Species. *Mol. Phys.* **2002**, *100*, 1551−1558.
(96) Kollipost, F.; Andersen, J.; Mahler, D. W.; Heimdal, J.; Heger, M.; Suhm, M. A.; Larsen, R. W. The Effect of Hydrogen Bonding on Torsional Dynamics: A Combined Far-Infrared Jet and Matrix Isolation Study of Methanol Dimer. *J. Chem. Phys.* **2014**, *141*, 174314.
(97) Quack, M. Spectra and Dynamics of Coupled Vibrations in Polyatomic-Molecules. *Annu. Rev. Phys. Chem.* **1990**, *41*, 839−874.
(98) Albrecht, M.; Rice, C. A.; Suhm, M. A. Elementary Peptide Motifs in the Gas Phase: FTIR Aggregation Study of Formamide, Acetamide, N-Methylformamide, and N-Methylacetamide. *J. Phys. Chem. A* **2008**, *112*, 7530−7542.

https://dx.doi.org/10.1021/acs.chemrev.9b00547
Chem. Rev. 2020, 120, 3233−3260

(99) Lee, J. J.; Albrecht, M.; Rice, C. A.; Suhm, M. A.; Stamm, A.; Zimmer, M.; Gerhards, M. Adaptive Aggregation of Peptide Model Systems. *J. Phys. Chem. A* **2013**, *117*, 7050−7063.
(100) Blake, G. A.; Laughlin, K. B.; Cohen, R. C.; Busarow, K. L.; Gwo, D. H.; Schmuttenmaer, C. A.; Steyert, D. W.; Saykally, R. J. The Berkeley Tunable Far Infrared-Laser Spectrometers. *Rev. Sci. Instrum.* **1991**, *62*, 1701−1716.
(101) Blake, G. A.; Laughlin, K. B.; Cohen, R. C.; Busarow, K. L.; Gwo, D. H.; Schmuttenmaer, C. A.; Steyert, D. W.; Saykally, R. J. Tunable Far Infrared-Laser Spectrometers. *Rev. Sci. Instrum.* **1991**, *62*, 1693−1700.
(102) Cole, W. T. S.; Yonder, O.; Sheikh, A. A.; Fellers, R. S.; Viant, M. R.; Saykally, R. J.; Farrell, J. D.; Wales, D. J. Terahertz VRT Spectroscopy of the Water Hexamer-h12 Cage: Dramatic Libration-Induced Enhancement of Hydrogen Bond Tunneling Dynamics. *J. Phys. Chem. A* **2018**, *122*, 7421−7426.
(103) Lin, W.; Steyert, D. W.; Hlavacek, N. C.; Mukhopadhyay, A.; Page, R. H.; Siegel, P. H.; Saykally, R. J. Terahertz Vibration-Rotation-Tunneling Spectroscopy of the Propane-Water Dimer: The Ortho-state of a 20 cm^{-1} Torsion. *Chem. Phys. Lett.* **2014**, *612*, 167−171.
(104) Cole, W. T. S.; Hlavacek, N. C.; Lee, A. W. M.; Kao, T. Y.; Hu, Q.; Reno, J. L.; Saykally, R. J. Terahertz VRT Spectrometer Employing Quantum Cascade Lasers. *Chem. Phys. Lett.* **2015**, *638*, 144−148.
(105) Cole, W. T. S.; Fellers, R. S.; Viant, M. R.; Leforestier, C.; Saykally, R. J. Far-Infrared VRT Spectroscopy of the Water Dimer: Characterization of the 20 μm Out-of-Plane Librational Vibration. *J. Chem. Phys.* **2015**, *143*, 154306.
(106) Brown, G. G.; Dian, B. C.; Douglass, K. O.; Geyer, S. M.; Shipman, S. T.; Pate, B. H. A Broadband Fourier Transform Microwave Spectrometer based on Chirped Pulse Excitation. *Rev. Sci. Instrum.* **2008**, *79*, No. 053103.
(107) Patterson, D.; Schnell, M.; Doyle, J. M. Enantiomer-Specific Detection of Chiral Molecules via Microwave Spectroscopy. *Nature* **2013**, *497*, 475−477.
(108) Mouhib, H.; Stahl, W.; Luthy, M.; Buchel, M.; Kraft, P. Cassis Odor through Microwave Eyes: Olfactory Properties and Gas-Phase Structures of all the Cassyrane Stereoisomers and its Dihydro Derivatives. *Angew. Chem., Int. Ed.* **2011**, *50*, 5576−5580.
(109) Puzzarini, C.; Biczysko, M.; Barone, V.; Pena, I.; Cabezas, C.; Alonso, J. L. Accurate Molecular Structure and Spectroscopic Properties of Nucleobases: a Combined Computational-Microwave Investigation of 2-Thiouracil as a Case Study. *Phys. Chem. Chem. Phys.* **2013**, *15*, 16965−16975.
(110) Lesarri, A.; Mata, S.; Cocinero, E. J.; Blanco, S.; Lopez, J. C.; Alonso, J. L. The Structure of Neutral Proline. *Angew. Chem., Int. Ed.* **2002**, *41*, 4673−4676.
(111) Melandri, S.; Caminati, W.; Favero, L. B.; Millemaggi, A.; Favero, P. G. A Microwave Free Jet Absorption Spectrometer and Its First Applications. *J. Mol. Struct.* **1995**, *352*, 253−258.
(112) Leon, I.; Alonso, E. R.; Mata, S.; Cabezas, C.; Alonso, J. L. Unveiling the Neutral Forms of Glutamine. *Angew. Chem., Int. Ed.* **2019**, *58*, 16002−16007.
(113) Vaquero-Vara, V.; Alstadt, V.; Sewatsky, T. P.; Claughton, J. L.; Finneran, I. A.; Shipman, S. T.; Pate, B. H.; Pratt, D. W. N-Ethylformamide Dimer. A Beta-Turn Model Peptide in the Gas Phase. *J. Mol. Spectrosc.* **2017**, *335*, 102−107.
(114) Balabin, R. M. Enthalpy Difference between Conformations of Normal Alkanes: Raman Spectroscopy Study of n-Pentane and n-Butane. *J. Phys. Chem. A* **2009**, *113*, 1012−1019.
(115) Balabin, R. M. Conformational Equilibrium in Glycine: Experimental Jet-Cooled Raman Spectrum. *J. Phys. Chem. Lett.* **2010**, *1*, 20−23.
(116) Balabin, R. M. The Identification of the Two Missing Conformers of Gas-Phase Alanine: A Jet-Cooled Raman Spectroscopy Study. *Phys. Chem. Chem. Phys.* **2010**, *12*, 5980−5982.
(117) Shachar, A.; Mayorkas, N.; Bar, I. Structural Features of Monohydrated 2-(4-Fluorophenyl) Ethylamine: A Combined Spectroscopic and Computational Study. *Phys. Chem. Chem. Phys.* **2017**, *19*, 23999−24008.
(118) Mayorkas, N.; Izbitski, S.; Bernat, A.; Bar, I. Simultaneous Ionization-Detected Stimulated Raman and Visible–Visible–Ultraviolet Hole-Burning Spectra of Two Tryptamine Conformers. *J. Phys. Chem. Lett.* **2012**, *3*, 603−607.
(119) Golan, A.; Mayorkas, N.; Rosenwaks, S.; Bar, I. Raman Spectral Signatures as Conformational Probes of Gas Phase Flexible Molecules. *J. Chem. Phys.* **2009**, *131*, No. 024305.
(120) Schmitt, M.; Spiering, F.; Zhaunerchyk, V.; Jongma, R. T.; Jaeqx, S.; Rijs, A. M.; van der Zande, W. J. Far-Infrared Spectra of the Tryptamine A Conformer by IR-UV Ion Gain Spectroscopy. *Phys. Chem. Chem. Phys.* **2016**, *18*, 32116−32124.
(121) Schmitt, M.; Feng, K.; Boehm, M.; Kleinermanns, K. Low Frequency Backbone Vibrations of Individual Conformational Isomers: Tryptamine. *J. Chem. Phys.* **2006**, *125*, 144303.
(122) Schmitt, M.; Henrichs, U.; Muller, H.; Kleinermanns, K. Intermolecular Vibrations of the Phenol Dimer Revealed by Spectral Hole-Burning and Dispersed Fluorescence Spectroscopy. *J. Chem. Phys.* **1995**, *103*, 9918−9928.
(123) Boning, M.; Stuhlmann, B.; Engler, G.; Kleinermanns, K. Isomer-Selective Vibrational Spectroscopy of Jet-Cooled Phenol-Acetylene Aggregates. *J. Phys. Chem. A* **2013**, *117*, 3214−3220.
(124) Kim, N. J.; Kang, H.; Park, Y. D.; Kim, S. K. Dispersed Fluorescence Spectroscopy of Jet-Cooled Adenine. *Phys. Chem. Chem. Phys.* **2004**, *6*, 2802−2805.
(125) Kittrell, C.; Abramson, E.; Kinsey, J. L.; Mcdonald, S. A.; Reisner, D. E.; Field, R. W.; Katayama, D. H. Selective Vibrational-Excitation by Stimulated-Emission Pumping. *J. Chem. Phys.* **1981**, *75*, 2056−2059.
(126) Cooper, D. E.; Klimcak, C. M.; Wessel, J. E. Ion Dip Spectroscopy - a New Technique of Multi-Photon Ionization Spectroscopy Applied to I_2. *Phys. Rev. Lett.* **1981**, *46*, 324−328.
(127) Suzuki, T.; Mikami, N.; Ito, M. 2-Color Stimulated-Emission Spectroscopy of Trans-Stilbene - Large-Amplitude Torsional Motion in the Ground-State and Its Role in Intramolecular Vibrational Redistribution. *J. Phys. Chem.* **1986**, *90*, 6431−6440.
(128) Ebata, T.; Ito, M. Ground-State IVR of Jet-Cooled P-Alkylphenols and P-Alkylanilines Studied by Stimulated-Emission Ion Dip and Stimulated Raman-UV Optical Double-Resonance Spectroscopies. *J. Phys. Chem.* **1992**, *96*, 3224−3231.
(129) Bakker, D. J.; Ong, Q.; Dey, A.; Mahe, J.; Gaigeot, M. P.; Rijs, A. M. Anharmonic, Dynamic and Functional Level Effects in Far-infrared Spectroscopy: Phenol Derivatives. *J. Mol. Spectrosc.* **2017**, *342*, 4−16.
(130) Bakker, D. J. Ph.D. Dissertation, Radboud University, 2017, https://repository.ubn.ru.nl/bitstream/handle/2066/177068/177068.pdf?sequence=1, (accessed January 28, 2020).
(131) Nagornova, N. S.; Rizzo, T. R.; Boyarkin, O. V. Exploring the Mechanism of IR-UV Double-Resonance for Quantitative Spectroscopy of Protonated Polypeptides and Proteins. *Angew. Chem., Int. Ed.* **2013**, *52*, 6002−6005.
(132) Bakels, S.; Meijer, E. M.; Greuell, M.; Porskamp, S. B. A.; Rouwhorst, G.; Mahe, J.; Gaigeot, M. P.; Rijs, A. M. Interactions of Aggregating Peptides Probed by IR-UV Action Spectroscopy. *Faraday Discuss.* **2019**, *217*, 322−342.
(133) Frauenfelder, H.; Sligar, S. G.; Wolynes, P. G. The Energy Landscapes and Motions of Proteins. *Science* **1991**, *254*, 1598−1603.
(134) Callender, R. H.; Dyer, R. B.; Gilmanshin, R.; Woodruff, W. H. Fast Events in Protein Folding: The Time Evolution of Primary Processes. *Annu. Rev. Phys. Chem.* **1998**, *49*, 173−202.
(135) Takahashi, S.; Yeh, S.-R.; Das, T. K.; Chan, C.-K.; Gottfried, D. S.; Rousseau, D. L. Folding of Cytochrome C Initiated by Submillisecond Mixing. *Nat. Struct. Mol. Biol.* **1997**, *4*, 44.
(136) Turton, D. A.; Senn, H. M.; Harwood, T.; Lapthorn, A. J.; Ellis, E. M.; Wynne, K. Terahertz Underdamped Vibrational Motion Governs Protein-Ligand Binding in Solution. *Nat. Commun.* **2014**, *5*, 3999.

https://dx.doi.org/10.1021/acs.chemrev.9b00547
Chem. Rev. 2020, 120, 3233−3260

(137) Bakker, J. M.; Aleese, L. M.; Meijer, G.; von Helden, G. Fingerprint IR Spectroscopy to Probe Amino Acid Conformations in the Gas Phase. *Phys. Rev. Lett.* **2003**, *91*, 203003.
(138) Çarçabal, P.; Kroemer, R. T.; Snoek, L. C.; Simons, J. P.; Bakker, J. M.; Compagnon, I.; Meijer, G.; von Helden, G. Hydrated Complexes of Tryptophan: Ion Dip Infrared Spectroscopy in the 'Molecular Fingerprint' Region, 100−2000 cm^{-1}. *Phys. Chem. Chem. Phys.* **2004**, *6*, 4546−4552.
(139) Biswal, H. S.; Loquais, Y.; Tardivel, B.; Gloaguen, E.; Mons, M. Isolated Monohydrates of a Model Peptide Chain: Effect of a First Water Molecule on the Secondary Structure of a Capped Phenylalanine. *J. Am. Chem. Soc.* **2011**, *133*, 3931−3942.
(140) Fischer, J. L.; Elvir, B. R.; Delucia, S.-A.; Blodgett, K. N.; Zeller, M.; Kubasik, M. A.; Zwier, T. S. Single-Conformation Spectroscopy of Capped Aminoisobutryic Acid Dipeptides: The Effect of C-Terminal Cap Chromophore on Conformation. *J. Phys. Chem. A* **2019**, *123*, 4178−4187.
(141) Pribble, R. N.; Zwier, T. S. Size-Specific Infrared-Spectra of Benzene-$(H_2O)_n$ Clusters (n = 1 through 7) - Evidence for Noncyclic $(H_2O)_n$ Structures. *Science* **1994**, *265*, 75−79.
(142) Chin, W.; Piuzzi, F.; Dimicoli, I.; Mons, M. Probing the Competition Between Secondary Structures and Local Preferences in Gas Phase Isolated Peptide Backbones. *Phys. Chem. Chem. Phys.* **2006**, *8*, 1033−1048.
(143) Gerhards, M.; Unterberg, C. Structures of the Protected Amino Acid Ac-Phe-OMe and its Dimer: A Beta-sheet Model System in the Gas Phase. *Phys. Chem. Chem. Phys.* **2002**, *4*, 1760−1765.
(144) Stamm, A.; Maue, D.; Gerhards, M. Structural Rearrangement by Isomer-Specific Infrared Excitation in the Neutral Isolated Dihydrated Cluster of 3-Hydroxyflavone. *J. Phys. Chem. Lett.* **2018**, *9*, 4360−4366.
(145) Robertson, E. G.; Simons, J. P. Getting into Shape: Conformational and Supramolecular Landscapes in Small Biomolecules and their Hydrated Clusters. *Phys. Chem. Chem. Phys.* **2001**, *3*, 1−18.
(146) Snoek, L. C.; Robertson, E. G.; Kroemer, R. T.; Simons, J. P. Conformational Landscapes in Amino Acids: Infrared and Ultraviolet Ion-dip Spectroscopy of Phenylalanine in the Gas Phase. *Chem. Phys. Lett.* **2000**, *321*, 49−56.
(147) Uhlemann, T.; Seidel, S.; Muller, C. W. Laser Desorption Single-conformation UV and IR Spectroscopy of the Sulfonamide Drug Sulfanilamide, the Sulfanilamide-Water Complex, and the Sulfanilamide Dimer. *Phys. Chem. Chem. Phys.* **2017**, *19*, 14625−14640.
(148) Mitsuda, H.; Miyazaki, M.; Nielsen, I. B.; Çarçabal, P.; Dedonder, C.; Jouvet, C.; Ishiuchi, S.; Fujii, M. Evidence for Catechol Ring- Induced Conformational Restriction in Neurotransmitters. *J. Phys. Chem. Lett.* **2010**, *1*, 1130−1133.
(149) Usabiaga, I.; Camiruaga, A.; Insausti, A.; Carcabal, P.; Cocinero, E. J.; Leon, I.; Fernandez, J. A. Phenyl-β-D-glucopyranoside and Phenyl-β-D-galactopyranoside Dimers: Small Structural Differences but Very Different Interactions. *Front. Phys.* **2018**, *6*, DOI: 10.3389/fphy.2018.00003
(150) Boesl, U.; Neusser, H. J.; Schlag, E. W. 2-Photon Ionization of Polyatomic-Molecules in a Mass-Spectrometer. *Z. Naturforsch., A: Phys. Sci.* **1978**, *33*, 1546−1548.
(151) Zandee, L.; Bernstein, R. B. Resonance-Enhanced Multi-Photon Ionization and Fragmentation of Molecular-Beams - NO, I_2, Benzene, and Butadiene. *J. Chem. Phys.* **1979**, *71*, 1359−1371.
(152) Page, R. H.; Shen, Y. R.; Lee, Y. T. Infrared-Ultraviolet Double-Resonance Studies of Benzene Molecules in a Supersonic Beam. *J. Chem. Phys.* **1988**, *88*, 5362−5376.
(153) Unterberg, C.; Jansen, A.; Gerhards, M. Ultraviolet/Infrared-Double Resonance Spectroscopy and Ab Initio Calculations on the $Indole^+$ and $Indole(H_2O)_1^+$ Cations. *J. Chem. Phys.* **2000**, *113*, 7945−7954.
(154) Meijer, G.; Devries, M. S.; Hunziker, H. E.; Wendt, H. R. Laser Desorption Jet-Cooling of Organic-Molecules - Cooling Characteristics and Detection Sensitivity. *Appl. Phys. B: Lasers Opt.* **1990**, *51*, 395−403.
(155) Rijs, A. M.; Kabelac, M.; Abo-Riziq, A.; Hobza, P.; de Vries, M. S. Isolated Gramicidin Peptides Probed by IR Spectroscopy. *ChemPhysChem* **2011**, *12*, 1816−1821.
(156) Ishiuchi, S.; Yamada, K.; Oba, H.; Wako, H.; Fujii, M. Gas Phase Ultraviolet and Infrared Spectroscopy on a Partial Peptide of β_2-Adrenoceptor SIVSF-NH_2 by a Laser Desorption Supersonic Jet Technique. *Phys. Chem. Chem. Phys.* **2016**, *18*, 23277−23284.
(157) Cocinero, E. J.; Çarçabal, P.; Vaden, T. D.; Simons, J. P.; Davis, B. G. Sensing the Anomeric Effect in a Solvent-free Environment. *Nature* **2011**, *469*, 76.
(158) Hunig, I.; Seefeld, K. A.; Kleinermanns, K. REMPI and UV-UV Double Resonance Spectroscopy of Tryptophan Ethylester and the Dipeptides Tryptophan-Serine, Glycine-Tryptophan and Proline-Tryptophan. *Chem. Phys. Lett.* **2003**, *369*, 173−179.
(159) Teschmit, N.; Dlugolecki, K.; Gusa, D.; Rubinsky, I.; Horke, D. A.; Kupper, J. Characterizing and Optimizing a Laser-Desorption Molecular Beam Source. *J. Chem. Phys.* **2017**, *147*, 144204.
(160) Piuzzi, F.; Dimicoli, I.; Mons, M.; Tardivel, B.; Zhao, Q. C. A Simple Laser Vaporization Source for Thermally Fragile Molecules Coupled to a Supersonic Expansion: Application to the Spectroscopy of Tryptophan. *Chem. Phys. Lett.* **2000**, *320*, 282−288.
(161) Ghafur, O.; Crane, S. W.; Ryszka, M.; Bockova, J.; Rebelo, A.; Saalbach, L.; De Camillis, S.; Greenwood, J. B.; Eden, S.; Townsend, D. Ultraviolet Relaxation Dynamics in Uracil: Time-resolved Photoion Yield Studies using a Laser-based Thermal Desorption Source. *J. Chem. Phys.* **2018**, *149*, No. 034301.
(162) Usmanov, D. T.; Ninomiya, S.; Chen, L. C.; Saha, S.; Mandal, M. K.; Sakai, Y.; Takaishi, R.; Habib, A.; Hiraoka, K.; Yoshimura, K.; et al. Desorption in Mass Spectrometry. *Mass Spectrom.* **2017**, *6*, S0059−S0059.
(163) Levy, D. H. Laser Spectroscopy of Cold Gas-Phase Molecules. *Annu. Rev. Phys. Chem.* **1980**, *31*, 197−225.
(164) Lubman, D. M.; Tembreull, R. Pulsed Laser Desorption of Biologicals in Supersonic Jets with Resonant 2-Photon Ionization Detection. *Anal. Chem.* **1987**, *59*, 1082−1088.
(165) Posthumus, M. A.; Kistemaker, P. G.; Meuzelaar, H. L. C.; Tennoeverdebrauw, M. C. Laser Desorption-Mass Spectrometry of Polar Non-Volatile Bio-Organic Molecules. *Anal. Chem.* **1978**, *50*, 985−991.
(166) Usabiaga, I.; Gonzalez, J.; Arnaiz, P. F.; Leon, I.; Cocinero, E. J.; Fernandez, J. A. Modeling the Tyrosine-Sugar Interactions in Supersonic Expansions: Glucopyranose-Phenol Clusters. *Phys. Chem. Chem. Phys.* **2016**, *18*, 12457−12465.
(167) Cable, J. R.; Tubergen, M. J.; Levy, D. H. Laser Desorption Molecular-Beam Spectroscopy - the Electronic-Spectra of Tryptophan Peptides in the Gas-Phase. *J. Am. Chem. Soc.* **1987**, *109*, 6198−6199.
(168) Voumard, P.; Zenobi, R. Laser-Induced Thermal-Desorption of Aniline from Silica Surfaces. *J. Chem. Phys.* **1995**, *103*, 6795−6805.
(169) Zare, R. N.; Levine, R. D. Mechanism for Bond-Selective Processes in Laser Desorption. *Chem. Phys. Lett.* **1987**, *136*, 593−599.
(170) Zenobi, R.; Hahn, J. H.; Zare, R. N. Surface-Temperature Measurement of Dielectric Materials Heated by Pulsed Laser-Radiation. *Chem. Phys. Lett.* **1988**, *150*, 361−365.
(171) Li, Y. Z.; McIver, R. T.; Hemminger, J. C. Experimental-Determination of Thermal and Nonthermal Mechanisms for Laser Desorption from Thin Metal-Films. *J. Chem. Phys.* **1990**, *93*, 4719−4723.
(172) Hall, R. B. Pulsed-Laser-Induced Desorption Studies of the Kinetics of Surface-Reactions. *J. Phys. Chem.* **1987**, *91*, 1007−1015.
(173) Levis, R. J. Laser-Desorption and Ejection of Biomolecules from the Condensed-Phase into the Gas-Phase. *Annu. Rev. Phys. Chem.* **1994**, *45*, 483−518.
(174) Chin, W.; Dognon, J. P.; Canuel, C.; Piuzzi, F.; Dimicoli, I.; Mons, M.; Compagnon, I.; von Helden, G.; Meijer, G. Secondary Structures of Short Peptide Chains in the Gas Phase: Double Resonance Spectroscopy of Protected Dipeptides. *J. Chem. Phys.* **2005**, *122*, No. 054317.

https://dx.doi.org/10.1021/acs.chemrev.9b00547
Chem. Rev. 2020, 120, 3233−3260

(175) Chin, W.; Mons, M.; Dognon, J. P.; Piuzzi, F.; Tardivel, B.; Dimicoli, I. Competition Between Local Conformational Preferences and Secondary Structures in Gas-Phase Model Tripeptides as Revealed by Laser Spectroscopy and Theoretical Chemistry. *Phys. Chem. Chem. Phys.* **2004**, *6*, 2700−2709.
(176) Mons, M.; Dimicoli, I.; Piuzzi, F.; Tardivel, B.; Elhanine, M. Tautomerism of the DNA Base Guanine and its Methylated Derivatives as Studied by Gas-phase Infrared and Ultraviolet Spectroscopy. *J. Phys. Chem. A* **2002**, *106*, 5088−5094.
(177) Gloaguen, E.; Valdes, H.; Pagliarulo, F.; Pollet, R.; Tardivel, B.; Hobza, P.; Piuzzi, F.; Mons, M. Experimental and Theoretical Investigation of the Aromatic−Aromatic Interaction in Isolated Capped Dipeptides. *J. Phys. Chem. A* **2010**, *114*, 2973−2982.
(178) Teschmit, N.; Horke, D. A.; Kupper, J. Spatially Separating the Conformers of a Dipeptide. *Angew. Chem., Int. Ed.* **2018**, *57*, 13775−13779.
(179) Zehnacker, A.; Suhm, M. A. Chirality Recognition between Neutral Molecules in the Gas Phase. *Angew. Chem., Int. Ed.* **2008**, *47*, 6970−6992.
(180) Perez-Mellor, A.; Alata, I.; Lepere, V.; Zehnacker, A. Conformational Study of the Jet-Cooled Diketopiperazine Peptide Cyclo Tyrosyl-Prolyl. *J. Phys. Chem. B* **2019**, *123*, 6023−6033.
(181) Gotch, A. J.; Zwier, T. S. Multiphoton Ionization Studies of Clusters of Immiscible Liquids.I. C_6H_6-$(H_2O)_n$, n = 1,2. *J. Chem. Phys.* **1992**, *96*, 3388−3401.
(182) Even, U. The Even-Lavie Valve as a Source for High Intensity Supersonic Beam. *Epj Technol. Instrum.* **2015**, *2*, DOI: 10.1140/epjti/s40485-015-0027-5
(183) Irimia, D.; Dobrikov, D.; Kortekaas, R.; Voet, H.; van den Ende, D. A.; Groen, W. A.; Janssen, M. H. M. A Short Pulse (7 μs FWHM) and High Repetition Rate (dc-5kHz) Cantilever Piezovalve for Pulsed Atomic and Molecular Beams. *Rev. Sci. Instrum.* **2009**, *80*, 113303.
(184) Stern, O. Zur Methode der Molekularstrahlen. I. *Eur. Phys. J. A* **1926**, *39*, 751−763.
(185) Dunoyer, L. Comptes Rendus Acad. *Sc. Paris* **1911**, *152*, 594.
(186) Kantrowitz, A.; Grey, J. A High Intensity Source for the Molecular Beam 0.1. Theoretical. *Rev. Sci. Instrum.* **1951**, *22*, 328−332.
(187) Smalley, R. E.; Wharton, L.; Levy, D. H. Molecular Optical Spectroscopy with Supersonic Beams and Jets. *Acc. Chem. Res.* **1977**, *10*, 139−145.
(188) Johnston, M. V. Supersonic Jet Expansions in Analytical Spectroscopy. *TrAC, Trends Anal. Chem.* **1984**, *3*, 58−61.
(189) Miller, T. A. Chemistry and Chemical Intermediates in Supersonic Free Jet Expansions. *Science* **1984**, *223*, 545−553.
(190) Gloaguen, E.; de Courcy, B.; Piquemal, J. P.; Pilme, J.; Parisel, O.; Pollet, R.; Biswal, H. S.; Piuzzi, F.; Tardivel, B.; Broquier, M.; et al. Gas-Phase Folding of a Two-Residue Model Peptide Chain: On the Importance of an Interplay between Experiment and Theory. *J. Am. Chem. Soc.* **2010**, *132*, 11860−11863.
(191) Yatsyna, V. Ph.D. Dissertation, University of Gothenburg, 2019, https://gupea.ub.gu.se/bitstream/2077/58138/1/gupea_2077_58138_1.pdf, (accessed January 28, 2020).
(192) Handschuh, M.; Nettesheim, S.; Zenobi, R. Is Infrared Laser-induced Desorption a Thermal Process? The Case of Aniline. *J. Phys. Chem. B* **1999**, *103*, 1719−1726.
(193) Plowright, R. J.; Gloaguen, E.; Mons, M. Compact Folding of Isolated Four-Residue Neutral Peptide Chains: H-Bonding Patterns and Entropy Effects. *ChemPhysChem* **2011**, *12*, 1889−1899.
(194) Yatsyna, V.; Mallat, R.; Gorn, T.; Schmitt, M.; Feifel, R.; Rijs, A. M.; Zhaunerchyk, V. Competition Between Folded and Extended Structures of Alanylalanine (Ala-Ala) in a Molecular Beam. *Phys. Chem. Chem. Phys.* **2019**, *21*, 14126−14132.
(195) Wiley, W. C.; Mclaren, I. H. Time-of-Flight Mass Spectrometer with Improved Resolution. *Rev. Sci. Instrum.* **1955**, *26*, 1150−1157.
(196) Mamyrin, B. A.; Karataev, V. I.; Shmikk, D. V.; Zagulin, V. A. Mass-Reflectron a New Nonmagnetic Time-of-Flight High-Resolution Mass-Spectrometer. *J. Exp. Theor. Phys.* **1973**, *64*, 82−89.
(197) Boesl, U. Time-of-Flight Mass Spectrometry: Introduction to the Basics. *Mass Spectrom. Rev.* **2017**, *36*, 86−109.
(198) The FHI free-electron laser (FEL) facility http://fel.fhi-berlin.mpg.de/ (accessed August 6th, 2019).
(199) FELIX Laboratory https://www.ru.nl/felix/ (accessed August 6th, 2019).
(200) Centre Laser Infrarouge d'Orsay http://old.clio.lcp.u-psud.fr/clio_eng/clio_eng.htm (accessed August 6th, 2019).
(201) Joshi, K.; Semrouni, D.; Ohanessian, G.; Clavaguéra, C. Structures and IR Spectra of the Gramicidin S Peptide: Pushing the Quest for Low-Energy Conformations. *J. Phys. Chem. B* **2012**, *116*, 483−490.
(202) Martens, J. K.; Compagnon, I.; Nicol, E.; McMahon, T. B.; Clavaguéra, C.; Ohanessian, G. Globule to Helix Transition in Sodiated Polyalanines. *J. Phys. Chem. Lett.* **2012**, *3*, 3320−3324.
(203) Stedwell, C. N.; Galindo, J. F.; Roitberg, A. E.; Polfer, N. C. In *Annu. Rev. Anal. Chem.*; Cooks, R. G., Pemberton, J. E., Eds.; 2013; Vol. *6*, pp 267−285.
(204) Cismesia, A. P.; Bell, M. R.; Tesler, L. F.; Alves, M.; Polfer, N. C. Infrared ion Spectroscopy: An Analytical Tool for the Study of Metabolites. *Analyst* **2018**, *143*, 1615−1623.
(205) Stearns, J. A.; Boyarkin, O. V.; Rizzo, T. R. Spectroscopic Signatures of Gas-phase Helices: Ac-Phe-$(Ala)_5$-Lys-H^+ and Ac-Phe-$(Ala)_{10}$-Lys-H^+. *J. Am. Chem. Soc.* **2007**, *129*, 13820−13821.
(206) Rizzo, T. R.; Stearns, J. A.; Boyarkin, O. V. Spectroscopic Studies of Cold, Gas-phase Biomolecular Ions. *Int. Rev. Phys. Chem.* **2009**, *28*, 481−515.
(207) Gaigeot, M.-P.; Spezia, R. Theoretical Methods for Vibrational Spectroscopy and Collision Induced Dissociation in the Gas Phase. *Top. Curr. Chem.* **2014**, *364*, 99−151.
(208) Dunbar, R. C.; Martens, J.; Berden, G.; Oomens, J. Binding of Divalent Metal Ions with Deprotonated Peptides: Do Gas-Phase Anions Parallel the Condensed Phase? *J. Phys. Chem. A* **2018**, *122*, 5589−5596.
(209) van Outersterp, R. E.; Martens, J.; Berden, G.; Steill, J. D.; Oomens, J.; Rijs, A. M. Structural Characterization of Nucleotide 5-Triphosphates by Infrared Ion Spectroscopy and Theoretical Studies. *Phys. Chem. Chem. Phys.* **2018**, *20*, 28319−28330.
(210) Compagnon, I.; Oomens, J.; Bakker, J.; Meijer, G.; von Helden, G. Vibrational Spectroscopy of a Non-Aromatic Amino Acid-based Model Peptide: Identification of the Gamma-turn Motif of the Peptide Backbone. *Phys. Chem. Chem. Phys.* **2005**, *7*, 13−15.
(211) Barnes, L.; Schindler, B.; Chambert, S.; Allouche, A. R.; Compagnon, I. Conformational Preferences of Protonated N-Acetylated Hexosamines Probed by InfraRed Multiple Photon Dissociation (IRMPD) Spectroscopy and Ab Initio Calculations. *Int. J. Mass Spectrom.* **2017**, *421*, 116−123.
(212) Klyne, J.; Miyazaki, M.; Fujii, M.; Dopfer, O. Sequential Microhydration of Cationic 5-Hydroxyindole ($5HI^+$): Infrared Photodissociation Spectra of $5HI^+$-W_n Clusters (W = H_2O, $n \leq 4$). *Phys. Chem. Chem. Phys.* **2018**, *20*, 3092−3108.
(213) Ishiuchi, S.; Sasaki, Y.; Lisy, J. M.; Fujii, M. Ion-Peptide Interactions between Alkali Metal Ions and a Termini-protected Dipeptide: Modeling a Portion of the Selectivity Filter in K^+ Channels. *Phys. Chem. Chem. Phys.* **2019**, *21*, 561−571.
(214) Brites, V.; Nicely, A. L.; Sieffert, N.; Gaigeot, M.-P.; Lisy, J. M. High Energy Conformers of $M^+(APE)(H_2O)_{0-1}Ar_{0-1}$ Clusters Revealed by Combined IR-PD and DFT-MD Anharmonic Vibrational Spectroscopy. *Phys. Chem. Chem. Phys.* **2014**, *16*, 13086−13095.
(215) Rodriguez, J. D.; Lisy, J. M. Probing Ionophore Selectivity in Argon-Tagged Hydrated Alkali Metal Ion-Crown Ether Systems. *J. Am. Chem. Soc.* **2011**, *133*, 11136−11146.
(216) Fischer, K. C.; Voss, J. M.; Zhou, J.; Garand, E. Probing Solvation-Induced Structural Changes in Conformationally Flexible Peptides: IR Spectroscopy of Gly_3H^+-(H_2O). *J. Phys. Chem. A* **2018**, *122*, 8213−8221.

https://dx.doi.org/10.1021/acs.chemrev.9b00547
Chem. Rev. 2020, 120, 3233−3260

(217) Cramer, C. J. *Essentials of Computational Chemistry*; Wiley: New York, 2004.
(218) Compagnon, I.; Oomens, J.; Meijer, G.; von Helden, G. Mid-Infrared Spectroscopy of Protected Peptides in the Gas Phase: A Probe of the Backbone Conformation. *J. Am. Chem. Soc.* **2006**, *128*, 3592−3597.
(219) Voronina, L.; Masson, A.; Kamrath, M.; Schubert, F.; Clemmer, D.; Baldauf, C.; Rizzo, T. Conformations of Prolyl-Peptide Bonds in the Bradykinin 1−5 Fragment in Solution and in the Gas Phase. *J. Am. Chem. Soc.* **2016**, *138*, 9224−9233.
(220) Servage, K. A.; Silveira, J. A.; Fort, K. L.; Russell, D. H. Cryogenic Ion Mobility-Mass Spectrometry: Tracking Ion Structure from Solution to the Gas Phase. *Acc. Chem. Res.* **2016**, *49*, 1421−1428.
(221) Sohn, W. Y.; Kim, M.; Kim, S. S.; Park, Y. D.; Kang, H. Solvent-assisted Conformational Isomerization and the Conformationally-pure REMPI Spectrum of 3-Aminophenol. *Phys. Chem. Chem. Phys.* **2011**, *13*, 7037−7042.
(222) Rodriguez, O.; Lisy, J. M. Revisiting $Li^+(H_2O)_{3-4}Ar_1$ Clusters: Evidence of High-Energy Conformers from Infrared Spectra. *J. Phys. Chem. Lett.* **2011**, *2*, 1444−1448.
(223) Rodriguez, J. D.; Lisy, J. M. Infrared spectroscopy of Gas-phase Hydrated K^+:18-crown-6 Complexes: Evidence for High Energy Conformer Trapping using the Argon Tagging Method. *Int. J. Mass Spectrom.* **2009**, *283*, 135−139.
(224) Brites, V.; Cimas, A.; Spezia, R.; Sieffert, N.; Lisy, J. M.; Gaigeot, M. P. Stalking Higher Energy Conformers on the Potential Energy Surface of Charged Species. *J. Chem. Theory Comput.* **2015**, *11*, 871−883.
(225) Voronina, L.; Rizzo, T. R. Spectroscopic Studies of Kinetically Trapped Conformations in the Gas Phase: The Case of Triply Protonated Bradykinin. *Phys. Chem. Chem. Phys.* **2015**, *17*, 25828−25836.
(226) Fort, K. L.; Silveira, J. A.; Pierson, N. A.; Servage, K. A.; Clemmer, D. E.; Russell, D. H. From Solution to the Gas Phase: Factors That Influence Kinetic Trapping of Substance P in the Gas Phase. *J. Phys. Chem. B* **2014**, *118*, 14336−14344.
(227) *Faraday Discussions, Advances in ion spectroscopy - from astrophysics to biology*; RSC, Royal Society of Chemistry, 2019.
(228) Yu, Q.; Bowman, J. M. Classical, Thermostated Ring Polymer, and Quantum VSCF/VCI Calculations of IR Spectra of $H_7O_3^+$ and $H_9O_4^+$ (Eigen) and Comparison with Experiment. *J. Phys. Chem. A* **2019**, *123*, 1399−1409.
(229) Qu, C.; Bowman, J. M. Quantum Approaches to Vibrational Dynamics and Spectroscopy: Is Ease of Interpretation Sacrificed as Rigor Increases? *Phys. Chem. Chem. Phys.* **2019**, *21*, 3397−3413.
(230) Houston, P. L.; Van Hoozen, B. L.; Qu, C.; Yu, Q.; Bowman, J. M. Teaching Vibrational Spectra to Assign Themselves. *Faraday Discuss.* **2018**, *212*, 65−82.
(231) Hirshberg, B.; Sagiv, L.; Gerber, R. B. Approximate Quantum Dynamics using Ab Initio Classical Separable Potentials: Spectroscopic Applications. *J. Chem. Theory Comput.* **2017**, *13*, 982−991.
(232) Barone, V.; Biczysko, M.; Bloino, J. Fully Anharmonic IR and Raman Spectra of Medium-Size Molecular Systems: Accuracy and Interpretation. *Phys. Chem. Chem. Phys.* **2014**, *16*, 1759−1787.
(233) Sibert, E. L. Modeling Vibrational Anharmonicity in Infrared Spectra of High Frequency Vibrations of Polyatomic Molecules. *J. Chem. Phys.* **2019**, *150*, No. 090901.
(234) McQuarrie, D. A. *Statistical Mechanics*; University Science Books, 2000.
(235) Kubo, R.; Toda, M.; Hashitsume, N. *Statistical Physics II*; Springer: Berlin Heidelberg, 1991.
(236) Gaigeot, M.-P.; Sprik, M. Ab Initio Molecular Dynamics Computation of the Infrared Spectrum of Aqueous Uracil. *J. Phys. Chem. B* **2003**, *107*, 10344−10358.
(237) Ramirez, R.; Lopez-Ciudad, T.; Kumar, P.; Marx, D. Quantum Corrections to Classical Time-correlation Functions: Hydrogen Bonding and Anharmonic Floppy Modes. *J. Chem. Phys.* **2004**, *121*, 3973−3983.
(238) Borysow, J.; Moraldi, M.; Frommhold, L. The Collission-induced Spectroscopies Concerning the Desymmetrization of Classical Line-shape. *Mol. Phys.* **1985**, *56*, 913−913.
(239) Gaigeot, M.-P. Theoretical Spectroscopy of Floppy Peptides at Room Temperature. A DFTMD Perspective: Gas and Aqueous Phase. *Phys. Chem. Chem. Phys.* **2010**, *12*, 3336−3359.
(240) Roy, T. K.; Gerber, R. B. Vibrational Self-consistent Field Calculations for Spectroscopy of Biological Molecules: New Algorithmic Developments and Applications. *Phys. Chem. Chem. Phys.* **2013**, *15*, 9468−9492.
(241) Mardirossian, N.; Lambrecht, D. S.; McCaslin, L.; Xantheas, S. S.; Head-Gordon, M. The Performance of Density Functionals for Sulfate-Water Clusters. *J. Chem. Theory Comput.* **2013**, *9*, 1368−1380.
(242) Lambrecht, D. S.; McCaslin, L.; Xantheas, S. S.; Epifanovsky, E.; Head-Gordon, M. Refined Energetic Ordering for Sulphate-Water (n = 3−6) Clusters using High-Level Electronic Structure Calculations. *Mol. Phys.* **2012**, *110*, 2513−2521.
(243) Paesani, F. Getting the Right Answers for the Right Reasons: Toward Predictive Molecular Simulations of Water with Many-Body Potential Energy Functions. *Acc. Chem. Res.* **2016**, *49*, 1844−1851.
(244) Wang, Y. M.; Huang, X. C.; Shepler, B. C.; Braams, B. J.; Bowman, J. M. Flexible, Ab Initio Potential, and Dipole Moment Surfaces for Water. I. Tests and Applications for Clusters up to the 22-mer. *J. Chem. Phys.* **2011**, *134*, No. 094509.
(245) Baldauf, C.; Rossi, M. Going Clean: Structure and Dynamics of Peptides in the Gas Phase and Paths to Solvation. *J. Phys.: Condens. Matter* **2015**, *27*, 493002.
(246) Becke, A. D. Density-Functional Exchange-Energy Approximation with Correct Asymptotic Behavior. *Phys. Rev. A: At., Mol., Opt. Phys.* **1988**, *38*, 3098−3100.
(247) Lee, C.; Yang, W.; Parr, R. G. Development of the Colle-Salvetti Correlation-Energy Formula into a Functional of the Electron Density. *Phys. Rev. B: Condens. Matter Mater. Phys.* **1988**, *37*, 785−789.
(248) Grimme, S.; Antony, J.; Ehrlich, S.; Krieg, H. A Consistent and Accurate Ab Initio Parametrization of Density Functional Dispersion Correction (DFT-D) for the 94 Elements H-Pu. *J. Chem. Phys.* **2010**, *132*, 154104.
(249) Beck, J. P.; Cimas, A.; Lisy, J. M.; Gaigeot, M. P. O-H Anharmonic Vibrational Motions in Cl^-–$(CH_3OH)_{1-2}$ Ionic Clusters. Combined IRPD Experiments and AIMD Simulations. *Spectrochim. Acta, Part A* **2014**, *119*, 12−17.
(250) Marinica, D. C.; Gregoire, G.; Desfrancois, C.; Schermann, J. P.; Borgis, D.; Gaigeot, M. P. Ab Initio Molecular Dynamics of Protonated Dialanine and Comparison to Infrared Multiphoton Dissociation Experiments. *J. Phys. Chem. A* **2006**, *110*, 8802−8810.
(251) Gaigeot, M. P.; Vuilleumier, R.; Sprik, M.; Borgis, D. Infrared Spectroscopy of N-Methylacetamide Revisited by Ab Initio Molecular Dynamics Simulations. *J. Chem. Theory Comput.* **2005**, *1*, 772−789.
(252) Pezzotti, S.; Galimberti, D. R.; Gaigeot, M. P. 2D H-Bond Network as the Topmost Skin to the Air-Water Interface. *J. Phys. Chem. Lett.* **2017**, *8*, 3133−3141.
(253) Pezzotti, S.; Galimberti, D. R.; Shen, Y. R.; Gaigeot, M. P. Structural Definition of the BIL and DL: A New Universal Methodology to Rationalize Non-Linear $\chi^{(2)}(\omega)$ SFG Signals at Charged Interfaces, Including $\chi^{(3)}(\omega)$ Contributions. *Phys. Chem. Chem. Phys.* **2018**, *20*, 5190−5199.
(254) Cyran, J. D.; Donovan, M. A.; Vollmer, D.; Brigiano, F. S.; Pezzotti, S.; Galimberti, D. R.; Gaigeot, M. P.; Bonn, M.; Backus, E. H. G. Molecular Hydrophobicity at a Macroscopically Hydrophilic Surface. *Proc. Natl. Acad. Sci. U. S. A.* **2019**, *116*, 1520−1525.
(255) Mahe, J. Ph.D. Dissertation, 2017.
(256) Van-Oanh, N. T.; Falvo, C.; Calvo, F.; Lauvergnat, D.; Basire, M.; Gaigeot, M. P.; Parneix, P. Improving Anharmonic Infrared Spectra using Semiclassically Prepared Molecular Dynamics Simulations. *Phys. Chem. Chem. Phys.* **2012**, *14*, 2381−2390.
(257) Hase, W. L., Ed. *Comparisons of Classical and Quantum Dynamics*; Jai Press: London, 1998.

https://dx.doi.org/10.1021/acs.chemrev.9b00547
Chem. Rev. 2020, 120, 3233−3260

(258) Pratihar, S.; Ma, X. Y.; Homayoon, Z.; Barnes, G. L.; Hase, W. L. Direct Chemical Dynamics Simulations. *J. Am. Chem. Soc.* **2017**, *139*, 3570−3590.
(259) Xie, Z.; Bowman, J. A. Zero-Point Energy Constraint in Quasi-Classical Trajectory Calculations. *J. Phys. Chem. A* **2006**, *110*, 5446−5449.
(260) Habershon, S.; Manolopoulos, D. E. Zero Point Energy Leakage in Condensed Phase Dynamics: An Assessment of Quantum Simulation Methods for Liquid Water. *J. Chem. Phys.* **2009**, *131*, 244518.
(261) Martinez, M.; Gaigeot, M. P.; Borgis, D.; Vuilleumier, R. Extracting Effective Normal Modes from Equilibrium Dynamics at Finite Temperature. *J. Chem. Phys.* **2006**, *125*, 144106−144106.
(262) Gaigeot, M.-P.; Martinez, M.; Vuilleumier, R. Infrared Spectroscopy in the Gas and Liquid Phase from First Principle Molecular Dynamics Simulations: Application to Small Peptides. *Mol. Phys.* **2007**, *105*, 2857−2878.
(263) Mathias, G.; Ivanov, S. D.; Witt, A.; Baer, M. D.; Marx, D. Infrared Spectroscopy of Fluxional Molecules from (ab Initio) Molecular Dynamics: Resolving Large-Amplitude Motion, Multiple Conformations, and Permutational Symmetries. *J. Chem. Theory Comput.* **2012**, *8*, 224−234.
(264) Schmitz, M.; Tavan, P. Vibrational Spectra from Atomic Fluctuations in Dynamics Simulations. I. Theory, Limitations, and a Sample Application. *J. Chem. Phys.* **2004**, *121*, 12233−12246.
(265) Schmitz, M.; Tavan, P. Vibrational Spectra from Atomic Fluctuations in Dynamics Simulations. II. Solvent-Induced Frequency Fluctuations at Femtosecond Time Resolution. *J. Chem. Phys.* **2004**, *121*, 12247−12258.
(266) Bowman, J. M.; Zhang, X. B.; Brown, A. Normal-mode analysis without the Hessian: A driven molecular-dynamics approach. *J. Chem. Phys.* **2003**, *119*, 646−650.
(267) Kaledin, M.; Brown, A.; Kaledin, A. L.; Bowman, J. M. Normal Mode Analysis using the Driven Molecular Dynamics Method. II. An Application to Biological Macromolecules. *J. Chem. Phys.* **2004**, *121*, 5646−5653.
(268) Galimberti, D. R.; Milani, A.; Tommasini, M.; Castiglioni, C.; Gaigeot, M.-P. Combining Static and Dynamical Approaches for Infrared Spectra Calculations of Gas Phase Molecules and Clusters. *J. Chem. Theory Comput.* **2017**, *13*, 3802−3813.
(269) Alauddin, M.; Biswal, H. S.; Gloaguen, E.; Mons, M. Intra-Residue Interactions in Proteins: Interplay between Serine or Cysteine Side Chains and Backbone Conformations, Revealed by Laser Spectroscopy of Isolated Model Peptides. *Phys. Chem. Chem. Phys.* **2015**, *17*, 2169−2178.
(270) Yan, B.; Jaeqx, S.; van der Zande, W. J.; Rijs, A. M. A Conformation-Selective IR-UV Study of the Dipeptides Ac-Phe-Ser-NH_2 and Ac-Phe-Cys-NH_2: Probing the SH—O and OH—O Hydrogen Bond Interactions. *Phys. Chem. Chem. Phys.* **2014**, *16*, 10770−10778.
(271) Cremades, N.; Dobson, C. M. The Contribution of Biophysical and Structural Studies of Protein Self-Assembly to the Design of Therapeutic Strategies for Amyloid Diseases. *Neurobiol. Dis.* **2018**, *109*, 178−190.
(272) te Brinke, E.; Groen, J.; Herrmann, A.; Heus, H. A.; Rivas, G.; Spruijt, E.; Huck, W. T. S. Dissipative Adaptation in Driven Self-Assembly Leading to Self-Dividing Fibrils. *Nat. Nanotechnol.* **2018**, *13*, 849−855.
(273) Okesola, B. O.; Mata, A. Multicomponent Self-Assembly as a Tool to Harness New Properties from Peptides and Proteins in Material Design. *Chem. Soc. Rev.* **2018**, *47*, 3721−3736.
(274) Tao, K.; Levin, A.; Adler-Abramovich, L.; Gazit, E. Fmoc-Modified Amino Acids and Short Peptides: Simple Bio-Inspired Building Blocks for the Fabrication of Functional Materials. *Chem. Soc. Rev.* **2016**, *45*, 3935−3953.
(275) Hartl, F. U. In *Annu. Rev. Biochem.*; Kornberg, R. D., Ed.; 2017; Vol. *86*, pp 21−26.
(276) Chiti, F.; Dobson, C. M. Protein Misfolding, Amyloid Formation, and Human Disease: A Summary of Progress Over the Last Decade. *Annu. Rev. Biochem.* **2017**, *86*, 27−68.
(277) Eisenberg, D. S.; Sawaya, M. R. Structural Studies of Amyloid Proteins at the Molecular Level. *Annu. Rev. Biochem.* **2017**, *86*, 69−95.
(278) Gerhards, M.; Unterberg, C.; Gerlach, A.; Jansen, A. β-Sheet Model Systems in the Gas Phase: Structures and Vibrations of Ac-Phe-NHMe and its Dimer $(Ac\text{-}Phe\text{-}NHMe)_2$. *Phys. Chem. Chem. Phys.* **2004**, *6*, 2682−2690.
(279) Vaden, T. D.; Gowers, S. A. N.; Snoek, L. C. Observation of β-Sheet Aggregation in a Gas-Phase Tau-Peptide Dimer. *J. Am. Chem. Soc.* **2009**, *131*, 2472−2474.
(280) Fricke, H.; Gerlach, A.; Gerhards, M. Structure of a β-sheet Model System in the Gas Phase: Analysis of the Fingerprint Region up to 10 μm. *Phys. Chem. Chem. Phys.* **2006**, *8*, 1660−1662.
(281) Gerhards, M.; Unterberg, C.; Gerlach, A. Structure of a β-Sheet Model System in the Gas Phase: Analysis of the C = O Stretching Vibrations. *Phys. Chem. Chem. Phys.* **2002**, *4*, 5563−5565.
(282) Jaeqx, S. Ph.D. Dissertation, Radboud University, 2014, https://repository.ubn.ru.nl/bitstream/handle/2066/130135/130135.pdf (accessed January 28, 2020).
(283) Abo-Riziq, A.; Crews, B. O.; Callahan, M. P.; Grace, L.; de Vries, M. S. Spectroscopy of Isolated Gramicidin Peptides. *Angew. Chem., Int. Ed.* **2006**, *45*, 5166−5169.
(284) Wallace, B. A. Gramicidin Channels and Pores. *Annu. Rev. Biophys. Biophys. Chem.* **1990**, *19*, 127−157.
(285) Allen, T. W.; Andersen, O. S.; Roux, B. Energetics of Ion Conduction Through the Gramicidin Channel. *Proc. Natl. Acad. Sci. U. S. A.* **2004**, *101*, 117−122.
(286) Ketchem, R. R.; Hu, W.; Cross, T. A. High-Resolution Conformation of Gramicidin-A in a Lipid Bilayer by Solid-State NMR. *Science* **1993**, *261*, 1457−1460.
(287) Kelkar, D. A.; Chattopadhyay, A. The Gramicidin Ion Channel: A Model Membrane Protein. *Biochim. Biophys. Acta, Biomembr.* **2007**, *1768*, 2011−2025.
(288) Veatch, W. R.; Fossel, E. T.; Blout, E. R. Conformation of Gramicidin-A. *Biochemistry* **1974**, *13*, 5249−5256.

https://dx.doi.org/10.1021/acs.chemrev.9b00547
Chem. Rev. 2020, 120, 3233−3260